A FAST, SCALABLE ACOUSTIC RESONATOR-BASED BIOSENSOR ARRAY SYSTEM FOR SIMULTANEOUS DETECTION OF MULTIPLE BIOMARKERS

A Thesis
Presented to
The Academic Faculty

by

Farasat Munir

In Partial Fulfillment
of the Requirements for the Degree
Doctor of Philosophy in the
School of Electrical and Computer Engineering

Georgia Institute of Technology
December 2012

A FAST, SCALABLE ACOUSTIC RESONATOR-BASED BIOSENSOR ARRAY SYSTEM FOR SIMULTANEOUS DETECTION OF MULTIPLE BIOMARKERS

Approved by:

Bruno Frazier, Committee Chair
School of Electrical and Computer Engineering
Georgia Institute of Technology

William D. Hunt, Advisor
School of Electrical and Computer Engineering
Georgia Institute of Technology

J. Stevenson Kenney
School of Electrical and Computer Engineering
Georgia Institute of Technology

Mary Ann Ingram
School of Electrical and Computer Engineering
Georgia Institute of Technology

Nael A McCarty
Department of Pediatrics
Emory University School of Medicine

Date Approved: 30th July 2012

To my Mother and Father.

ACKNOWLEDGEMENTS

I would first like to thank my advisor, Dr. William Hunt, for this thesis was not possible without his guidance, help, and constant encouragement. I am also thankful to my thesis committee members.

Special thanks goes to my parents, who tried very hard to instill in me the love of knowledge which ultimately put me in pursuit of PhD. I hope that with the completion of my PhD I can look honest when I say to them that they have been successful. I am also much thankful to my brothers Faisal Munir, and Moazzam Munir for they took care of my responsibilities so that I can come to study at Georgia Tech. Always assuring me of their support and urging me not to worry about back home.

After my parents and God the biggest thanks, however, go to my dearest friend Muhammad Omer, for his contributions to my life and my PhD are matched by none. Many a times he single-handedly kept me afloat, hopeful and on course. I can never fully thank him and can never really count in how many ways I benefit from him. I just hope that he continues to be so amazing for me and for my family.

Another big influence is my wife Sadia Nasir, who endured me through very difficult times and showed me a whole new perspective on life. I am indeed very thankful to her for continuously supporting me throughout my PhD, for making my shoulders light in so many ways, giving me the comfort of home. Without her i may have quit PhD due to the monstrous home sickness. The journey of PhD would have been very very boring without her presence. Another big big reason to thank my wife is our daughter Fatima Farasat, what a lovely thing she is, one look at her smiling face makes me forget all worries and gets me ready for work. Thanks to my wife, i get to see lots and lots of smiles on my daughter's face.

Another dear friend is Sir Qaiser Chaudry and his family with whom I began this journey of PhD together. He is not my superior in any formal sense but i dearly like to call him "Sir

Qaiser". He and his family supported me in numerous ways and made my stay at Georgia Tech very very pleasant, specially his wife who always made me feel like a younger brother and welcome at their home. Because of them my parents were less worried about me being in a foreign country. I am indeed very thankful to him and his family and look forward to a lifelong relationship with them.

I would also like to thank Dr. Murtaza Askari and Dr. Ali Hashmi and their family who facilitated me in settling down at Georgia Tech, supported me in a number of ways and always gave me very sound and encouraging advice.

I am deeply thankful to my friends and room mates, Mir Adeel Masood and Moazzam Ali Khan who supported me and helped me on numerous occasions during my stay at GaTech. I must also acknowledge, Muhammad Usman, Muhammad Salman Asif, Muhammad Bilal, Umer Tariq and other Pakistani friends here at GaTech, who contributed towards my success in one way or the other.

Among the Lab members at "Microelectronic Acoustic Group" I am particularly indebted to Adam Wathen and Ryan Westafer for their support, encouragement and insightful discussions always helping me along on the way towards my PhD. Special thanks for Dr. Anthony Dickherber, Dr. Chris Corso who were my mentors in the MAG Lab, they supported me in the beginning of my research and set very good examples for me to follow. My research work takes a number of cues from their research work. I would also like to acknowledge the rest of MAG group members Stephen Mobley, Stephen Mihalko, Sean McGee, Warsame Heban, Stephen Welch, Steve Ruff, and Alice Wang.

Finally, I would like to thank my professors from my alma matter in Pakistan i.e "University of Engineering and Technology Lahore" for putting me on the right path. Specially I am highly highly thankful to Dr. Noor M. Sheikh, Dr. Amjad Luna and Dr. Aun Abbas for their kind advice and enabling my success.

TABLE OF CONTENTS

LIST OF TABLES

LIST OF FIGURES

SUMMARY

This thesis is about the design of a biosensor system for detection of multiple cancer biomarkers. Accurate diagnosis and prognosis of cancer requires early detection. Equally important, though, is the measurement of biomarker-velocity and detection of multiple biomarkers. Early detection requires highly sensitive biosensors capable of detection at very low concentrations of target molecules. Biomarker-velocity can be measured by monitoring concentration of target molecule over a period of time. This requires a system which is very easy to use, fast, flexible, inexpensive and portable, thus enabling its ubiquitous presence at the point of care. For detection of multiplexed biomarkers, biosensors which easily lend to array configuration are required. Conventional techniques do not fulfill either all or some aspects of the requirements listed above.

In this work, we present the design of a biosensor system, keeping in view the desired features described above, to achieve the ultimate goal of enabling ubiquitous presence of biosensor at the point of care. We focus on acoustic transducer based biosensors. The two fundamental components of design in an acoustic biosensor are the design of an acoustic transducer and the design of a novel electrical interface for the transducer. For transducer design, we introduce and present the design of a single structure, GHz range, multi-mode acoustic resonator. We present this as a suitable transducer for liquid phase biosensors, which is the preferred medium for sensing of cancer biomarkers. We explore the underlying physics and do experimental and theoretical characterization of this device. The transducer needs to be functionalized with a chemically sensitive layer which performs the molecular recognition of cancer biomarkers. We present the experimental exploration of a reversible and oriented immobilization based Histidine-Ni(2+) interaction which used NTA as the chelator for anchoring onto the device. Then we discuss the microfluidic design to enable liquid phase operation. We used SU-8 polymer barriers for liquid containment and addressed the challenges of making it compatible with ZnO based devices.

An electrical interface is needed to excite and extract the sensor response. We have presented here a novel method to measure and track a resonator's response and extract its characteristic parameters. This method measures the wideband frequency response of the resonator with a much simpler setup as compared to conventional methods. We have proposed and demonstrated the use of a white noise signal as a viable signal for broadband excitation of resonator-based sensing platforms. We have also established, shown through simulation and prototype measurements, the feasibility of the proposed method. The accuracy and speed of the system can be further greatly improved by FFT-based digital implementation of the spectral analysis system. We have presented an example hardware implementation of FFT-based signal analyzer, and have discussed the hardware resources required for actual implementation in a chip form. Lastly we discuss the measurement protocol and sensor results for head and neck cancer and prostate cancer biomarkers. These results demonstrate the usability of the proposed sensor system for detection of cancer biomarkers.

Given the current biosensors landscape, the work in this thesis enables the evolution of biosensors in several important directions. By introducing novel characterization methods, highly sensitive, cost effective, and CMOS-integrate able, sensor design, this thesis paves way for future developments that can realize the goal of ubiquitous presence of biosensor at the point of care.

CHAPTER I

INTRODUCTION

1.1 Biosensors: Cancer Diagnostics at the point of care

In 2012, over 570,000 Americans are expected to die of cancer, more than 1,500 people per day [4]. Cancer is the second most common cause of death in the US, exceeded only by heart disease, accounting for nearly 1 of every 4 deaths. Cancer is also one of the most expensive diseases. The National Institutes of Health (NIH) estimates that the overall costs of cancer in 2007 were $226.8 billion [4].

The early diagnosis of cancer is crucial for patient survival and successful prognosis of the disease. Existing methods of cancer screening rely heavily on invasive techniques such as performing a biopsy and examining the tissue to detect cancer cells. Relatively recent methods employ the analysis of tumor associated antigens as biomarkers. These biomarkers are molecules that can be found in human fluids such as urine,blood, serum, or spinal fluids as well as inside or on the tumor cells [5]. There are a range of biomarkers that are associated with different types of cancers. Many markers are still being evaluated to establish their detection capability.

One of the most widely used methods to detect cancer biomarkers is ELISA (Enzyme Linked Immunosorbant Assay). ELISA, though is time consuming, expensive, and requires high level of expertise. Moreover, ELISA is not sensitive enough to detect very low concentration of biomarkers, which is key for early detection [5]. Very sensitive and specific methods are required for early detection. Information about the stage, progression, regression and probability of recurrence of a disease, if available, can have a significant impact on both the survivability and treatment options. There is thus a need for a biosensor technology that provides all this information at the point of care, and with minimum time.

Cancer cells disrupt the normal cellular behavior and cause a range of changes in the

human body such as inactivation of tumor suppressor genes, activation of oncogenes, over-expression of certain proteins [5]. The rate of disruption also varies with the stage of cancer and its location. Modern molecular methods are being used to derive biomarkers corresponding to all these changes. Therefore the analysis of a range of biomarkers corresponding to these changes and a continuous monitoring of the biomarker level will be potentially more useful compared to a single biomarker. We will now look at a few examples that use biomarkers for cancer detection.

Prostate cancer is the most common type of cancer in men with an estimated 240,000 new cases in 2012 [4]. The level of Prostate Specific Antigen (PSA) in blood serum is commonly used to screen for prostate cancer. The threshold level of PSA is considered to be $4.0ngl^{-1}$. PSA levels above this threshold level are strongly correlated with prostate cancer. In addition to prostate cancer, elevated PSA levels may also indicate benign prostatic hyperplasia, prostatitis (inflammation of the prostate), or smaller tumors that do not prove to be fatal [6]. Thus, elevated PSA levels alone are not always indicative of prostate cancer. Treatment options for prostate cancer are invasive, life changing, and costly. Therefore the value of PSA as a screening test for prostate cancer has become controversial. Additional information is required in order to detect the presence of life-threatening prostate cancer. In a study [7] published in the Journal of the National Cancer Institute it was shown that rate of change of the PSA level i.e. 'PSA' velocity may help identify men with life-threatening prostate cancer during a period when their PSA levels are associated with the curable stage of the disease. Figure 1.1 (reproduced from [7]) shows a plot of distributions of PSA levels and PSA velocity as a function of years before diagnosis. PSA velocity, measured 10 - 15 years before diagnosis (when most men had PSA levels below 4.0 ng/mL) was associated with cancer-specific survival 25 years later; survival was 92% among men with PSA velocity of 0.35 ng/mL per year or less and 54% among men with PSA velocity above 0.35 ng/mL per year. Furthermore, men with PSA velocity above 0.35 ng/mL per year had a higher relative risk of prostate cancer death than men with PSA velocity of 0.35 ng/mL per year or less.

For many types of cancer there does not exist a single ideal biomarker. A group of

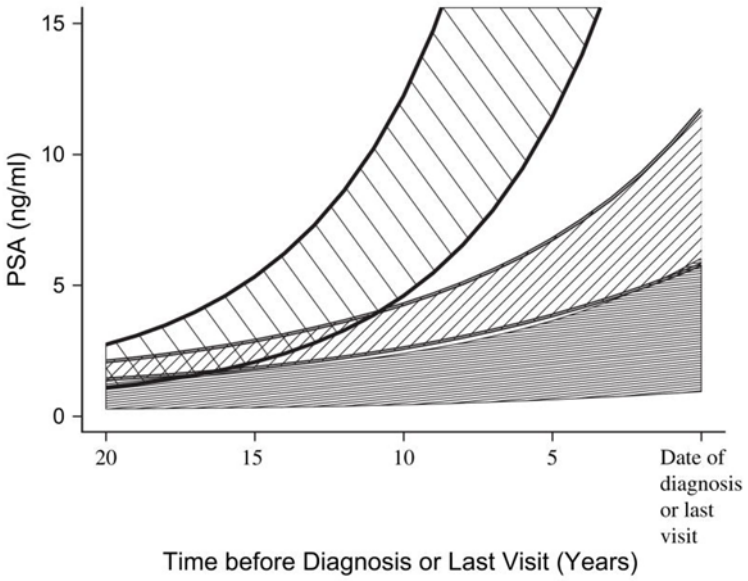

Figure 1.1: Average Prostate Specific Antigen (PSA) levels in ng/mL as a function of years before diagnosis (prostate cancer) or last visit (no prostate cancer). Subjects who died of prostate cancer (top cross-hatched area); subjects with prostate cancer who where alive or died of another cause (middle cross-hatched area); and subjects without prostate cancer (bottom solid area).(after [7])

biomarkers can provide more reliable and relevant information than a single biomarker. For prostate cancer, PSA is not the only relevant biomarker. [8] and [9] have shown that a panel of markers including PSA, free PSA (fPSA), human kellekrin 2 (hK2) and total PSA is more effective in detecting prostate cancer. For head and neck cancer a combination of TGF-α and EGFR protein are useful in distinguishing patients at high risk of tumor recurrence and in guiding therapy [10].

Kozak et al. [1] showed that the use of a group of biomarkers improves detection of early stage ovarian cancer compared to a single biomarker. They performed multivariate analysis on 5 biomarkers, namely transthyretin (TTR), beta-Hemoglobin (HB), apolipoprotein AI (APOAI), transferrin (TF), and Cancer Antigen CA125. The results based on their data are graphically displayed in Figure 1.2. It can be seen that for each stage, the Receiver Operating Characteristic (ROC) area is greater with multiple biomarkers compared to the commonly used single biomarker CA125. The ROC area for a particular test represents the accuracy of a test, and as the ROC area tends to one, the test becomes more and more

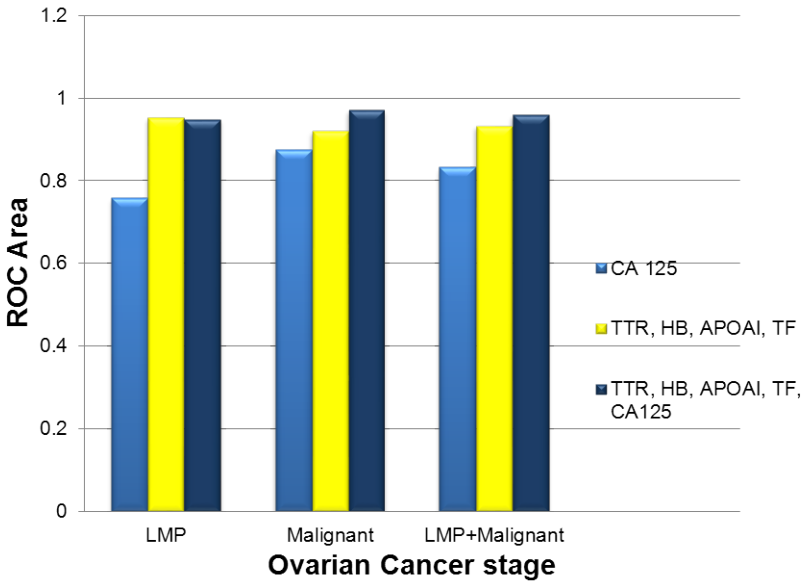

Figure 1.2: ROC area of a diagnostic test using single biomarker compared to multiple biomarkers for different stages of Ovarian Cancer(The accuracy of a test is greater if its ROC area is closer to 1). (based on the data in [1])

accurate.

There is therefore a need for a biosensor technology that is simple, detects multiple cancer biomarkers and is highly sensitive. Modern biosensors must also be present at the point of care to provide rapid and repeated measurement of biomarkers. Repeated measurements will allow time dependent measurements such as biomarker velocity as well as more accurate information about disease progress. The success and applicability of biosensors as point-of-care tools is based on five requirements. They need to be sensitive, specific, fast, cheap, and portable. Availability at the point of care demands that the biosensor system be inexpensive and portable. It should also be fast and require only minimal training or expertise. Current biosensors are primarily designed for measuring the level of a single biomarker. They are expensive, consist of bulky equipment, require high level of expertise to operate and provide results after a significant delay.

We can summarize the desired features or feature goals for a biosensor system for effective cancer diagnosis and prognosis as follows:

1.1.1 Feature Goals for Biosensors at POC

- Highly sensitive and specific to target biomarker to enable early detection
- Fast, flexible and inexpensive
- Capable of simultaneous multiple biomarkers detection
- Requires minimal training or expertise
- Able to process a large number of samples rapidly.

1.2 Biosensor System

The purpose of the biosensor system is to determine the presence, absence or concentration of specific target molecules (biomarkers) in an environment. The biosensor system relies on the detection of a molecular recognition event e.g. an antigen binding to an antibody. A chemically sensitive layer (from here on referred to as bio-recognition layer) performs the molecular recognition. The layer itself is functionalized onto a transducer. These molecular recognition events may alter one or more properties of the transducer. Corresponding to these changes the transducer generates an electrical signal which can be measured, displayed, and analyzed. Therefore bio-recognition layer and the transducer are the two main components of a biosensor. A good transducer design and a functionalization layer design are fundamental requirements for a working biosensor. Additionally, for these two components to make a useable biosensor, the complete biosensor system should provide the following functionalities:

a) An effective electrical interface circuit to excite and read out the transducer response.

b) The capability to analyze the sensor response in equivalent parameters of an electrical model of sensor

c) Translation of the sensor data from electrical parameters to physical properties of the surface perturbation layer

d) Relate the physical terms to a chemical, biological or physical phenomenon.

e) Microfluidic design compatible with the transducer to enable the functioning of the sensor in liquid phase (required for most bio sensing needs).

The research work required to enable all the above functionalities in a biosensor system spans several different areas of expertise and is carried out in many different academic specialties. Below we show a block diagram (Figure 1.3) which divides the research work into individual concentration areas. Each of the comprising blocks is a separate research field in its own right. However, in this thesis we are presenting a holistic effort towards a biosensor system. We believe that a holistic effort will allow for easier,more efficient, and optimized integration of these components, and will result in a better biosensor system. The system components will be designed keeping in view the feature goals of a biosensor, described in Section 1.1, with the overarching objective of enabling a viable presence of the biosensor system at the point of care. For this purpose, the work in this thesis spans nearly all of these blocks. The major contributions however are in the blocks of transducer design, and electrical interface design.

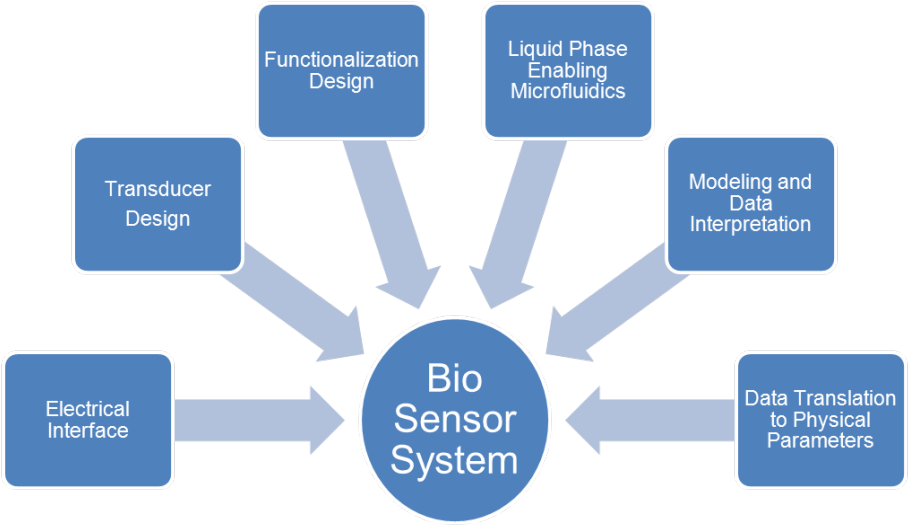

Figure 1.3: The complete biosensor system

We now give a brief background about existing realizations of biosensing methods and lead towards the particular methods that are the focus of this work.

Conventional methods for biosensing are time consuming, prone to contamination, and often require a labeling technique (fluorescent, radio, or colorimetric) to identify the target molecule. Techniques based on the immunoassay principle such as ELISA are relatively rapid, but they suffer from lack of sensitivity, require a high level of expertise, and are unsuited to process a large number of samples in a short time.

A number of biosensor modalities (grouped as label-free biosensors) do not require use of detection labels. Such techniques have been widely adopted in research laboratories. Label-based techniques only give information about the presence of a target molecule, whereas label-free techniques can provide insight into real time molecular interaction.

Among the label-free techniques the most notable is the Surface Plasmon Resonance (SPR) Technique. This technique measures the change in refractive index or dielectric constant of a solution in the vicinity of the sensor surface. Though, SPR can be extremely sensitive under controlled conditions; it requires bulky and expensive equipment. Another important thing to note is that SPR only provides information about the optical properties of the material. However for complete characterization, mechanical and viscoelastic properties of the target material and sample are important. Piezoelectric acoustic sensors offer the potential to measure mechanical (e.g. mass density, stiffness), viscoelastic (e.g. viscosity, shear moduli) and electrical properties (e.g. permittivity) and are thus able to provide a better insight into molecular interactions. Thus they are the focus of this work.

1.3 Organization of The Thesis

We begin with the discussion of the transducer design. We present the case for acoustic resonators as a suitable transducer to fulfill the feature goals listed in section 1.1. Chapter 2 describes in detail the design of the transducer, covering the theoretical aspects, the practical fabrication challenges, and some measured results. Two principal types of acoustic modes of propagation are the Thickness Shear Mode and the Thickness Extensional Mode. We describe a novel design of a single structure device that is simultaneously resonant in both modes. Such a device can have potentially useful applications for sensing purposes. In addition, in the measured results, we highlight the observation of a hybrid mode. The

multi-mode acoustic devices described in Chapter 2 must be characterized for their acoustic, electric, and sensing behavior before being used as a bio-sensor. In Chapter 3, we present the investigation of various aspects of each of the resonant modes of the multi-mode device. Both experimental and simulation tools are used for this characterization. A key aspect is the thickness variation of the piezoelectric layer and the corresponding change in the resonance frequency of each mode. To establish their sensing properties, these devices are characterized against various known stimuli of different electrical and viscoelastic properties. Experimental results are given followed by discussion. Lastly we describe the implementation of these devices in array format suitable for liquid phase biosensing applications.

Secondly in Chapter 4, we discuss the microfluidics required for liquid phase operation. After the device functionalization, the amount and location of the liquid sample over the devices must be controlled for successful liquid phase measurement. In addition the probing pads of the device must be isolated from the active area of the device exposed to the sample to ensure an accurate measurement. For this purpose we investigated the use of SU-8 polymer barriers for liquid containment. The design of microfluidics mask, the recipe of SU-8 fabrication process, and the challenge of making it compatible with ZnO-based devices are discussed in this chapter.

In Chapter 5 we focussed on the aspects of biosensor design which impart the sensing functionality to our acoustic transducer i.e the functionalization of the transducer by immobilizing a chemically sensitive layer on our acoustic transducer. We highlighted the importance of oriented immobilization and reversible scheme for preserving the activity of immobilized proteins and to allow for regeneration of the device surface. We presented Histidine-Ni interaction based surface chemistry as a suitable technique for oriented and reversible immobilization. We showed our efforts at using this functionalization approach on our ZnO based devices with Ni-NTA terminated alkane-thiol SAM and Ni-NTA terminated organosilane SAM. We also suggested the use of a thin layer of Silicon Oxide on top of ZnO as a protective layer to prevent the etching of ZnO during the immobilization procedure.

We also presented a preliminary investigation of using our ZnO based BAW resonator devices as a biosensor for detection of Head and Neck Cancer biomarkers. The results of these experiments demonstrated that our device are capable of detection of biomarkers in complex medium such as cell lysate and that they exhibit very high sensitivity and selectivity compared to ELISA based detection of the same biomarkers.

Chapter 6 focuses on describing a new method for extracting data from resonator based sensing devices, which leads toward an easy electronic interface for sensor systems. The electrical interface to the transducer/resonator plays a very important role in achieving the goals underlined for our biosensor system in Section 1.1.1. This interface allows for accessibility of the transducer response, determines its usability, manufacturability (to some extent), and its cost. Thus a low cost, easy to use interface to the transducer can enable the ubiquitous presence of the biosensor. In this chapter, simulation results are first presented for verification of the proposed system, followed by measurement results with a prototype implementation. The accuracy and speed of the system can be further improved by FFT-based digital implementation of the spectral analysis system. This will allow for a low-cost and compact stand-alone implementation. We discuss the system architecture for this stand-alone implementation in chapter 7. The system architecture consist of two major parts i.e. the analog signal conditioning chain and the FFT based digital spectrum analyzer. The design of this system is presented according to the specifications followed by measurements and a discussion on results. Chapter 7 is the culmination of the research efforts, where we present the sensor tests for head and neck cancer and prostate cancer biomarkers. In the last chapter 8 we draw conclusions from the research effort described in this thesis and point to possible directions for future work.

CHAPTER II

TRANSDUCER DESIGN

2.1 Introduction

The transducer is the central component around which all other components are designed to make a complete biosensor system. As discussed in Section 1.2 the piezoelectric acoustic resonators offer many advantages over other types of transducers. Therefore, the transducer design presented here is focussed on piezoelectric acoustic resonators.

There are different types of acoustic sensors based on the type of acoustic wave being set up in them. The goal is to design a transducer suitable for liquid phase biosensing operation. The device design presented here, is the Bulk acoustic wave (BAW) resonator using ZnO piezoelectric film in Solidly mounted resonator (SMR) configuration. In this chapter, we cover the necessary theoretical background, which is followed by fabrication and measurements of the device.

First, we give a review of different types of acoustic wave devices used for sensing purposes and discuss that for highly sensitive sensor devices BAW devices are the best choice. Furthermore, for liquid phase operation Thickness shear mode (TSM) based BAW devices are best suited. Then we present theoretical discussion of BAW devices to develop an understanding of basics of BAW resonator design. This is followed by a discussion of conditions necessary for setting up TSM in ZnO. Then the advantages of solidly mounted resonator configuration are described since the device developed employs this configuration.

Lastly, leveraging the the theoretical foundations laid in this chapter, we describe the design of a functional BAW resonator. This is a novel multi-mode device design, which is a single structure resonant in multiple bulk acoustic wave modes in the GHz range. This device could be potentially more useful than a single mode device.

2.2 Piezoelectric Acoustic Sensors

Piezoelectric acoustic sensors are a type of biosensors that fall under the broad category of mass-sensitive biosensors (also called gravimetric sensors). The sensing functionality is based on the property of acoustic devices that they are sensitive to surface boundary conditions such as mass change, viscosity, and to some extent permittivity of the sample at the device surface. There are different types of acoustic sensors based on the type of acoustic wave being set up in them. Broadly, they can be classified as surface acoustic wave (SAW) sensors, bulk acoustic wave sensors (BAW) and flexural plate mode sensors. The simplest and most widely used acoustic wave biosensor is quartz crystal microbalance (QCM). It consists of a piezoelectric quartz crystal that is resonant in thickness shear mode (TSM) bulk acoustic waves. In 1959, Sauerbrey first demonstrated that mass addition to QCM sensor surface results in a decrease in the resonance frequency [11]. He identified a relationship between the adsorbed mass (Δm), and change in frequency (Δf), as

$$\Delta f = \frac{-2f_0^2 \Delta m}{A\sqrt{\rho_q \mu_q}} \tag{2.1}$$

where f_0 is the resonant frequency of the unperturbed resonator, A is the area under the electrodes of the resonator, ρ_q is the crystal mass density, and μ_q is the shear modulus of the crystal. This relationship gives the sensing principle for all acoustic wave devices, though it is only valid for rigid and homogenous mass films. The sensitivity of 5MHz crystal based on this relation is 17.7 $ngHz^{-1}cm^{-2}$. This sensitivity in the nanogram range led to the use of QCM as a tool for measuring thin-film deposition thickness [12], and for studying adsorption phenomena at the solid-gas and solid-liquid interface. Thus very sensitive QCM based mass measuring devices have been reported in the literature both in gas phase [13] and in liquid media [14].

A typical quartz crystal resonator layout is shown in Figure 2.1. The electrodes are used to excite the wave in the quartz crystal plate as well as sense the resulting resonance characteristics. The resonance frequency is inversely proportional to the thickness of the quartz plate. This is clear from the following relation, which is true for all BAW devices operating in pure thickness mode:

$$f_r = \frac{v_a \cdot N}{2d},\ N = 1, 3, 5, \ldots \tag{2.2}$$

where d is the thickness of the quartz crystal plate, n is the odd harmonic mode number, and v_a is the acoustic wave velocity in the quartz plate.

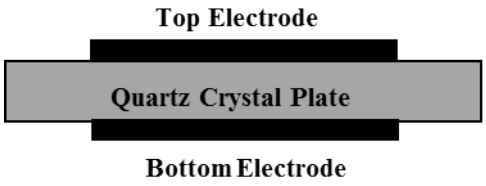

Figure 2.1: Quartz Crystal resonator

According to Equation 2.1, the mass sensitivity varies as the square of frequency, and Equation 2.2 tells us that for higher frequency devices we need thinner plates. Thus, thinner devices are required for higher mass sensitivity. But thinning down beyond a certain point makes the device difficult to fabricate and handle, and results in fragile devices. Therefore, Surface acoustic wave (SAW) devices were investigated for higher mass sensitivity. SAW devices typically operate in the range of 100 MHz to 800 MHz. In SAW devices the acoustic wave travels along the surface of the device and has a very small depth, a few wavelengths, into the substrate. Thus, they are highly sensitive to an added layer on the surface, which has different properties than the substrate. SAW devices have been described in detail in [15]. Further increase in sensitivity requires gigahertz range sensors. SAW devices are limited by a number of obstacles when designing for gigahertz range. Including the limitation and difficulty of lithography technology, increased resistivity of the interdigitated electrode patterns and propagation losses. Both QCM and SAW devices have large area, and a major shortcoming is that they are difficult to integrate with CMOS technology. Moreover, sensor arrays require a complex electronic interface. Hence, the integration ability with CMOS fabrication is a prerequisite for small footprint and low cost sensor systems. Advances in piezoelectric thin film deposition technology have led to the development of a new type of BAW devices that circumvent the above mentioned problems in QCM and SAW devices. Piezoelectric thin films of zinc oxide (ZnO) and aluminum nitride (AlN)

have been used to make film BAW resonators called FBAR [16, 17]. Thin-film deposition techniques such as RF-magnetron sputtering are compatible with CMOS techniques; they enable uniform sub-micrometer range thin films. Thus, the gigahertz range frequency of resonance has become possible. Moreover, the lateral size can be made much smaller (a few hundred micrometers) as compared to QCM (5mm). Recently, FBARs have been reported as sensitive biosensors both in gas and liquid phase [18, 19]. They have other useful applications such as RF filters in communications [20]. Thus the current body of research has established the suitability of the acoustic resonators as useful biosensors. Compared to other biosensing modalities they offer significant advantages. Therefore bulk acoustic wave acoustic resonators are our choice of transducer for the Biosensor design. In the following section we therefore discuss the theoretical background of the BAW resonator to lay the foundations of our Resonator Design.

2.3 BAW Resonator Theoretical Background

2.3.1 Principles of Acoustic Resonator

The fundamental principal of an acoustic resonator is the confinement of a traveling acoustic wave by a structure. This confinement results in a standing wave within the structure. The frequency of the standing wave is determined by the velocity of the wave and the dimensions of the confinement structure. For Bulk acoustic waves the traveling waves are generated in the bulk of a substrate and are confined by the dimensions of the substrate. Propagation of an acoustic wave in a solid can take several forms, or modes. In general, these waves can be either longitudinal (particle displacement in parallel with the propagation direction), shear (particle displacement perpendicular to the wave propagation direction) or a combination of the two. The longitudinal wave is characterized by particle displacement in the same direction as the propagating wave. In a thin-film resonator, the wave propagates through the thickness of the thin film and the particle displacement is similarly normal to the surface. The propagation of a sound wave in air is an example of a longitudinal wave.

For all practical applications of acoustic waves, piezoelectric substrates are used, because they provide an effective means of electrically generating and detecting acoustic vibrations.

Quartz crystal microbalance mentioned earlier is a BAW resonator using the piezoelectric quartz crystal. Piezoelectric materials exhibit the lack of Centro-symmetry in their crystal structure. When piezoelectric crystals are strained by an applied force, the lattice symmetry is disturbed causing charge asymmetry and as a result the material becomes electrically polarized. This is called direct piezoelectric effect. This is always accompanied by the converse piezoelectric effect, whereby the crystal becomes strained under the influence of an applied electric field. The strain thus produced reverses sign with the reversal of the applied electric field. Thus by applying oscillatory electric field to the piezoelectric crystal a mechanical acoustic wave can be launched and supported in it. The fundamental constitutive relations of the piezoelectric materials which relate the mechanical forces and electrical field are governed by Equations 2.3 and 2.4.

$$\mathbf{T} = \mathbf{c}^E : \mathbf{S} - \bar{\epsilon}^S \cdot \mathbf{E} \tag{2.3}$$

Where $\mathbf{T}$ is the stress, $\mathbf{S}$ is the strain, $\mathbf{c}^E$ is the 4th order three dimensional stiffness tensor at a constant electric field , $\bar{\epsilon}$ is the permittivity tensor at a constant strain, and $\mathbf{E}$ is the electric filed. The first term in this equation is the hooke's law in three dimensions and accounts for stress due to applied strain $\mathbf{S}$. The second term accounts for stress due to the applied electric filed in a piezoelectric material characterized by $\bar{\epsilon}$. The second equation of the constitutive relation is

$$\mathbf{D} = \bar{\epsilon}^S \cdot \mathbf{E} - \bar{\mathbf{e}} : \mathbf{S}, \tag{2.4}$$

where $\mathbf{D}$ is the Electric displacement. $\bar{\epsilon}$ is the permittivity tensor of the material. The first part on the right hand side is the basic Maxwell's definition of displacement due to electric field. The second part accounts for the electric displacement due to strain $\mathbf{S}$ in the piezoelectric material.

Within the piezoelectric material the acoustic and electric fields are described by the following equations.

$$\nabla \cdot \mathbf{T} = \rho \frac{\partial^2 \mathbf{u}}{\partial t^2} \tag{2.5}$$

$$\mathbf{S} = \nabla_s \mathbf{u} \tag{2.6}$$

$$\mathbf{E} = -\nabla \phi \tag{2.7}$$

Where ρ is the mass density of the piezoelectric substrate is the particle displacement, is the gradient matrix operator and ϕ is the scalar potential. First equation is the Newton's law and the second equation is the definition of three dimensional strain $\mathbf{S}$ in matrix form. The last equation defines electric field as the derivative of scalar potential ϕ, since we assume quasi static approximation. We manipulate these equations using the constitutive relations (detailed derivation in [21]) to arrive at the three dimensional wave equation in piezoelectric media.

$$\nabla \cdot \mathbf{c}^E : \nabla_s \mathbf{u} + \nabla . e : \nabla \phi = \rho \frac{\partial^2 \mathbf{u}}{\partial t^2} \tag{2.8}$$

This equation contains a term involving the electric potential ϕ . The term may be considered a source term responsible for the generation of an acoustic wave by a time- varying electrical potential.

The wave equation shown above is not so useful for analytical calculations. We need to transform it into a useful form. This is done by taking into account the direction of propagation of wave, solving for a plane wave through the bulk of a piezoelectric crystal and using matrix operations, we arrive at Equation 2.9. The details of derivation are given in [22]

$$\kappa^2 \Gamma_{ij} \nu_j = \rho \omega^2 \nu_i \tag{2.9}$$

This is the Christoffel equation where κ is the wave number defined as ω / va (frequency/acoustic velocity), is the density of the material, ν_i and ν_j are the particle polarization direction vectors, and Γ_{ij} is the piezoelectrically stiffened Christoffel matrix. Γ_{ij} is defined as

$$\Gamma_{ij} = l_{iK}\left(\mathbf{c}^{E}_{KL} + \frac{(e_{Kj}E_j)(E_i e_{iL})}{E_i \varepsilon^{S}_{ij} E_j}\right) l_{Ij}, \tag{2.10}$$

where e is the piezoelectric coupling tensor, ϵ^S is the 3x3 permittivity tensor at constant strain, E is the vector corresponding to external electric excitation field. The elements of the Christoffel matrix are functions of the plane wave propagation direction, the stiffness, permittivity, and coupling constants of the crystal, as well as the external electric field. The Christoffel equation gives a matrix equation form to wave equation. Thus the problem reduces to finding the eigen values of the Christoffel matrix. The Christoffel matrix is a 3x3 matrix;the eigen values are three real positive numbers that are the phase velocities of three possible propagating bulk modes(one longitudinal and two shear waves). The eigen vectors corresponding to the eigenvalues give the particle velocity direction for each of the three modes.Thses particle velocity directions are orthogonal to each other and are pure shear or pure longitudinal only for certain propagation directions.

2.4 Liquid Phase Operation and Acoustic Modes

Now we know that there are always three propagation mode solutions for any given direction l. A resonator can be designed using any of the three modes or a combination of these . As described in chapter 1 our goal is to design a transducer which is suitable for liquid phase operation. Any resonator designed must be suitable for liquid phase operation. The use of an acoustic resonator as a liquid phase sensor presents unique challenges. A liquid layer at the device surface is not rigid; it has some viscosity, and density associated with it. Hence the Sauerbrey relation (Equation 2.1) does not hold. Kanazawa and Gordon derived a relation to describe change in resonance frequency under liquid loading condition.

$$\Delta f = -f_0^{3/2}\sqrt{\frac{\eta_l \rho_l}{\pi \mu_q \rho_q}}, \tag{2.11}$$

Where f_o is the resonance frequency, ρ_l is the density of the liquid ,η_l is the viscosity of the liquid, ρ_q is the density of quartz, and μ_q is the shear modulus of the quartz crystal. Since the product $\rho * \eta$ is about two orders of magnitude higher for liquids than for gases, the crystal is heavily loaded in the liquid phase.

Hunt [23] has also given governing relations derived from the surface reciprocity relation using time-dependent perturbation theory,

$$t\frac{\partial \Delta\omega}{\partial t} + \Delta\omega = \frac{\omega_u h_f}{\pi\sqrt{\rho_q \mu_q}} \left\{ -\omega_u \left[\Delta\rho_f - \frac{\Delta\mu_f}{V_s^2} \right] + i \left[\frac{\partial \rho_f}{\partial t} - \frac{1}{V_s^2}\frac{\partial \Delta\mu_f}{\partial t} \right] \right\} \tag{2.12}$$

where the subscript "u" denotes the unperturbed field condition, "f" denotes the immobilized chemi-specific film, ω is the radian frequency, V_s is the velocity of the shear acoustic wave, and h_f is the height of the immobilized surface. Assuming that $\Delta\rho$, $\Delta\mu$, and $\Delta\omega$ do not change with time, the Hunt equation reduces to

$$\Delta f = -\frac{2f_u^2 h_f}{\sqrt{\rho_q \mu_q}} \left[\Delta\rho_f - \frac{\Delta\mu_f}{V_s^2} \right] \tag{2.13}$$

which is analogous to Sauerbrey's equation with the addition of a surface film stiffness dependency. These relations establish the detection capability of the acoustic resonators in liquid phase sensing.

The liquids can sustain acoustic longitudinal waves. Therefore, bulk acoustic resonators vibrating in the longitudinal mode dissipate energy into the liquid resulting in severe dampening of the resonator response. On the contrary, the propagation of acoustic shear waves is barely supported in liquids. Therefore, Thickness shear mode (TSM) devices are considered a better option for liquid phase sensing. Thickness shear mode is the mode in which the acoustic wave travels in the thickness direction of the substrate and the particle velocities are orthogonal to the propagation direction. TSM is the principal mode of operation in AT-cut quartz crystals (QCM), but for higher sensitivities FBARs operating in TSM at gigahertz have also been reported [21]. Thus we focus our attention on FBARs as they are the transducer of choice for liquid phase biosensors.

2.5 TSM Resonator using Thin Films

In FBAR instead of a crystal plate a piezoelectric thin film (a few hundred nanometers to a few micrometers) is used. Since Hunt lab has the facilities to fabricate high quality ZnO thin films. The piezoelectric material of interest for this research is zinc oxide (ZnO), which is a hexagonal 6mm class crystal. ZnO piezoelectric films have been used for resonator design for high frequency filter design application in Telecommunications industry. Typically these

devices operate in the longitudinal mode. TSM excitation requires the coupling to the lateral components of the piezoelectric coefficient matrix to excite particle motion parallel to the wave propagation direction. To achieve this coupling, the important things are the crystalline orientation of the ZnO thin film and the electrode configuration. For ZnO, the orientation is usually defined with respect to c-axis of the ZnO crystal. In longitudinal mode resonators the common method is to use c-axis oriented (c-axis parallel to the substrate normal) ZnO films sandwiched between two electrodes (Figure 2.2 (a)). In this configuration the electric field is parallel to the c-axis and can not excite the lateral particle displacement. For TSM, the common method to achieve lateral coupling is the use of ZnO thin films with c-axis inclined to the normal [24, 25] and the electrodes in the thickness excitation configuration. Recently, non inclined ZnO thin films (i.e c-axis oriented ZnO) have also been studied [21] for resonator design. With c-axis oriented ZnO films ,lateral field excitation (LFE) configuration shown in Figure 2.2 (b) is used. LFE involves co-planar electrodes generating an electric field parallel, or lateral, to the film surface. Since the growth of ZnO with inclined c-axis is more complex, we opt for the use of LFE with c-axis oriented ZnO films for generating TSM. In the following paragraphs we analyze theoretically the lateral field excitation and c-axis oriented ZnO thin films.

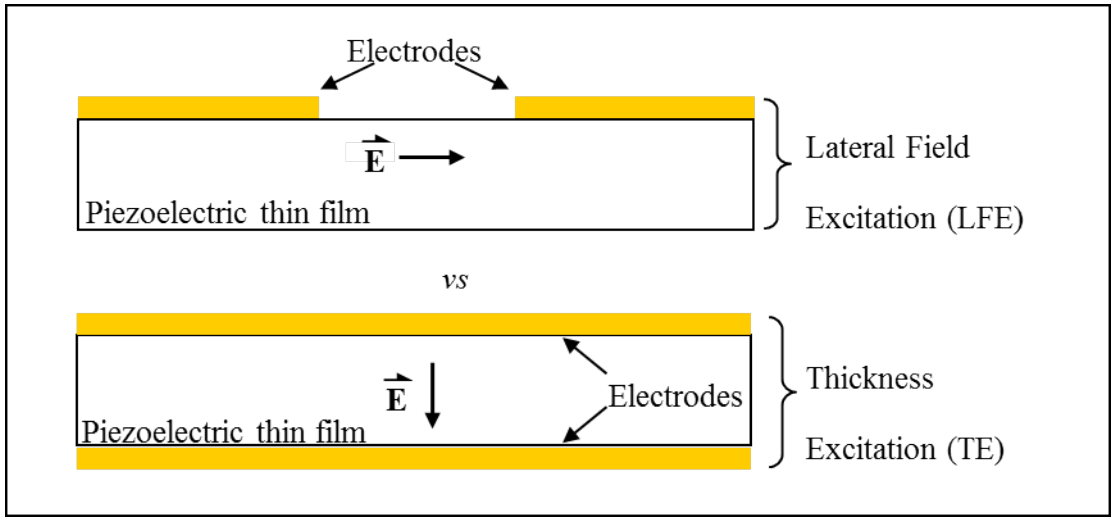

Figure 2.2: Lateral Field Excitation vs Thickness Excitation

Now we will use the Christoffel equation described earlier to theoretically analyze the

TSM in ZnO. We assume c-axis of ZnO is parallel to the z-axis in the xyz frame of our problem. The wave propagation is also in the z-direction. Since we are solving for the lateral field we set the z- component of the electric field vector as zero. The resulting field vector Ex is given as

$$\mathbf{E} = \begin{pmatrix} E_x \\ E_y \\ 0 \end{pmatrix} = E_i^T \tag{2.14}$$

For hexagonal crystals, like ZnO, the material tensors have the following form:

$$c^E = \begin{pmatrix} c_{11} & c_{12} & c_{13} & 0 & 0 & 0 \\ c_{11} & c_{11} & c_{13} & 0 & 0 & 0 \\ c_{13} & c_{13} & c_{33} & 0 & 0 & 0 \\ 0 & 0 & 0 & c_{44} & 0 & 0 \\ 0 & 0 & 0 & 0 & c_{44} & 0 \\ 0 & 0 & 0 & 0 & 0 & c_{66} \end{pmatrix},$$

$$e = \begin{pmatrix} 0 & 0 & 0 & 0 & e_{15} & 0 \\ 0 & 0 & 0 & e_{15} & 0 & 0 \\ e_{31} & e_{32} & e_{33} & 0 & 0 & 0 \end{pmatrix},$$

and

$$\epsilon^S = \begin{pmatrix} \epsilon_{11} & 0 & 0 \\ 0 & \epsilon_{11} & 0 \\ 0 & 0 & \epsilon_{33} \end{pmatrix},$$

The resulting Christofell Matrix is of the form

$$\Gamma_{ij} = \begin{pmatrix} c_{44} + \frac{e_{15}E_x^2}{\varepsilon_{11}} & \frac{e_{15}^2 E_x E_y}{\varepsilon_{11}} & 0 \\ \frac{e_{15}^2 E_x E_y}{\varepsilon_{11}} & c_{44} + \frac{e_{15}E_y^2}{\varepsilon_{11}} & 0 \\ 0 & 0 & c_{33} \end{pmatrix} \tag{2.15}$$

The eigenvalues of this matrix correspond to terms that can be used to solve for, the acoustic velocity in each of the three wave propagation modes, while the corresponding

eigenvectors relate to the direction of particle displacement. Solving for the eigenvectors and eigenvalues of Γ gives:

$$x_1 = \begin{pmatrix} -E_y \\ E_x \\ 0 \end{pmatrix}, \lambda_1 = c_{44}, x_2 = \begin{pmatrix} E_x \\ E_y \\ 0 \end{pmatrix}, \lambda_2 = c_{44} + \frac{e_{15}^2}{\varepsilon_{11}}, x_3 = \begin{pmatrix} 0 \\ 0 \\ 0 \end{pmatrix}, \lambda_3 = c_{33}. \quad (2.16)$$

Out of the three mode the second mode's eigen value λ_2 contains e_{15} making it piezoelectrically excitable. The particle displacement defined by x_2 is in the x-y plane and will be directly aligned with the electric field, regardless of the orientation of the field with respect to the x-y plane. This mode is a pure shear thickness mode since the particle displacement is in the x-y plane and the wave propagation direction is in the z-direction. Both the other two modes, the shear mode (defined by x1 and λ_1) and the longitudinal mode (defined by x3 and λ_3), are piezoelectrically inactive. The second mode is the mode we seek since it is the thickness shear mode and can be excited by the electric field in the x-y plane. The acoustic velocity for this mode can be calculated from the following equation.

$$\nu_a = \sqrt{\frac{c_{44} + \frac{e_{15}^2}{\varepsilon_{11}}}{\rho}} \quad (2.17)$$

The theoretical piezoelectric coupling constant for the ZnO LFE resonator is given by

$$K^2 = \frac{e_1 5^2}{c_{44}\varepsilon 11} \quad (2.18)$$

The theoretical analysis have shown that if the electrode configuration is such that it generates an electric field in the x-y plane in the c-axis oriented ZnO, it is possible to generate TSM in c-axis oriented ZnO. This knowledge will help us to guide electrode configuration choices when designing ZnO resonator for TSM.

2.6 Solidly Mounted Resonator Configuration

Having analyzed the possibility of generation of TSM in ZnO thin film (we have now given the theoretical basis of the TSM in c-axis oriented ZnO), the next logical step is to identify the resonator configuration which confines this TSM acoustic wave, causing the buildup of

a standing wave in the piezoelectric film. That is the acoustic energy needs to be trapped within the piezoelectric film by providing acoustic isolation around the piezoelectric film. This can be done by providing high acoustic impedance mismatch between the medium surrounding the piezoelectric film and the film itself. The acoustic impedance is defined as

$$Z_n = \sqrt{\rho_n \cdot c_n} \tag{2.19}$$

where ρ_n is the film density and c_n is the appropriate stiffness parameter[38]. A traveling acoustic wave in the piezoelectric film is reflected back into the film by the high acoustic impedance mismatch at the boundary of piezoelectric film and the surrounding medium, thus acoustic energy is trapped within the piezoelectric film. Air has near zero density therefore its acoustic impedance is near zero. Thus, excellent energy trapping can be achieved in resonators whose surfaces are open to air or vacuum. The higher the energy trapped within the resonator structure, the better is the quality of resonance. Hence the quality factor Q (a common parameter used to characterize the strength of a resonator) is broadly defined as:

$$Q = \frac{Energy\ conserved\ per\ cycle}{Energy\ dissipated\ per\ cycle} \tag{2.20}$$

There exist many methods of estimating Q, which have been discussed in [22]. Among BAW resonators, The QCM has very high quality factor with Q values well in the tens of thousands. The QCM is made from a quartz plate which has completely free surfaces except for small wire electrodes contacting the edges of the crystal. This configuration allows air to be on both sides of the acoustic medium, and thus resulting in very good acoustic isolation. That is why a common approach to fabricating thin film bulk acoustic resonators is to have air on both sides of the thin film. Various other configurations are used for providing acoustic isolation to the thin film. Figure 2.3 illustrates three of the configurations through which acoustic isolation can be achieved with thin-film BAW resonators. The first two configurations require fabrication of air barrier beneath the piezoelectric film. This is both difficult to achieve and requires an additional and very expensive fabrication step. Furthermore, thin films of ZnO necessary to produce the very high frequencies desirable for higher orders of sensitivity would cause these devices to be extremely delicate. The solution

to this problem is to deposit the piezoelectric film onto a solid structure that mimics the acoustic impedance of air, which is referred to as a solidly mounted resonator (SMR). Newell first described the concept of SMRs in 1965 [26], in which an acoustic mirror (analogous to an optical Bragg reflector) is deposited beneath the piezoelectric crystal film, as shown in Figure 2.3 (c). I employ this configuration in order to develop a design that is both robust and easy to fabricate. Thus the solidly mounted resonator is our configuration of choice for

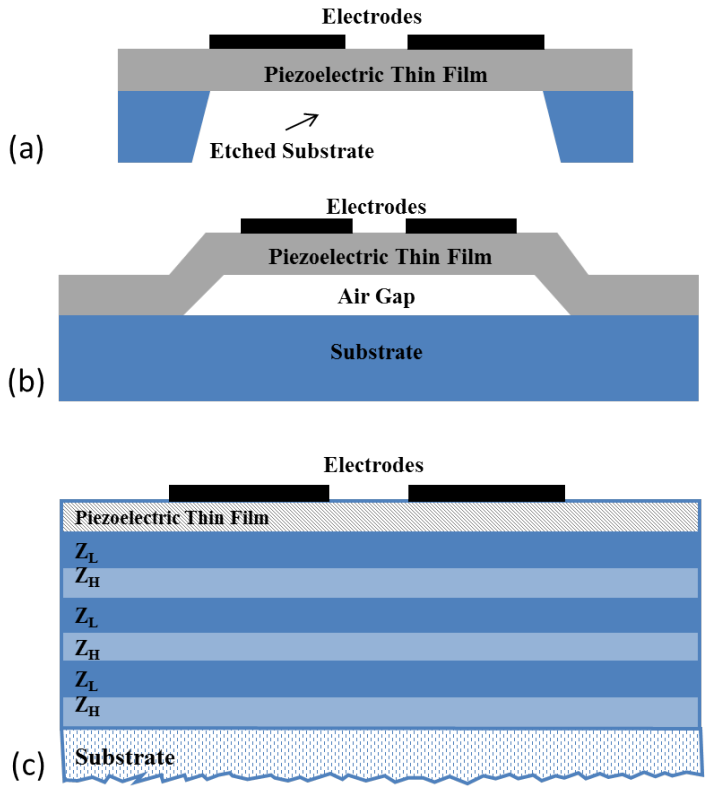

Figure 2.3: Thin film resonator configurations. a)Membrane resonator b)Air gap resonator c)Solidly mounted resonator

.

resonator design. The next section will discuss in detail the resonator design.

2.7 Design of Resonator

The primary objective of the resonator design is the design of a transducer which can be used as a liquid phase bio sensor. However, we are interested in designing a transducer that provides maximum information about the sample being probed by the transducer. The

TSM BAW resonator is better suited to measurements in liquid phase biosensor, and the longitudinal mode BAW resonators are capable of providing sensing information about thin films at the sensor surface in the dry or gaseous phase. Coupling the information obtained from both liquid phase and dry phase can add to the usefulness of the BAW resonator. Thus it is desire able from sensing point of view to have a device that is simultaneously resonant in both modes. Multiple modes excited in a single resonator structure would provide a multi-band resonator operating at non-harmonically related frequencies in the gigahertz range.

The theoretical background presented so far in this chapter outlines the salient features of our resonator (i.e. a ZnO based thin film solidly mounted resonator that supports TSM) and has also highlighted the major components of the design of resonator. The major components are a) Design of an acoustic reflector to provide acoustic isolation b) Deposition of high quality c-axis oriented ZnO piezoelectric film c) the design of a suitable electrode configuration to excite TSM in ZnO resonator.

In the following section we will visits these three components with the perspective of designing a multi-mode piezoelectric BAW resonator.

2.7.1 Multi-mode BAW Resonator

The first and foremost consideration is the excitation of both TSM and TE modes in a single structure. A common method is to use the inclined c-axis growth of ZnO to excite both modes using thickness excitation [24, 25].

In c-axis ZnO, the excitation of the TSM requires lateral-field excitation while the TE mode requires thickness excitation (as discussed in Section 2.5). Due to the different velocities of the TSM and TE modes, the corresponding wavelengths in any material are different. This implies that the reflector stack designed for the TSM may not be properly tuned for the TE mode, and vice versa. Therefore different devices with different electrode and reflector designs are needed to support the TSM and TE bulk acoustic modes with each device optimized for a single mode. Here, we present a single electrode geometry with one reflector design tuned to support both the TSM and TE modes in a single resonator

structure.

2.8 Electrode and Reflector Design

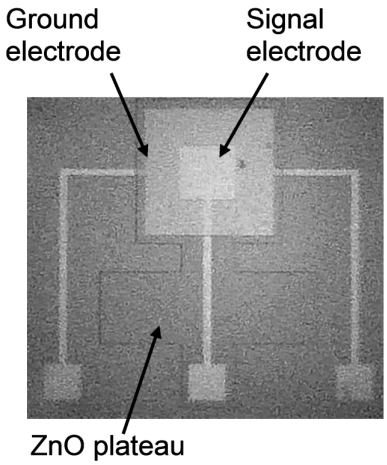

Figure 2.4: Photograph of fabricated device

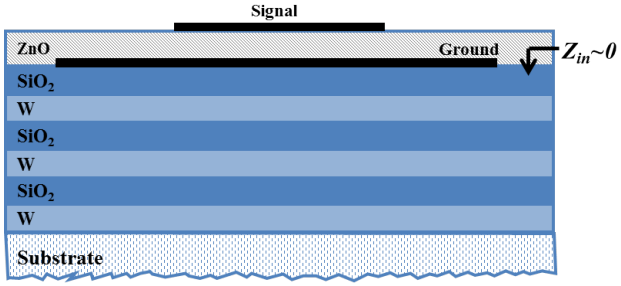

Figure 2.5: BAW resonator cross-section

A cross-section of our device geometry is shown in Figure 2.5. with a photograph of top view of our fabricated device shown in Figure 2.4. The device footprint is approximately $400\mu m$ x $400\mu m$ making it ideal for on-chip integration. This thickness-excitation configuration is traditionally used for longitudinal mode resonators since it provides electric field parallel to the c-axis of the ZnO (the region under the top electrode). However, in this electrode configuration the bottom electrode is larger than the top, a portion of the electric field is oriented in such a way that coupling to the shear mode will also exist due to a lateral electric field component, which will result in the excitation of TSM [27].

The acoustic reflector is constructed by a stack of quarter wavelength thick materials of alternating high and low acoustic impedance. The stack provides acoustic isolation by approximating air boundary at the piezo-stack interface. Each material layer in the reflector stack can be modeled as a transmission line. The impedance seen by the acoustic wave (Z_{in}) arriving at the boundary of the layer is given in [26]:

$$Z_{in} = Z_n \frac{Z_{n-1}\cos(\frac{2\pi}{\lambda_n}h_n) + jZ_n\sin(\frac{2\pi}{\lambda_n}h_n)}{Z_n\cos(\frac{2\pi}{\lambda_n}h_n) + jZ_{n-1}\sin(\frac{2\pi}{\lambda_n}h_n)}, \tag{2.21}$$

where h_n is the length of the transmission line (thickness of the layer), λ_n is the acoustic wavelength in the material of layer, Z_n is the characteristic acoustic impedance Z_n of the layer and Z_{n-1} represents the impedance on the other end of the transmission line (the impedance of the next layer). For quarter wavelength thick layer ($h_n = \lambda/4$), (2.21) reduces to

$$Z_{in} = Z_n \frac{Z_n}{Z_{n-1}}. \tag{2.22}$$

For a stack of alternating low and high impedance layers deposited on a Si wafer, the net Z_{in} for an acoustic wave incident on the piezo-stack boundary as shown in Figure **??**, can be written as follows:

$$Z_{in} = Z_l \cdot \frac{Z_l}{Z_h} \cdot \frac{Z_l}{Z_h} \cdot \frac{Z_l}{Z_h} \cdot \frac{Z_{Si}}{Z_h}. \tag{2.23}$$

If the ratio of Z_l to Z_h is less than one, then the input impedance seen by the acoustic wave will approach zero. This results in the overall stack approximating the effect of a pure air boundary, thus providing acoustic isolation from the substrate. The acoustic impedance for the TSM is given by $Z_{TSM} = \sqrt{\rho \cdot c_{44}}$ for a wave propagating along the c-axis, where ρ is the mass density and c is the appropriate stiffness constant. Similarly, the acoustic impedance of the TE is $Z_{TE} = \sqrt{\rho \cdot c_{33}}$. Since the acoustic impedance is a function of the stiffness coefficient, each material offers different impedance to different types of waves. Since the acoustic wave velocity is also dependent on c, the frequencies of the the propagating TSM and TE modes are different. Hence, the same set of reflector layers will reflect both the TSM and TE waves at different frequencies. A judicious choice of the resonator thickness can then be made to establish the TSM and TE modes within the reflector bandwidth for each mode, respectively.

Considering all the above mentioned parameters that affect the design of a reflector, we chose a combination of tungsten and silicon dioxide (W/SiO_2). The W/SiO_2 combination offers a very high impedance mismatch and, hence, a very wideband response. A MATLAB® script was written to simulate the reflector response based on (2.21). The quarter-wavelength thickness of each layer was chosen by an iterative simulation of the reflector response to give a reflectance band in the GHz range for both the TSM and TE modes simultaneously. The resulting reflection coefficients are shown in Figure 2.6. It is evident from these results that this reflector can reflect both the TSM and TE modes in the GHz range, provide the ZnO thickness is chosen appropriately.

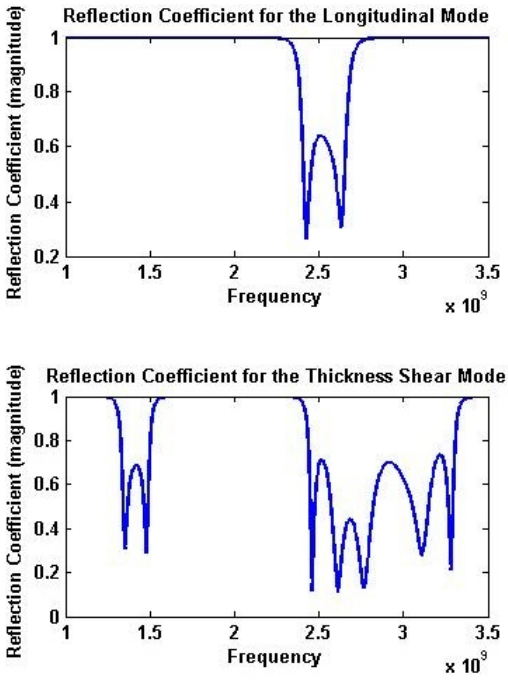

Figure 2.6: Simulated reflector response

In order to calculate the appropriate ZnO thickness to accommodate both modes of interest, we must determine the efficiency of the reflector in supporting both modes at a given ZnO thickness. We first recalculate the reflector response as a function of ZnO thickness, d (rather than frequency: $d = V/2f_0$). The two reflector responses are multiplied (equivalent to a logical AND operation), and the result is plotted in Figure 2.7. This new plot offers a metric by which to determine the reflection efficiency for *both* modes at a given

ZnO thickness; the closer this product is to 1, the more efficient the reflector will be in supporting both the TSM and TE modes. As shown in the shaded area of the plot, we target a ZnO thickness of approximately 1125nm +/- 80nm. In choosing the ZnO thickness using this metric, we have optimized the multi-mode support of the device.

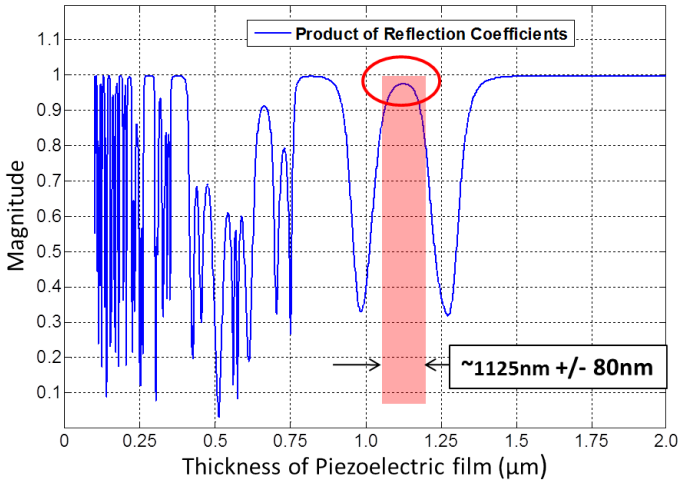

Figure 2.7: Calculated combined TSM and TE reflector response

2.8.1 Experimental Results

Approximately 50 devices were fabricated following the protocol described in [28] and measured using a Cascade Microtech Probe Station with an HP8753 Network Analyzer. The measured results shown in Figure 2.8 clearly show the multi-mode functionality of the single structure multi-mode device. Table 2.1 summarizes the measured frequencies, calculated acoustic velocities, and quality factors of each mode. In addition to the desired TSM and TE modes, this device also excites another mode that lies between the TSM and TE frequencies at about 1.5 GHz. We call this mode as "hybrid" mode and is discussed in detail in the next chapter. Since this is a non-harmonically-related mode to the desired TSM and TE modes, it could potentially have a variety of uses in communications and sensing applications.

The theoretical acoustic velocities on the TSM and TE modes are approximately 2800m/s

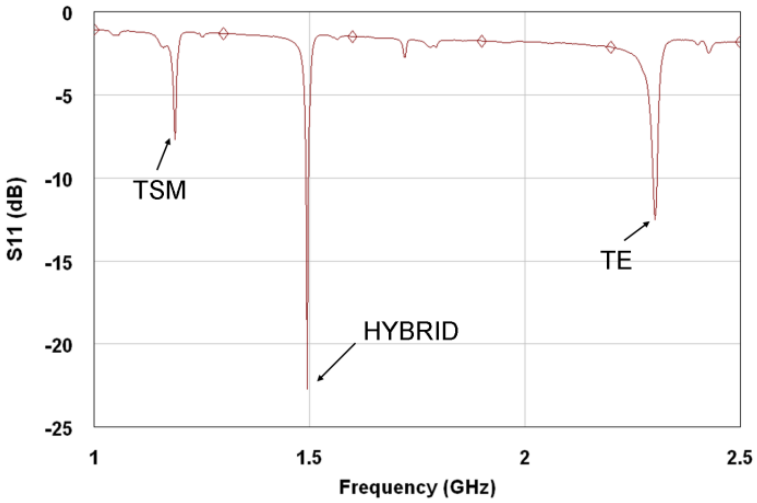

Figure 2.8: Measured S11 response of representative multi-mode device

Table 2.1: Multi-mode quality factors, resonant frequencies, and acoustic velocities

	Quality Factor			
Mode Type	Average	Range	Avg. Resonant Freq (GHz)	Avg. Velocity (m/s)
TSM	480	400-500	1.2	$\tilde{2}600$
Hybrid	700	500-800	2.3	$\tilde{3}320$
TE	910	800-1000	2.3	$\tilde{5}100$

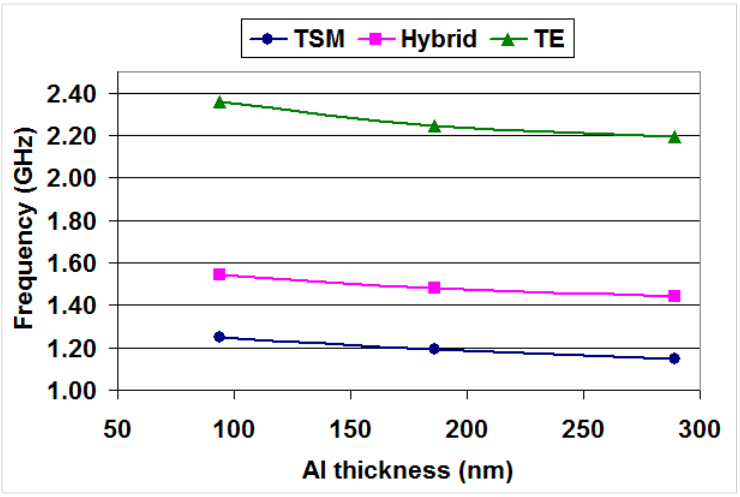

Figure 2.9: Measured top electrode thickness vs. resonant frequency

[22] and 6100m/s [20]. The measured velocities in this section are notably lower than the theoretical predictions because of the the inertial effects of the electrodes and energy trapping

phenomenon discussed in the next chapter. In a first-order approximation, the mass sensitivity of a device is proportional to the square of the unperturbed resonant frequency [11]. The frequency of the TE mode is more than twice that of the TSM, resulting in slightly over a 4x increase in mass sensitivity. The deviation of the TE velocity from the theoretical as compared to the TSM is, then, approximately 4x larger. The effect is confirmed experimentally and presented in Table 2.1. We also fabricated devices with varying electrode thicknesses to assess the affect of increased mass loading on the resonator surface. The resonant frequencies of all three modes decrease with mass-loading on the top electrode (Figure 2.9) showing that all three modes are mass sensitive. The sensing properties of all three modes will be characterized in detail in the next chapter.

2.9 Conclusion

In this chapter, the theoretical foundations of BAW resonator design were laid and were leveraged to develop a multi-mode resonator [29, 30]. A new method for characterizing a multi-mode reflection coefficient of an acoustic reflector is presented. We show that by multiplying the individual reflection coefficients of the TSM and longitudinal modes of an acoustic reflector allow for a simple determination of the appropriate piezoelectric layer thickness for the excitation and support of both modes. The measured resonant frequencies show the existence of the TSM and TE mode frequencies within the respective reflection bands of the reflector. In addition, the existence of a hybrid mode was observed in all devices, with resonant frequencies in between, and non-harmonically-related to, the TSM and TE modes. Novel design of the electrode geometry and reflector stack provided efficient excitation and support of all modes. All of the three modes are mass sensitive together these modes can provide a multi-frequency of probe of the bio sample at the transducer surface.

In the next chapter, we will extend further on the design of multi-mode device presented above. We will discuss energy trapping phenomenon, and detailed analysis of hybrid mode. Further, we will present the simulation and experimental characterization of this device. Such a characterization is essential to understand the behavior of the device and its usefulness as a biosensor.

CHAPTER III

MULTI-MODE DEVICE CHARACTERIZATION

3.1 Introduction

The focus of this chapter is to achieve a better understanding of the multi-mode device designed in the previous chapter. We use simulation, theory and experiment to gain an insight into the device behavior and characterize its response. The characterization and understanding is essential for making use of the device as a bio sensor. First, we look at the measured results presented in Table 2.1, specifically the discrepancy between the theoretical and measured mode velocities. We give simulation results that give us better understanding of the acoustic modes and point out the factors that may contribute toward deviation from theoretical predictions. Secondly, we look at the hybrid mode mentioned in the previous chapter. The hybrid mode is a unique and singular observation reported by our group for the first time [31]. Here we present the argument that the hybrid mode is possibly a coupled mode having both longitudinal and shear particle displacement. Detailed simulations, theory and experimental results are provided to support this argument. Lastly,we characterize the multi-mode device for different types of liquid samples. This will highlight the usefulness of the multi-mode device for liquid phase biosensing.

3.2 Resonance Frequency (Measured vs Theoretical)

In Table 2.1, we showed the resonance frequencies of the three modes and assuming the resonance was set up in the ZnO film only, the calculated mode velocities accordingly were found to be lower than the theoretical mode velocities in ZnO. The resonance frequency is the measurement parameter that gives an indication of deviation from the theoretically predicted behavior of the device. This deviation of the resonance frequency could be due to a number of factors that change the resonant behavior within the structure of the resonator including the change in mode velocity. In this section we aim to to look at the physical reasons behind the deviation of the resonance frequency from the theoretically predicted

value.

In the last chapter, we presented the requirements of generating TSM in thin film ZnO devices. We showed that we require electrodes to provide lateral electrical excitation of c-axis oriented ZnO film. A reflector stack is required to provide air like acoustic isolation to contain the acoustic modes within the ZnO film. Ideally we would want that the electrodes just provide us the desired electric field and the reflector provides perfect isolation and have no other effect on the resonance behavior of the device. Practically however the electrodes are a different material than the piezoelectric thin film and have some mass. Also, the electric field is not purely lateral and there are fringing fields present. All these factors which are due to the presence of physical electrodes may effect the resonator response. Similarly there are important difference in actual air and the reflector stack. Although the reflector stack can provide close to air acoustic isolation but unlike air it cant provide massless interface at the piezo-stack boundary. Therefore, it is essential to understand how the physical electrodes and reflector stack effects the resonator response. In the following lines we use finite element modeling of our multi-mode devices to explore these effects.

Finite element simulations using COMSOL Multiphysics® allows for extremely accurate simulations of highly complex physical systems by allowing for the inclusion of a variety of physical parameters and the interdependence of different types of physics (e.g. thermal effects as a result of electrical conduction).

COMSOL Multiphysics® provides a variety of high-level simulation modules including, but certainly not limited to, the Chemical Engineering Module, the AC/DC Module, the MEMS Modules, and a set of Multiphysics modules including heat transfer, electromagnetics, fluid dynamics, etc. Within the COMSOL user interface, a user can draw a desired structure from scratch or import a CAD file directly from a variety of CAD programs. Once a structure is defined, a user can define subdomain materials from a list of provided materials or define their own material by manually defining physical parameters like the stiffness matrix, the electrical conductivity, etc. Boundary conditions are then required to solve the PDEs using finite elements. COMSOL allows for a variety of bounday conditions depending

on the type of physics being simulated (e.g. mechanically free or rigid boundary for structural mechanics or a defined surface charge or electric potential for electrostatics). Once the simulation domain is fully defined (defined structure, subdomain settings, boundary conditions, etc.), there are a variety of analysis types available including static, transient, frequency response, eigenfrequency, and damped eigenfrequency analyses. Within each of these analysis types there exists a variety of solvers including, but not limited to, stationary, time dependent, eigenvalue, and parametric solvers. In addition to these available features, COMSOL allows for user-defined PDEs, integration with external software such as MATLAB, and a host of other far more complex features, descriptions of which are outside the scope of this thesis.

In these simulations, we employed the Structural Mechanics physics of the MEMS application module to simulate the piezoelectric excitation of ZnO. More specifically, within the structural mechanics module, we chose the Piezo Plane Strain module. In this module, we can include all applicable physics tensors for a material including the permittivity, piezoelectric coupling, and stiffness tensors.

The representative material tensors for ZnO (predefined in COMSOL) are:

$$\epsilon_r^S = \begin{pmatrix} 8.5446 & 0 & 0 \\ 0 & 8.5446 & 0 \\ 0 & 0 & 10.204 \end{pmatrix},$$

$$e = \begin{pmatrix} 0 & 0 & 0 & 0 & -0.480508 & 0 \\ 0 & 0 & 0 & -0.480508 & 0 & 0 \\ -0.567005 & -0.567005 & 1.32044 & 0 & 0 & 0 \end{pmatrix} \frac{C}{m^2},$$

$$c^E = \begin{pmatrix} 209.714 & 121.14 & 105.359 & 0 & 0 & 0 \\ 121.14 & 209.714 & 105.359 & 0 & 0 & 0 \\ 105.359 & 105.359 & 211.194 & 0 & 0 & 0 \\ 0 & 0 & 0 & 42.3729 & 0 & 0 \\ 0 & 0 & 0 & 0 & 42.3729 & 0 \\ 0 & 0 & 0 & 0 & 0 & 44.2478 \end{pmatrix} \times 10^9 Pa.$$

We use the eigenfrequency mode to visualize the particle displacement and stress profiles of the multi-mode device. The device cross section is shown in Figure 3.1. In order to reduce the computation load we exploit the symmetry of the problem. By using symmetries in a model its size can be reduced by one-half or more, making this an efficient tool for solving large problems.

Symmetry means that a model is identical on either side of a dividing line or plane. To take advantage of symmetry planes and symmetry lines, all of the geometry, material properties, and boundary conditions must be symmetric, and any loads or sources must be symmetric or antisymmetric. One can then build a model of the symmetric portion, which can be half, a quarter, or an eighth of the full geometry, and apply the appropriate symmetry (or antisymmetry) boundary conditions.

In Figure 3.1 we show the symmetry line of our problem. We simulate the one half of the structure to the left of the symmetry line and apply the symmetry boundary condition on the right most boundaries shown in figure.

As a first step we simulate the BAW resonator structure without the reflector, i.e. the ZnO piezoelectric film with electrodes. We have created a 850nm thick, c-axis oriented slab of ZnO. As shown in Figure 3.2, we set the ZnO to piezoelectric and the material orientation sets the $x-y$-plane of the simulation window equivalent to the $x-z$-plane of the ZnO. This gives us the desired c-axis orientation.

The results from this simulation give us some insights into the thickness shear mode profile. First the energy of the thickness shear mode is concentrated under the top electrode. This is interesting since in the previous chapter we argued that the electrical excitation of

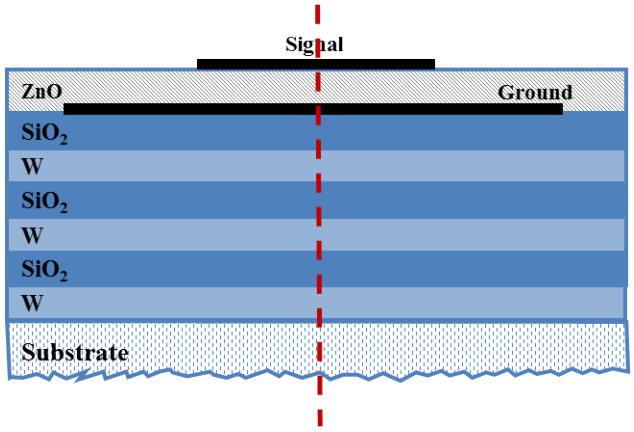

Figure 3.1: BAW symmetry condition for Finite Element simulations

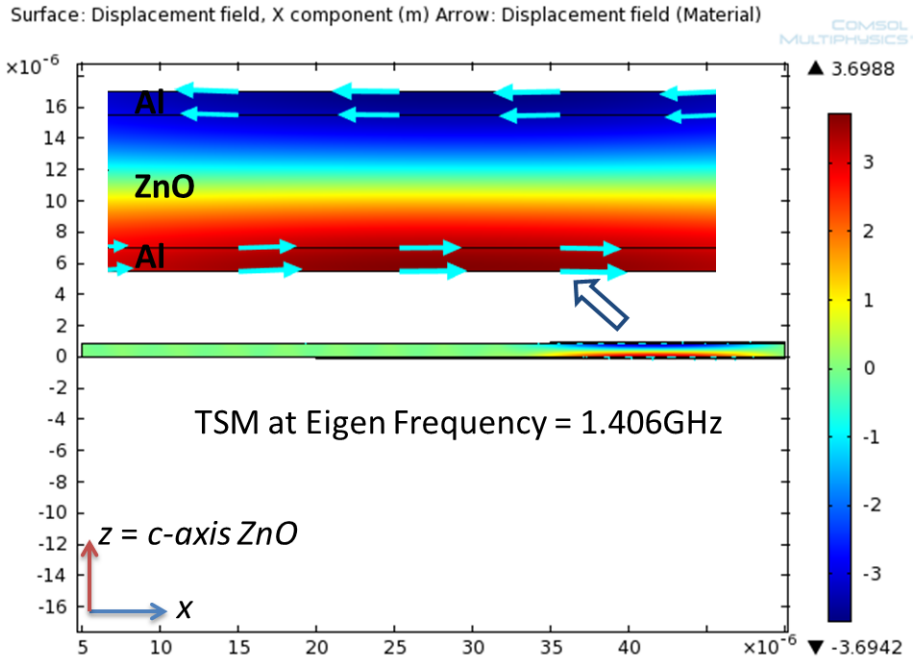

Figure 3.2: Thickness Shear Mode Displacement field x-component

the thickness shear mode is provided by the lateral component of the electrical field that lies outside the top electrode. The electrical field under the top electrode is aligned with the c-axis of the ZnO film and has negligible lateral component. The reason of TSM mode energy being concentrate under the top electrode is the energy trapping phenomenon. First, the particle displacement field is not confined with in the ZnO Piezoelectric film. It extends well into both the electrodes. We plot the particle displacement filed in the center of the

thickness shear mode vs the thickness (ZnO + Electrodes)of the resonator. We see that the plot traces half a wavelength representative of a standing wave of acoustic resonance. This implies that the total length that determines the resonance is not just the thickness of the piezoelectric film, rather it is the thickness of piezoelectric film plus the thickness of both the electrodes. For this simulation the 850nm is thickness of ZnO and the total thickness of both electrodes combined is 300 nm(35% of ZnO thickness). Usually the effect of electrodes can be ignored in thick films but approaching sub micron thicknesses for higher frequency resonators the electrodes thickness becomes significant compared to the thickness of the piezoelectric film. Thus the eigen frequency measured of fabricated devices and theoretically predicted according to equation **??**differ. We now take a look at how the reflector effects the behavior of TSM.

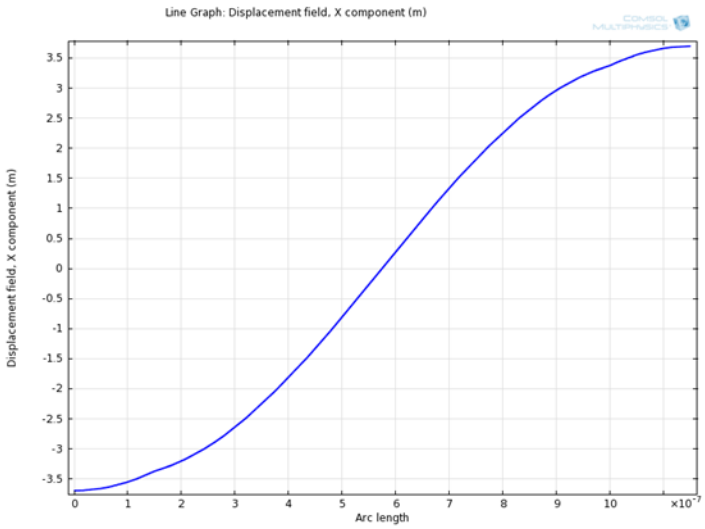

Figure 3.3: X-component of the Displacement field of TSM inside the resonator along the thickness

First, we look at the 2 layer reflector stack. We look for the eigen frequency which is concentrated under the top electrode and has displacement profile that matches the TSM. For the two layer case this eigen frequency corresponding to TSM falls at 1.365 GHz. Since the reflector stack tries to mimic air boundary by providing acoustic impedance close to zero but it does not provide zero mass compared to the air. Therefore, we may attribute the lowering of eigen frequency to the inertial loading of the reflector stack. In addition, the

simulation results show that the energy of the TSM extends well into the top layer of the reflector. Similar to the extension of the resonator's effective thickness due to the electrodes, we see further extension of the resonator thickness here. This extension of effective resonator thickness also contribute towards the lowering of eigenfrequency simulation. The reflector stack implemented in our resonator design presented in the previous chapter uses 6 layered reflector stack. It was also shown that with the increase in the number of layers the acoustic isolation provided by the stack improves. Therefore now we look at the simulation of 4 and 6-layered reflector stacks.

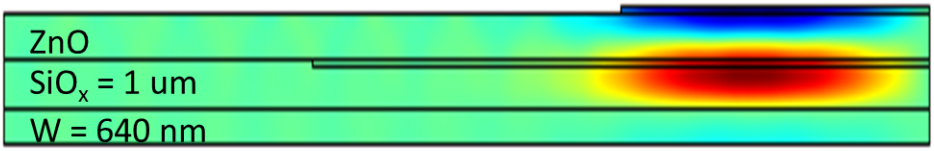

Figure 3.4: Thickness Shear Mode Displacement field with 2 layered reflector stack

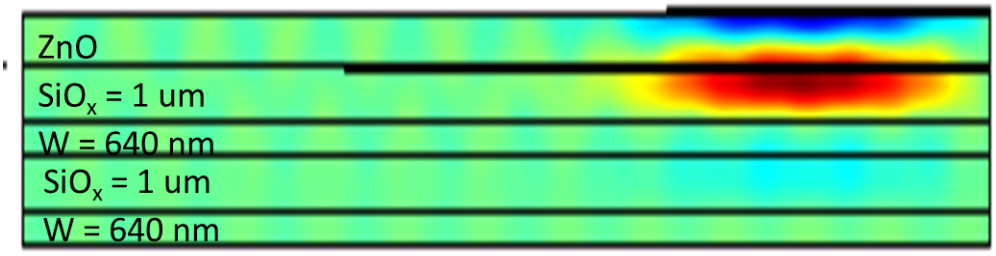

Figure 3.5: Thickness Shear Mode Displacement field with 4 layered reflector stack

The results of 6-layered and 4-layered stack are quite similar to the 2-layered stack. We see that the TSM is extended into the top layer of the reflector stack for both cases. The eigen frequency is lowered further compared to the 2-layer stack, but only by a small amount. This may be explained by the fact that the extent of the TSM energy profile extension into the top layer of the stack remains the same for all 2-layered, 4-layered and 6-layered reflector stack. Further it can be said that since the energy of the TSM mode stays only in the top layer of the stack the, the addition of more layers does not contribute towards inertial loading.

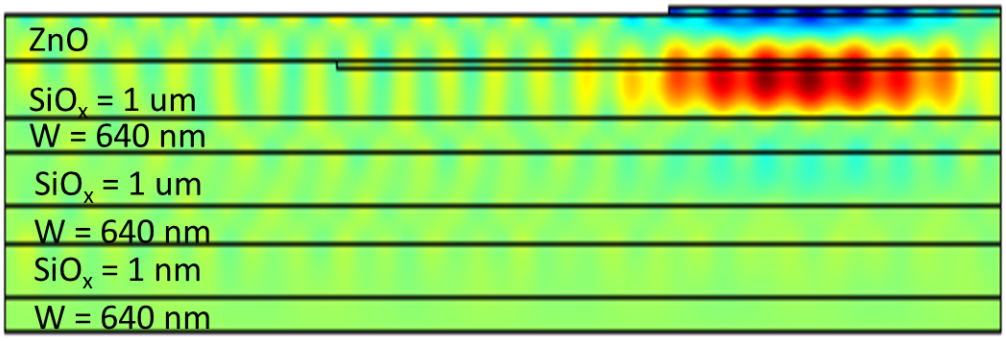

Figure 3.6: Thickness Shear Mode Displacement field with 6 layered reflector stack

The simulation results presented in this section highlighted the importance of top layer of stack. Since the TSM always extends into the top layer , the material properties and its dimensions may have impact on the resonance. We investigate the effect of the top layer thickness in the simulation results presented below. The reflector stack is designed such that each layer in the stack has quarter wavelength thickness. We have seen through simulations and experiments that with large number of layers such as 6 or more the change in an individual layer thickness does not affect the reflector response(i.e the coefficient of reflection stays close to 1). Therefore in the following simulations we explore the effect of increase in the thickness of the top layer. We changed the top layer thickness from 1 um to 1.2 um. The results are shown In Figures 3.7,3.8 and 3.9.

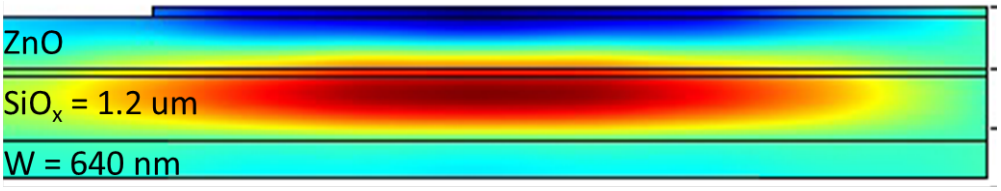

Figure 3.7: Thickness Shear Mode Displacement field with 2 layered reflector stack with the top layer extended

These results show that there is a significant decrease in resonance frequency for all three cases of extended top layer compared to non-extended layers. The extension of the energy profile of TSM into the top layer increases with the increase in the top layer thickness.

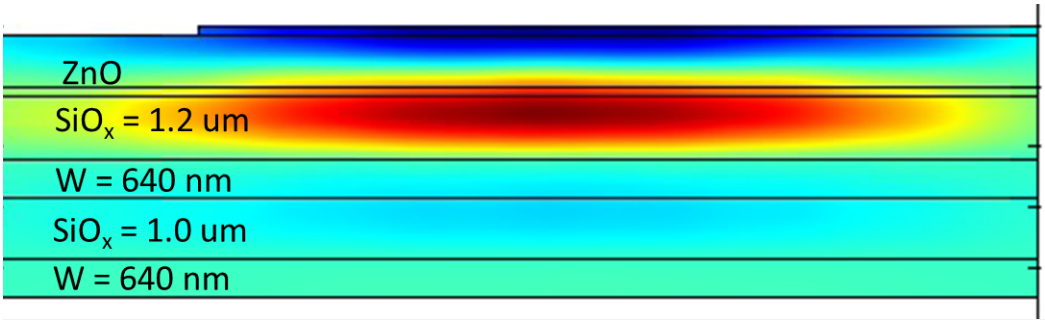

Figure 3.8: Thickness Shear Mode Displacement field with 4 layered reflector stack with the top layer extended

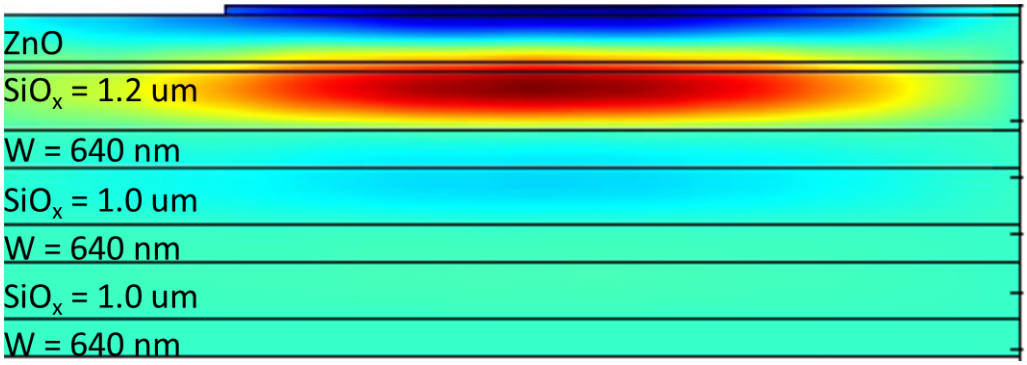

Figure 3.9: Thickness Shear Mode Displacement field with 6 layered reflector stack with the top layer extended

3.2.1 FEM Simulations-Summary

The results of FEM simulations point out several factors that affect the TSM and result in changing the resonance frequency from the theoretically predicted value. We learnt that the resonance frequency of the TSM mode is affected by the physical presence of electrodes in a way that the energy of the TSM mode is trapped under the top electrodes and extends into both electrodes and into the top layer of the reflector stack. The effective half wavelength of the resonance is more than the ZnO piezoelectric thickness. This increase in the half wavelength will directly result in the reduction of resonance frequency. Moreover, the mode velocity is not determined by the ZnO material parameters only, in fact it is now determined by piezoelectric material, the electrode material and the material of the stack's top layer. It is also evident that that the top layer of the stack has more impact than

the electrodes because the TSM energy profile covers almost all of the top layer. This fact suggests that the material properties of stack's top layer must be considered in the design of BAW solidly mounted resonators and these properties may be manipulated to alter the resonator response. Detailed investigation is needed to characterize and quantize the effects of reflector's top layer.

The fact that the energy of the TSM mode is concentrated under the top electrode is important from the sensing point of view as the sensitivity of TSM could only be in the areas where its energy is present. Therefore, the surface chemistry and target specific chemical sensitive layer should be immobilized on the top electrode.

3.3 Hybrid Mode

Hybrid mode that was observed in the measurements of our designed resonator is another type of discrepancy between theory and measurements. In this section, we will explore in detail the nature of hybrid mode with theory, simulations and experiments. This has been discussed in detail in our publication in the journal of applied physics [28].

A common way of verifying the existence of the TSM is to calculate the acoustic velocity of the mode from the measured resonant frequency and the device thickness. Assuming an ideal air-backed resonator (or air on top with a perfect acoustic reflector on the bottom), the velocity is simply calculated as , with d being the thickness of the device. Using bulk ZnO material properties in Rosenbaum [22], the calculated piezoelectrically-stiffened TSM velocity in ZnO is 2841m/s. Wu, et al., calculated the TSM velocities to be 2577m/s and 2733m/s for sputtered and epitaxial ZnO, respectively [32]. These velocities are theoretical calculations to which we can compare measured velocities to verify the TSM. Accounting for difference in ZnO material properties, deposition processes, parameters, and techniques, TSM velocities calculated from measurement should be within a few percent of these theoretical values.

Figure 3.10 shows a plot of the range of calculated mode velocities in ZnO devices [22, 31–35].

The reported values of the TSM velocity range from 2830-3368m/s. Using the same

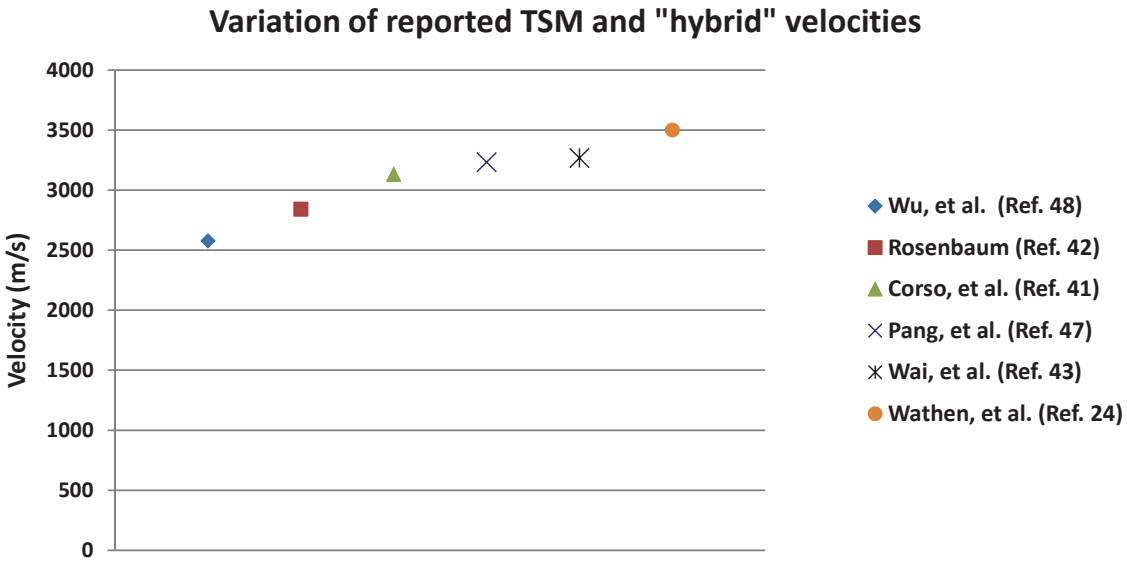

Figure 3.10: Variation of reported TSM and "hybrid" velocities

device structure as Corso, et al. [33], Wathen, et al. [31,36], observed a mode with a velocity of 3500m/s and an average Q of about 1900. With this velocity being nearly 1000m/s off from the quoted sputtered ZnO TSM velocity, this mode was deemed a hybrid mode and is thus not considered a pure TSM. The values in Figure 3.10 are all measured on devices employing sputtered ZnO. Using the sputtered ZnO TSM velocity (2580 m/s) [32] as a baseline, these values show a 20-36% deviation from the theoretical value. Even considering inherent differences in deposition parameters and ZnO crystallinity, it is difficult to attribute this amount of measured variance to an observed pure TSM.

It should be noted that only the ideal cases of thickness-excitation and lateral-field excitation generate the pure longitudinal and thickness shear modes, respectively. Thickness-excitation requires a piezoelectric film sandwiched between two electrodes to provide for an electric field parallel to the c-axis. Lateral-field excitation (LFE) requires electrodes to be on the sides of the film to provide a field orthogonal to the c-axis. In idealized models, these two configurations ignore fringing fields at the edges of the electrodes [22]. In real devices,

however, these fringing fields are unavoidable, resulting in a far more complex excitation field than in the ideal case. In addition to the desired pure mode, this impure field has the capability to excite a variety of acoustic modes, which may result in a far more complex resonant mode structure than the pure mode. This resulting mode structure may be considered a hybrid mode.

In this chapter, we present an experimental verification and a theoretical description of a hybrid acoustic mode presumably due to impure electrical excitation. We begin first with experimental observations of a resonant acoustic mode in two different electrode configurations on a ZnO SMR with an effective velocity that varies with ZnO thickness. A derivation of three governing partial differential equations that describe the coupling of longitudinal and shear particle displacement and the resulting piezoelectrically-generated potential is then presented as a potential explanation for the hybrid mode. Finite element simulations of the two experimental SMR device configurations are presented and an eigenmode analysis confirms the existence of a resonant coupled mode trapped in the ZnO film. The simulation results are then compared to those in experimentally measured devices. The experimental data is shown to agree with the simulated data within 1.5%.

3.3.1 Hybrid Mode-Experimental Investigations

The devices used in the studies shown in (Figure 3.10) have a variety of electrode configurations, ZnO thicknesses, and, if employed, reflector layer thicknesses. For simplicity, we wish to reduce the variability in our study to only two independent variables, i.e. the electrode configuration and the ZnO thickness. Each of two electrode configurations will be analyzed individually, so the experiment reduces further to two separate experiments, each depending only on the ZnO thickness. The goal of this section is to determine how the resonant frequencies and effective acoustic velocities vary with ZnO thickness.

Beginning with the method outlined in Corso, et,al. [33], we fabricated our own devices using the two well-defined electrode configurations shown schematically in Figure 3.11. The configurations were chosen specifically to excite the TSM in the devices using LFE. The acoustic reflector stack and ZnO layer shown in Figure 3.11 were fabricated using a Unifilm

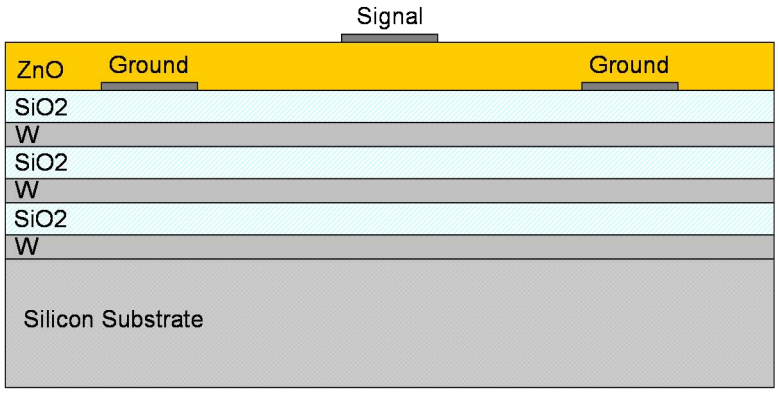

(a) Staggered configuration

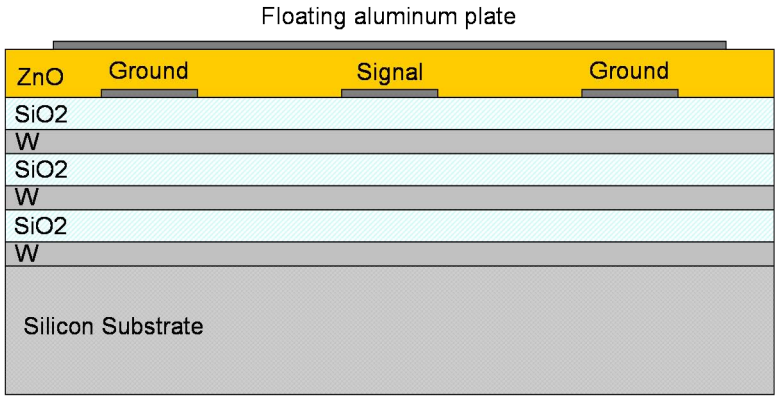

(b) Floating top electrode with buried electrodes

Figure 3.11: Electrode configurations

PVD sputtering system [33]. The stack is composed of alternating W and SiO_2 layers of 640nm and 1000nm thicknesses, respectively. The stack is then followed by the first Al electrode layer patterned using standard photolithography lift-off procedures and a CVC e-beam evaporation system. A scanning electron microscope image of the cross section of an actual device is shown in Figure 3.12 as an example of a fabricated stack.

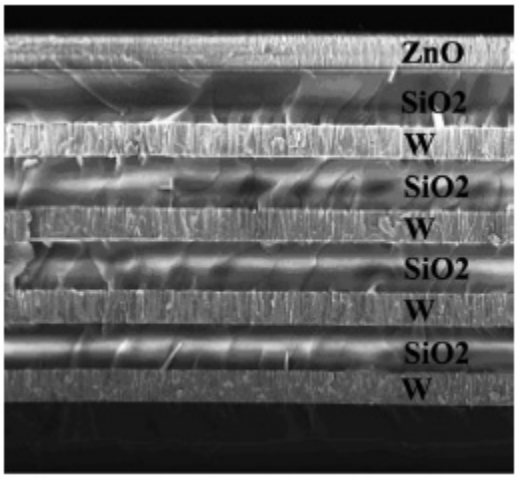

Figure 3.12: SEM cross section of fabricated SMR (fabricated by the author)

The electrodes start with a seed layer of 30nm of Cr on which 145nm of Al are evaporated. The ZnO is then RF sputtered in a 3% O_2 environment. As opposed to a uniform deposition, however, we deposit a highly non-uniform ZnO layer ranging from 1434nm at the center down to 1015nm at the edge of the 3-inch wafer. The top electrodes are then patterned in the same manner as the bottom. The final step is to etch the ZnO away in the appropriate locations to allow for access to the buried electrodes. The etch holes are patterned onto the wafer and a wet etch of DI water:HNO3:HCl (80:3:1) is used to remove the excess ZnO. The thicknesses of the ZnO and electrodes were all verified by a Tencor Alpha-Step Profilometer.

The one-port scattering parameters of the devices were captured on a HP 8753C Network Analyzer with a 85047A S-parameter test set. Cascade Microtech ACP40-GSG-400 probe tips were used to probe the devices. The measured resonant frequencies and effective velocities are given in Table 1.

Table 3.1: Measured Resonant Frequencies and Effective Velocites

	Buried Electrodes		Staggered Electrodes	
ZnO (nm)	f_0 (GHz)	Velocity (m/s)	f_0 (GHz)	Velocity (m/s)
1015	1.5496	3140	1.5482	3143
1111	1.4834	3296	1.4991	3331
1211	1.4374	3481	1.4614	3540
1324	1.4016	3711	1.4322	3792
1383	1.3731	3797	1.4123	3906
1434	1.357	3891	1.3398	3843

As shown in Table 3.1, for each electrode configuration, the resonant frequency decreases expectedly with increasing ZnO thickness. However, it is also apparent that the effective acoustic velocity increases with increasing ZnO thickness, continually diverging from the theoretically calculated TSM velocity in sputtered ZnO [32] of 2577m/s. In addition, Shockley, et al., showed the trapping of acoustic energy by the inertial loading of electrodes [**?**] resulting in a lower acoustic velocity below (or above) them. Examining the electrode configurations used in Figure 3.11, we see that the wave should then only be contained in the three regions of the ZnO that are directly below the top and above the bottom electrodes. In the case of the buried electrodes, the additional inertial loading due to the floating plate should further lower the acoustic velocity in the energy-trapping regions, thus lowering the resonant frequency for the same ZnO thickness as compared to the staggered configuration. Therefore, for any ZnO thickness, a resonant mode in the staggered configuration of Fig. 4(a) should continually have a higher effective velocity than that in the buried configuration of Fig. 4(c). As shown in Table 3.1, this effective velocity difference is, indeed, experimentally observed in all cases except the thickest staggered electrode configuration.

3.3.2 Hybrid Mode-Theoretical Treatment

Considering prior reports and the data gathered in Section II, it can be concluded that the observed mode was not the pure TSM we originally desired. With an effective velocity that increases with ZnO thickness, we can assume that the observed mode must be a kind of hybrid mode, possibly similar to that observed by Wathen, et al [31]. In this section, we describe the hybrid nature of the mode as a coupling between shear and longitudinal waves.

As a theoretical treatment of the hybrid modes in these devices, we will begin with the first principles of piezoelectric and acoustic phenomena as well as imposing some constraints on the desired solution set. First, we define the strain tensor and the electric field vector:

$$\mathbf{S} = \begin{pmatrix} S_1 \\ S_2 \\ S_3 \\ S_4 \\ S_5 \\ S_6 \end{pmatrix} = \begin{pmatrix} \frac{\partial u_1}{\partial x_1} \\ \frac{\partial u_2}{\partial x_2} \\ \frac{\partial u_3}{\partial x_3} \\ \frac{\partial u_2}{\partial x_3} + \frac{\partial u_3}{\partial x_2} \\ \frac{\partial u_1}{\partial x_3} + \frac{\partial u_3}{\partial x_1} \\ \frac{\partial u_1}{\partial x_2} + \frac{\partial u_2}{\partial x_1} \end{pmatrix} \tag{3.1}$$

$$\mathbf{E} = \begin{pmatrix} E_1 \\ E_2 \\ E_3 \end{pmatrix} = -\nabla\phi = \begin{pmatrix} \frac{\partial \phi}{\partial x_1} \\ \frac{\partial \phi}{\partial x_2} \\ \frac{\partial \phi}{\partial x_3} \end{pmatrix}. \tag{3.2}$$

For hexagonal crystals, like ZnO, the material tensors have the following form:

$$c^E = \begin{pmatrix} c_{11} & c_{12} & c_{13} & 0 & 0 & 0 \\ c_{11} & c_{11} & c_{13} & 0 & 0 & 0 \\ c_{13} & c_{13} & c_{33} & 0 & 0 & 0 \\ 0 & 0 & 0 & c_{44} & 0 & 0 \\ 0 & 0 & 0 & 0 & c_{44} & 0 \\ 0 & 0 & 0 & 0 & 0 & c_{66} \end{pmatrix},$$

$$e = \begin{pmatrix} 0 & 0 & 0 & 0 & e_{15} & 0 \\ 0 & 0 & 0 & e_{15} & 0 & 0 \\ e_{31} & e_{32} & e_{33} & 0 & 0 & 0 \end{pmatrix},$$

and

$$\epsilon^S = \begin{pmatrix} \epsilon_{11} & 0 & 0 \\ 0 & \epsilon_{11} & 0 \\ 0 & 0 & \epsilon_{33} \end{pmatrix},$$

where $\mathbf{c}^E$ is the stiffness tensor at a constant electric field, e is the piezoelectric coupling tensor, and ϵ^S is the permittivity tensor at a constant strain. We will use the following form for the constitutive relations:

$$\mathbf{T} = \mathbf{c}^E : \mathbf{S} - \bar{\epsilon}^S \cdot \mathbf{E} \tag{3.3a}$$

$$\mathbf{D} = \bar{\epsilon}^S \cdot \mathbf{E} - \bar{\mathbf{e}} : \mathbf{S}. \tag{3.3b}$$

For the particular configurations of the SMR devices being investigated, we search for solutions confined to a set of general restrictions for a wave propagating in the $x_1 - x_3$-plane as illustrated in Figure 3.13.

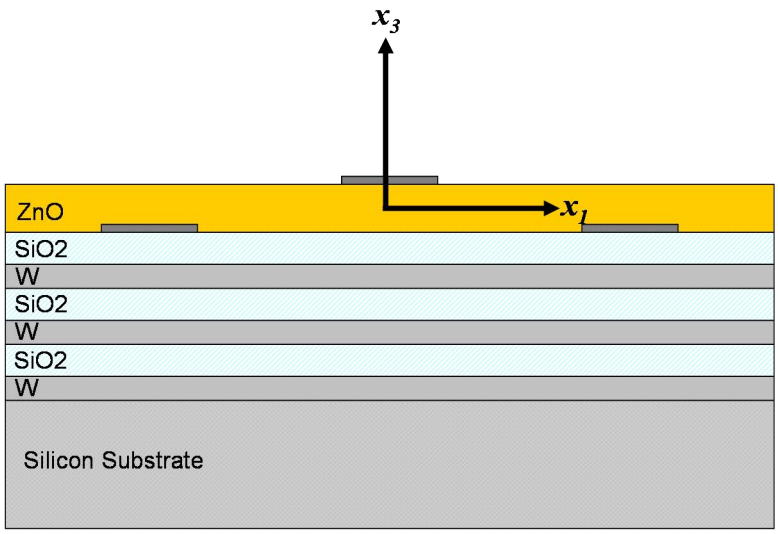

Figure 3.13: Device orientation

Primarily, we restrict the solutions to a 2-dimensional approximation with no field variations in x_2. Therefore, the desired particle polarization has components only in x_1 and x_3 directions (i.e. u_1 and u_3 are both nonzero, $u_2 = 0$) and the electric potential (ϕ) also

varies only in the $x_1 - x_3-$plane. Applying these conditions to (3.1), (3.2), and (3.3):

$$\mathbf{T} = \begin{pmatrix} T_1 \\ T_2 \\ T_3 \\ T_4 \\ T_5 \\ T_6 \end{pmatrix} = \begin{pmatrix} c_{11}\frac{\partial u_1}{\partial x_1} + c_{13}\frac{\partial u_3}{\partial x_3} + e_{31}\frac{\partial \phi}{\partial x_3} \\ c_{12}\frac{\partial u_1}{\partial x_1} + c_{13}\frac{\partial u_3}{\partial x_3} + e_{31}\frac{\partial \phi}{\partial x_3} \\ c_{13}\frac{\partial u_1}{\partial x_1} + c_{33}\frac{\partial u_3}{\partial x_3} + e_{33}\frac{\partial \phi}{\partial x_3} \\ 0 \\ c_{44}\frac{\partial u_1}{\partial x_1} + c_{44}\frac{\partial u_3}{\partial x_3} + e_{15}\frac{\partial \phi}{\partial x_3} \\ 0 \end{pmatrix} \tag{3.4a}$$

$$\mathbf{D} = \begin{pmatrix} D_1 \\ D_2 \\ D_3 \end{pmatrix} = \begin{pmatrix} -\epsilon_{11}\frac{\partial \phi}{\partial x_1} + e_{15}\frac{\partial u_1}{\partial x_3} + e_{15}\frac{\partial u_3}{\partial x_1} \\ 0 \\ -\epsilon_{33}\frac{\partial \phi}{\partial x_1} + e_{31}\frac{\partial u_1}{\partial x_1} + e_{33}\frac{\partial u_3}{\partial x_3} \end{pmatrix}. \tag{3.4b}$$

The application of Newton's Law and Gauss' Law for dielectrics to the stress and displacement tensors, respectively,

$$\nabla \cdot \mathbf{T} = \rho \frac{\partial^2 \mathbf{u}}{\partial t^2} \tag{3.5}$$

$$\nabla \cdot \mathbf{D} = 0 \tag{3.6}$$

and assuming time-harmonic behavior, we arrive at the following set of equations:

$$\frac{\partial T_1}{\partial x_1} + \frac{\partial T_6}{\partial x_2} + \frac{\partial T_5}{\partial x_3} = -\rho\omega^2 u_1, \tag{3.7a}$$

$$\frac{\partial T_6}{\partial x_1} + \frac{\partial T_2}{\partial x_2} + \frac{\partial T_4}{\partial x_3} = -\rho\omega^2 u_2, \tag{3.7b}$$

$$\frac{\partial T_5}{\partial x_1} + \frac{\partial T_4}{\partial x_2} + \frac{\partial T_3}{\partial x_3} = -\rho\omega^2 u_3, \tag{3.7c}$$

$$\frac{\partial D_1}{\partial x_1} + \frac{\partial D_3}{\partial x_3} = 0. \tag{3.7d}$$

Since we have assumed no particle displacement or field variations in the x_2 direction, we can eliminate the equation in u_2 and any partial derivatives with respect to x_2. Plugging (3.4) into (3.7), and grouping terms, we arrive at the following set of three coupled equations:

$$c_{11}\frac{\partial^2 u_1}{\partial x_1^2} + c_{44}\frac{\partial^2 u_1}{\partial x_3^2} + (c_{13}+c_{44})\frac{\partial^2 u_3}{\partial x_1 \partial x_3} + (e_{31}+e_{15})\frac{\partial^2 \phi}{\partial x_1 \partial x_3} = -\rho\omega^2 u_1, \tag{3.8a}$$

$$c_{44}\frac{\partial^2 u_3}{\partial x_1^2} + c_{33}\frac{\partial^2 u_3}{\partial x_3^2} + (c_{13}+c_{44})\frac{\partial^2 u_1}{\partial x_1 \partial x_3} + e_{15}\frac{\partial^2 \phi}{\partial x_1^2} + e_{33}\frac{\partial^2 \phi}{\partial x_3^2} = -\rho\omega^2 u_3, \tag{3.8b}$$

$$e_{15}\frac{\partial^2 u_3}{\partial x_1^2} + e_{33}\frac{\partial^2 u_3}{\partial x_3^2} + (e_{31}+e_{15})\frac{\partial^2 u_1}{\partial x_1 \partial x_3} - \epsilon_{11}\frac{\partial^2 \phi}{\partial x_1^2} - \epsilon_{33}\frac{\partial^2 \phi}{\partial x_3^2} = 0. \tag{3.8c}$$

These equations represent the governing set of coupled PDEs for the desired set of solutions. The complexity of these equations due to the inherent coupling of u_1 and u_3 as well as the coupled dependence on ϕ in the equation for u_1 in (3.8a) make an analytical solution to these equations difficult to obtain. But, there are several interesting qualitative features embedded in the equations that shed a bit more light on the coupling between the particle displacements.

First, let us consider that potential solutions include modes which are a superposition of LFE and thickness-excited waves. Applying the restrictions appropriate for each of the pure modes, we should observe the decomposition of the coupled PDEs into the wave equations for the pure modes. For a laterally-excited TSM, we require that only lateral particle displacement, i.e. u_1 components, exist. Further, for the ideal case, all variation of particle displacement in x_1 is eliminated, i.e. $\partial/\partial x_1 = 0$. Also, in LFE devices, a traveling piezoelectrically-generated potential does not exist [22]. Therefore, terms in u_3, terms involving the electric potential, and any terms with 2^{nd} partial derivatives with respect to both x_1 and x_3 are all zero. Under these ideal conditions, the only remaining equation is

$$c_{44}\frac{\partial^2 u_1}{\partial x_3^2} = -\rho\omega^2 u_1, \tag{3.9}$$

which is the fundamental wave equation for a propagating TSM in a c-axis oriented hexagonal crystal.

We now wish to see if the equations decompose into the pure longitudinal mode in ZnO. In this case, we will restrict the conditions to waves with particle displacement in u_3 only and with field variation in the x_3-direction. Therefore, all mixed partial derivatives are again zero. In contrast to LFE devices, an internal potential does exist in thickness excitation, and is in the direction of the excitation itself [22]. Therefore, the potential is

allowed to vary only in x_3. Equation (3.8c) thus reduces to

$$e_{33}\frac{\partial^2 u_3}{\partial x_3^2} = \epsilon_{33}\frac{\partial^2 \phi}{\partial x_3^2}. \tag{3.10}$$

We plug this into (3.8b) and arrive at the fundamental wave equation for the longitudinal mode:

$$\left(c_{33} + \frac{e_{33}^2}{\epsilon_{33}}\right)\frac{\partial^2 u_3}{\partial x_3^2} = -\rho\omega^2 u_3, \tag{3.11}$$

The decomposition of the coupled PDEs into the solutions for the pure TSM and longitudinal modes provides verification that the derived equations are, in fact, describing the coupling between longitudinal and shear particle displacements that reduce to the pure modes provided we apply the appropriate restrictions.

3.3.3 Hybrid Mode-Finite Element Modeling

Given the complexity of the governing equations derived above, we now use a finite element simulation package, specifically COMSOL Multiphysics® , to gain further insight on the potential solutions of (3.8). Using the MEMS multiphysics module of COMSOL, we can simulate the piezoelectric generation of acoustic waves and examine resulting particle displacements, potentials, etc. In this section, we simulate SMR device response by employing the eigenfrequency simulation in COMSOL to determine the eigenmodes of our experimental structures used in Section 3.3.1 (Fig. 3.11).

We use the default ZnO stiffness, permittivity, and piezoelectric coupling tensors in COMSOL as the material parameters. We first define the materials in each subdomain of the simulation (i.e. W, SiO_2, Si, and c-axis ZnO). Next, the mechanical boundary conditions of every boundary are defined as free-moving boundaries. Referring to Figure 3.11, the boundaries of the electrodes defined as "ground" were set to ground in the simulation. The "signal" electrodes were set to floating ($\hat{\mathbf{n}} \cdot \vec{D}_2 = \rho_s$) as this allows for the eigenfrequencies of the solutions to correspond directly to the frequency of the applied electrical excitation. In the experimental devices, the electrical excitation occurs only at the ground and signal electrodes. No other boundaries are physically connected to either the ground or the signal paths. Therefore, all other metal boundaries must be regarded as having floating potentials

as well. To accommodate this effect, we set all tungsten boundaries and the floating plate to a floating condition. All remaining boundaries were set to electrical continuity [i.e $\hat{\mathbf{n}} \cdot (\vec{D}_2 - \vec{D}_1) = 0$].

With regards to physical dimensions, the simulated structures are identical to our experimental structures presented in Section 3.3.1. The W layers are 640nm, the SiO_2 layers are 1000nm, the electrodes are 175nm thick and 40μm wide, and the lateral gap between the electrodes is 20μm. The overall structure is 200m wide and the floating plate in Figure 4(c) is 180μm wide. The initial ZnO thickness is 1015nm. Later, we increase the ZnO thickness to match the experimental thicknesses shown in 3.1 and observe the resulting eigenmodes.

Considering the conditions prescribed in Section 3.3.2, we desire a mode with energy mostly contained within in the ZnO layer and propagates only in the $x_1 - x_3$-plane. Further, due to the energy trapping considerations described in Section II [**?**], the mode should also be trapped laterally within the confines of the electrodes. Due to structural imperfections and the physical necessity for finite Q, some energy leakage outside of these regions is expected and will be present in all satisfactory solutions. For a ZnO thickness of 1015nm, the mode profiles that satisfy these criteria are shown in Figures 3.14 and 3.15.

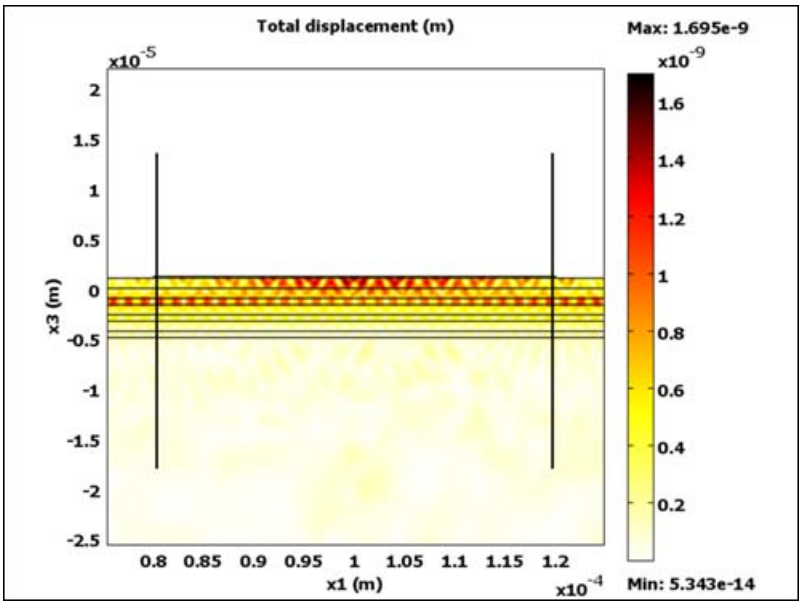

Figure 3.14: Particle displacement magnitude in staggered electrode configuration (solid vertical lines show edges of center top electrode in Figure 4(a))

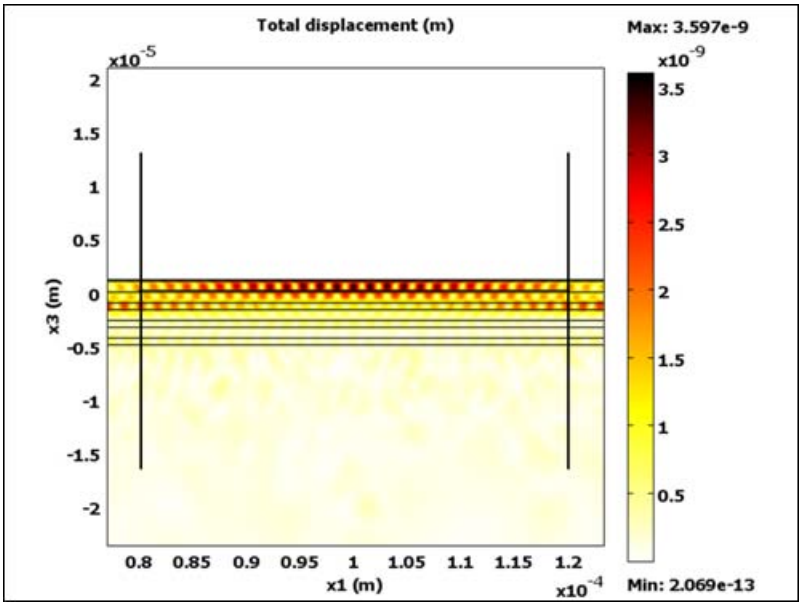

Figure 3.15: Particle displacement magnitude in electrode configuration with a floating top plate (solid vertical lines show edges of center buried electrode in Figure 4(c))

Since these are the only simulated modes present in the structure that satisfy our criteria described above, we now search for these modes in ZnO layers of varying thickness. The criteria for the desired mode structure are identical for each ZnO thickness. We simulate the devices structure for each of the ZnO thickness shown in 3.1. Table 3.2 shows a comparison of the resulting simulated eigenfrequencies and effective velocities for this mode and the experimental results as the ZnO thickness varies. This data is also displayed graphically in Figures 3.16 and 3.17.

Expectedly, like the experimental data, the simulated frequency of the mode decreases with increasing ZnO thickness. Again like the experimental results, the effective velocity *increases* with increasing ZnO thickness. Notably, the simulation results agree with the experimental results within 1.5%. This high level of agreement is further confirmation that the observed mode is not pure but, in this case, is a coupled *hybrid* mode between the longitudinal and shear particle displacements in the ZnO. An interesting observation is that, for all ZnO thicknesses, the simulated staggered electrode configuration has a higher effective velocity than the floating plate configuration (confirming the energy trapping phenomenon)

Table 3.2: Simulated and Measured Frequencies and Effective Velocities

	Buried Electrodes					Staggered Electrodes				
ZnO	Simulated		Measured			Simulated		Measured		
nm	GHz	m/s	GHz	m/s	% diff	GHz	m/s	GHz	m/s	% diff
1015	1.5476	3141	1.5496	3145	0.15	1.5497	3146	1.5482	3143	0.09
1111	1.4658	3257	1.4834	3296	1.18	1.5034	3341	1.4991	3331	0.29
1211	1.4430	3495	1.4374	3481	0.4	1.4645	3547	1.4614	3540	0.21
1324	1.3811	3657	1.4016	3711	1.46	1.4308	3789	1.4322	3792	0.1
1383	1.3678	3783	1.3731	3797	0.39	1.4153	3915	1.4123	3906	0.21
1434	1.3507	3873	1.357	3891	0.46	1.3430	3852	1.3398	3842	0.24

with exception to the thickest ZnO layer. Even this apparent anomaly as previously mentioned in Section 3.3.1 agrees with experiment within 0.24%.

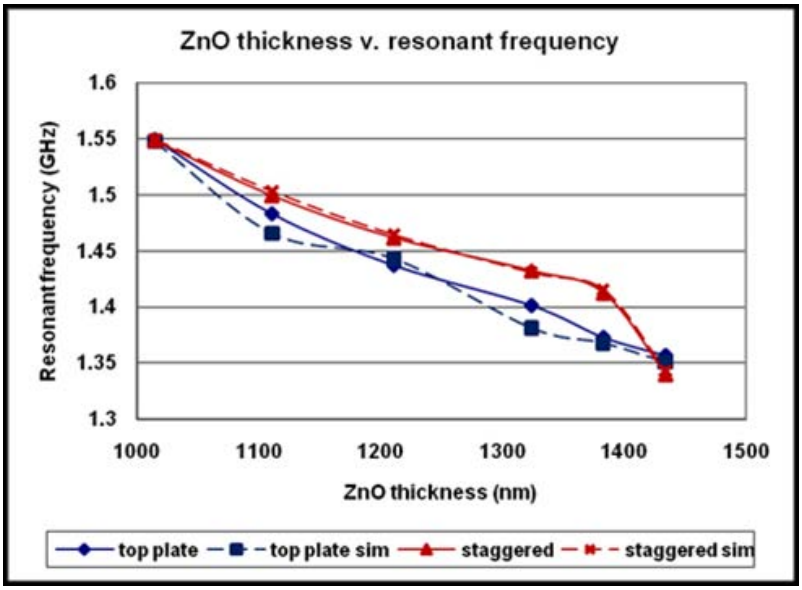

Figure 3.16: Measured and simulated resonant frequencies ("top plate" refers to the floating top plate configuration)

3.3.4 Hybrid Mode-Model Validation Using an Alternate Structure

Wathen, et al. [31] observed what was deemed a *hybrid* mode with an effective velocity of 3500m/s. The device structure used in that study is fundamentally different than the two used here in Section II and is shown schematically in Figure 3.18. This structure is identical to that used in Corso, et al. [33] Due to the assumed hybrid nature of the observed mode,

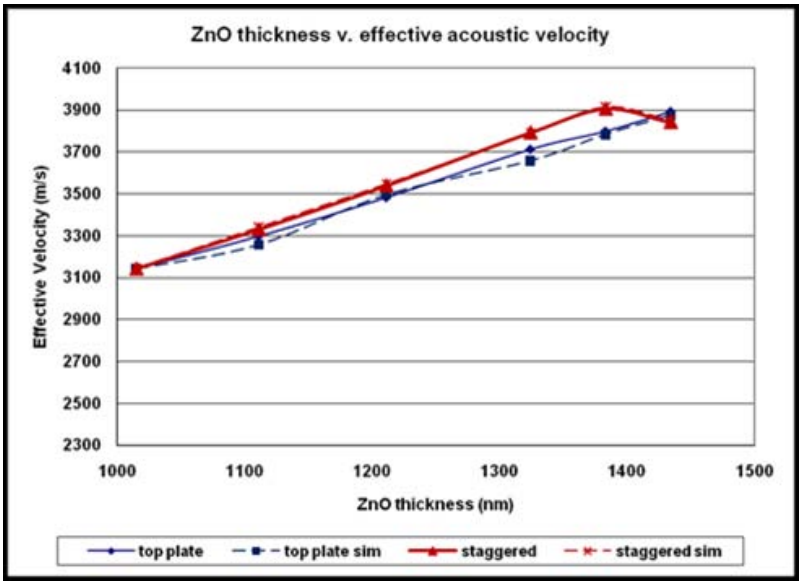

Figure 3.17: Measure and simulated effective velocities ("top plate" refers to the floating top plate configuration)

we now simulate the exact device structure used in the 2009 study as a validation of the models presented in Sections 3.3.2 and 3.3.3.

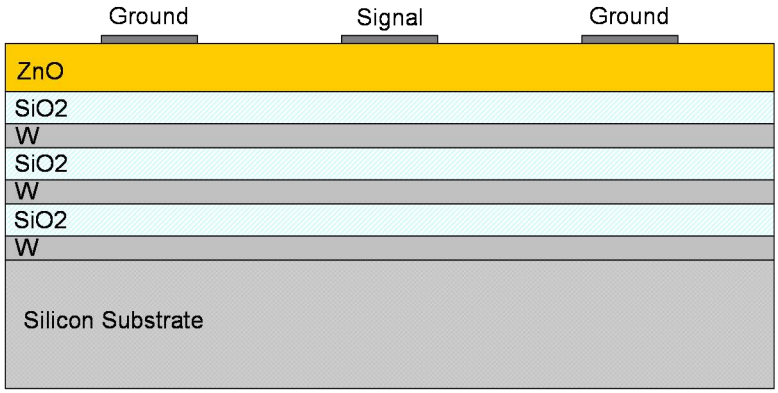

Figure 3.18: Typical LFE structure

The COMSOL subdomains and boundary conditions are set up identically to those presented in Section 3.3.3. Dimensionally, the structure is identical to that used in Wathen, et al. [31] An eigenfrequency simulation is used to find modes of a coupled nature in the ZnO layer and trapped under the electrodes. With a 680nm thick ZnO layer and 40μm wide electrodes, the aspect ratio under the electrode is nearly 60:1. This extreme aspect ratio

results in an extraordinary number of eigenfrequencies of the structure due to the number of possible spatial harmonics of the solutions. However, we find only one solution in the simulation that acceptably satisfies the conditions prescribed in Sections 3.3.2 and 3.3.3. The simulated eigenfrequency of this mode was 2.594GHz with the measured frequency in Wathen, et al. equal to 2.588GHz. The simulated effective velocity equaled 3527m/s with the measured equal to 3519m/s. The relative difference between the simulation and measurement, then, is equal to 0.2%. This alludes to a high confidence in the validity of the model presented in this study for describing the observed modes in the literature as a type of hybrid mode comprised of coupled longitudinal and shear particle displacements.

3.3.5 Hybrid Mode-Summary

Historically, there has been a large discrepancy between measured and theoretical velocities of the TSM in ZnO bulk acoustic resonators, as presented in Figure 3.10. We present an experimental verification of the discrepancy in ZnO SMR structures with two different electrode configurations. The ZnO thickness varied from 1015nm to 1434nm and the effective acoustic velocity through the thickness was found to increase with increasing ZnO thickness. A 2D theoretical analysis from the first principles of piezoelectric wave propagation has been presented. We show the possibility of the existence of a hybrid acoustic mode with coupled longitudinal and shear particle displacements. Finite element simulations of our experimental device structures show eigenmodes in the ZnO layer that satisfy the criteria of vertical and lateral energy trapping and a coupled mode structure. The eigenfrequency of the trapped mode at each thickness was used to calculate the effective velocity for that mode. These simulated velocities are within 1.46% of the experimentally measured velocities. We then validated the model by simulating a previously reported "hybrid" mode structure. The simulation results of this alternate device structure are within 0.2% of experimental measurements. We believe that this is a first step toward properly explaining the frequent discrepancy between measured and theoretical TSM values by way of a *hybrid* acoustic mode.

From a sensing perspective, it is evident that with the proper surface chemical treatment,

this mode will provide more information about a sample than just the pure modes. One thing to note, however, is that the coupled nature of the particle displacement is expected to degrade device performance in a liquid sample as the longitudinal component is radiated into the fluid. Whatever the consequence of a liquid sample, however, the addition of this mode into the variety of modes available for use increases the diagnostic power of these devices.

3.4 Multi-Mode Device Experimental Characterization

We conducted some experiments to characterize the response of our multi-mode device designed and described in the previous chapter. For using a resonator as a sensor its response must be characterized for different kinds of input stimulus to establish its sensing capability and for calibration purposes. We present here a preliminary characterization with a set of experiments to investigate the response of multi-mode device to viscous and conductive liquids.

3.4.1 Viscous and Conductive Liquid Measurements

Primarily we are concerned with the characterization of the TSM, since it is more useful for liquid phase biosensing. For viscous liquid measurements we use glycerol/DI water mixtures, with concentrations of 0%, 5%, 10%, and 15%, on the multi-mode devices. These glycerol/DI water mixtures produce conditions with less viscous to more viscous loading with increasing concentration of glycerol. The S11 parameter measured by the network analyzer for these glycerol/DI water mixtures is shown in Figure 3.19.

The resonance frequency in the S11 plot is the minimum of the resonance characteristics and is called as S11-frequency. Other than S-parameters, a more common way of characterizing resonator response is through analysis of impedance response of the resonator. The use of impedance response stems from QCM which has been studied in detail for its response to various types of surface load**??**. Two characteristic features extracted from the impedance response are the series and parallel frequency. The maximum of the impedance response is associated with the parallel resonance frequency and the minimum is associated with the series resonance frequency. Detailed analysis of series and parallel resonance frequencies

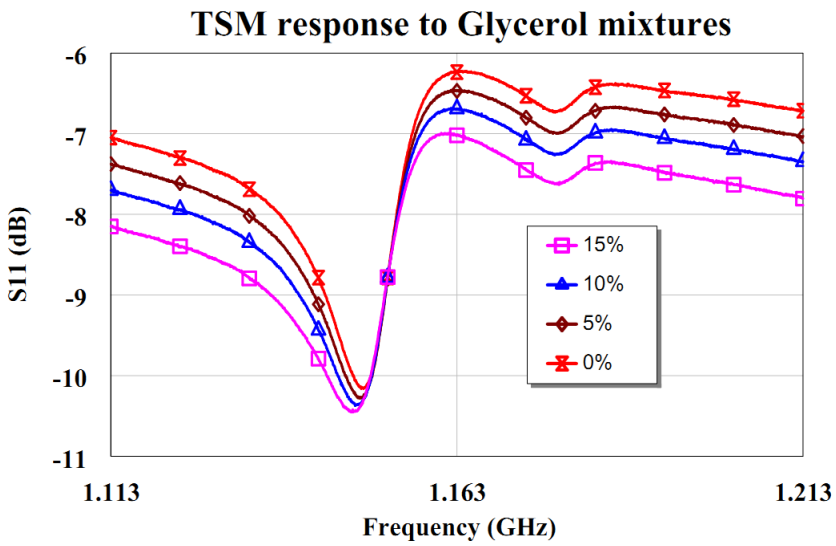

Figure 3.19: S11 parameters of TSM in multi-mode device under glycerol loading.

for BAW resonators and in particular for QCM is given in [37] by Lucklum et al. They deduce through experimental evidence that both series and parallel resonance frequencies shift due to surface loads but the parallel resonance frequency is effected by external capacitance much more than the series resonance frequency. Stray capacitances often add to the external capacitance of the resonator and are hard to control, therefore for sensing mechanical properties of surface load the series resonance frequency is better suited than the parallel resonance frequency. Whereas the parallel resonance frequency may be used to get a measure of the electrical properties of the surface load.

The impedance response can be obtained by converting the s-parameters using mathematical relations. Our devices being one port, we extract the one port z-parameter(z_{11}) from the one port S-parameters (S_{11} which is a complex quantity).

$$z_{11} = \frac{1 - |s_{11}|^2}{1 - 2 * Re(s_{11}) + |s_{11}|^2} + j\frac{2 * Im(s11)}{1 - 2 * Re(s_1 1) + |s_{11}|^2}. \tag{3.12}$$

We can use this relation to convert the s-parameter response for glycerol measurements shown in Figure 3.19 to Z-parameters.

The quantitative relationship of surface load changes to the resonator is provided in terms of frequency shift using Equation 2.11. This equation predicts a negative shift in the

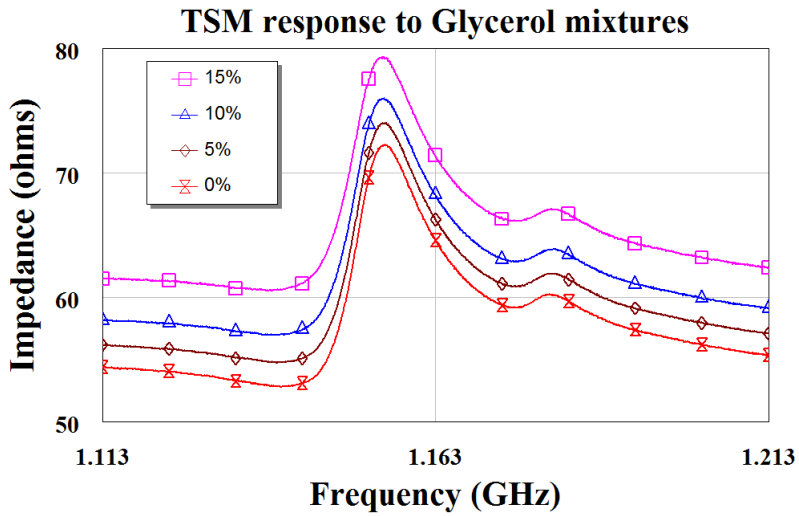

Figure 3.20: Impedance magnitude of TSM in multi-mode device under glycerol loading.

resonance frequency with the increasing viscosity of the liquid medium at device surface. The shift in resonance frequencies due to the glycerol mixture loading is shown in Figure 3.21.

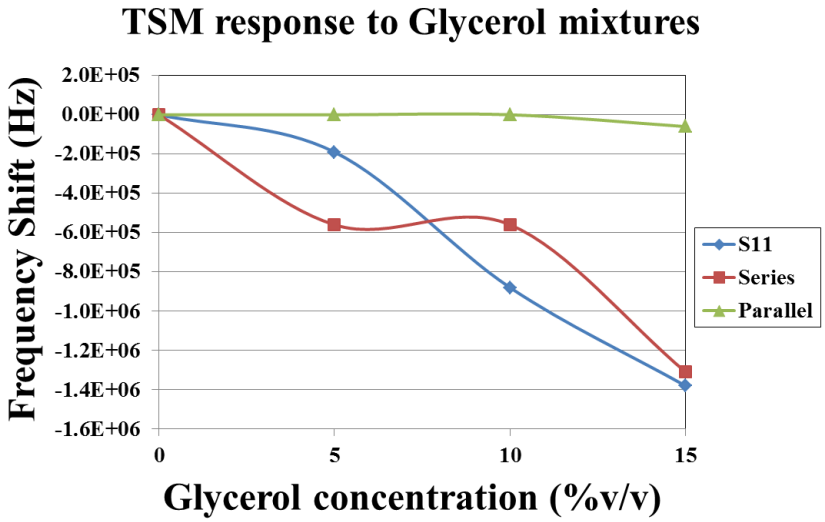

Figure 3.21: Frequency shifts of the TSM mode under glycerol loading

Here we see that the S11-frequency and the f_s both show lowering of frequency with increasing viscosity. However the parallel resonance frequency does not lower by the same

amount as the other two frequencies. These measurement results stand on their own and it is very difficult to compare them against any standard types of curves for viscous loading or against theoretical equation. The reason behind is that even though QCM is kind of a *'gold standard'* for TSM devices. The structure of the QCM is more close to the membrane devices, besides being very low frequency device. Thus there may be inherent differences in how the frequency shifts of TSM in thin film SMR devices behave. Additionally the devices presented here are much smaller than QCM and also operate at much higher frequency. The response scaling due to the frequency and size may not be a linear function. Similarly the theoretical equations such as Equation 2.11 are also derived for membrane type resonators and therefore the SMR type devices may not follow these equations precisely.

In addition to resonance frequency another commonly used parameter for resonator characterization is the quality factor Q. Figure 3.22 shows the shift in the Q of the multi-mode devices in response to varying viscosity glycerol/DI water mixtures. The Q has been calculated using the equation given below. The Q factor of the multi-mode devices is heavily reduced due to liquid loading. We can see that with the device already under liquid loading the increased concentration of glycerol does not affect the Q by a large factor and it is difficult to point out any definite patterns in the Q with increasing viscosity.

$$Q = \frac{f_0}{\Delta f_{-3dB}} \tag{3.13}$$

and

$$Q = \frac{f}{2}\frac{d\angle Z}{df} \tag{3.14}$$

where $f = f_s$ or f_p.

Conductive Liquid Measurements Since the resonator gives out electrical response, the conductivity of the medium containing the target molecule is an important property to be characterized. Given the fact that most biological mediums are conductive (blood, urine etc), it becomes more important to have a measure of the device response under varying conductivity conditions. Therefore, we characterize our devices with solutions of varying conductivity. The variation in conductivity is achieved by varying the salinity

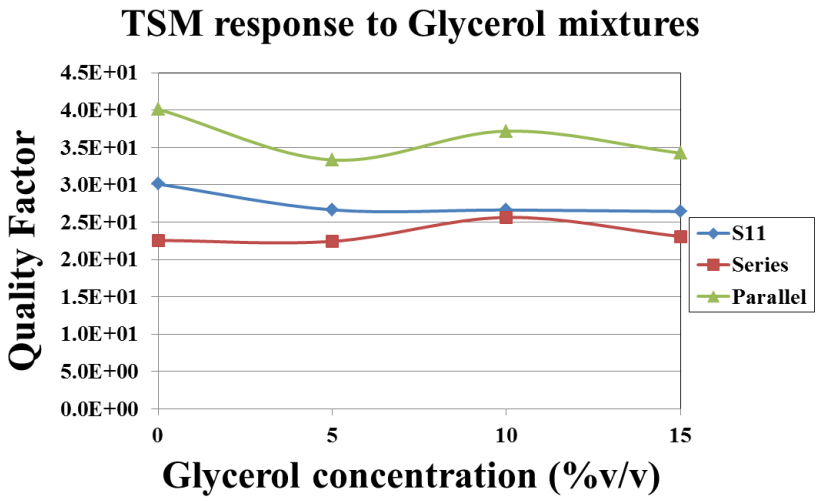

Figure 3.22: Quality factors of TSM mode under glycerol loading

of the medium. We use solution of NaCl in water with molarities varied from 0M to 0.1M. It is important to note the experimental protocol for the salinity measurements. The saline mixtures were all measured on the exact same device *in order* from lowest to highest concentration. After each measurement, the device was rinsed in DI water, and the next sample was measured. The measured data in S11 and impedance form is present in Figures 3.23, and 3.24.

Discussion of TSM Salinity Measurements First thing to notice about salinity measurements is that the results of 0.1M and 0.05M are vastly different from the other concentrations. Overall there is a decrease in the resonance frequency and in the quality factor with the increase in molarity for all concentration but for 0.1M and 0.05M there is 'amplified' change in Q and frequency shift. We discussed earlier in this section that the parallel resonance frequency is more sensitive to electrical changes and the series resonance frequency is more sensitive to mechanical changes of the surface load. However, here we see that the parallel frequency shifts are much smaller than the series frequency shifts. The salinity experiments that we are doing here use a single device for all molar concentration, this may lead to a build up of a salt layer on top of the devices specially for higher concentrations.

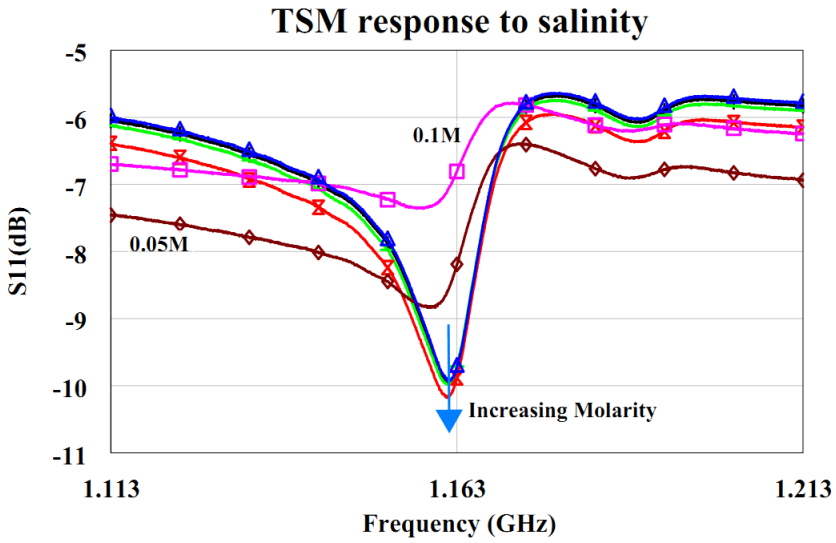

Figure 3.23: S11 of the shear mode in multi-mode device under saline solution loading.

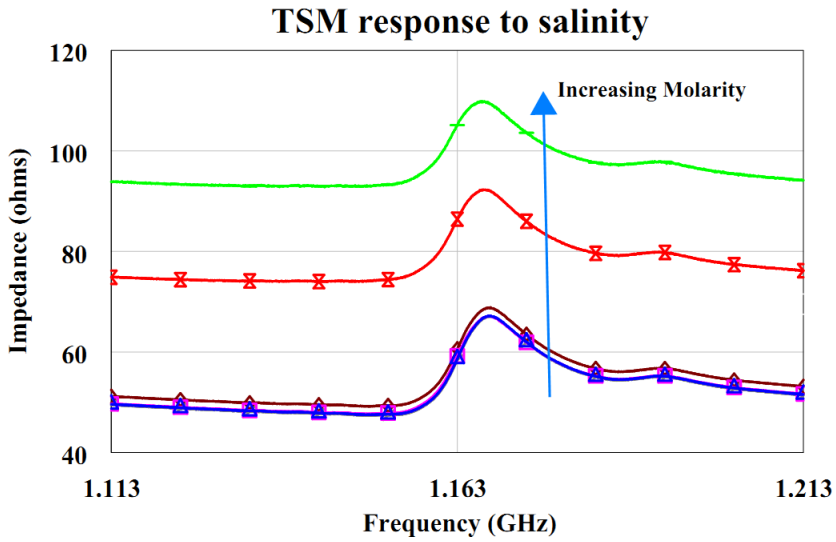

Figure 3.24: Impedance of the shear mode in multi-mode device under saline solution loading.

The device response therefore degrades due to the salt layer (which is conductive) being physically present on top of the device. This has been witnessed in the case of QCM [38]. Even though QCM is a low frequency device and different structurally it is still a TSM device and therefore the severe degradation of our devices can be attributed to the formation of the salt layer.

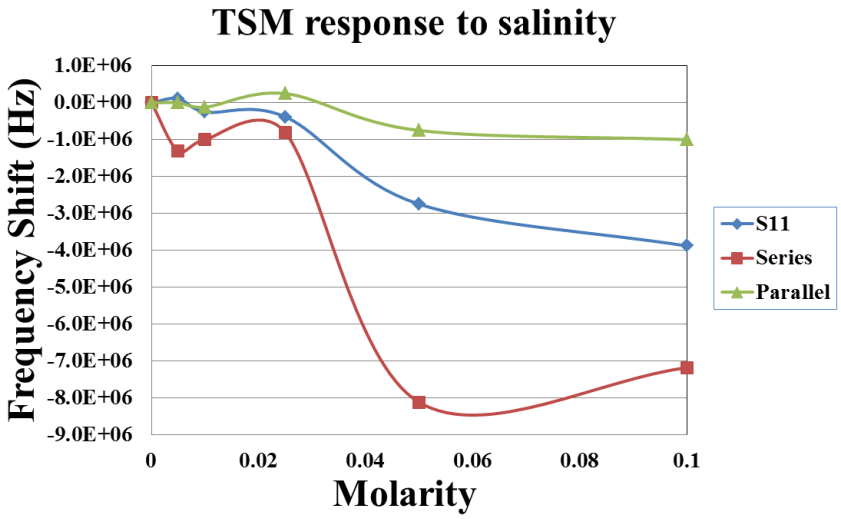

Figure 3.25: Frequency shifts of the TSM under solutions of varying conductivity

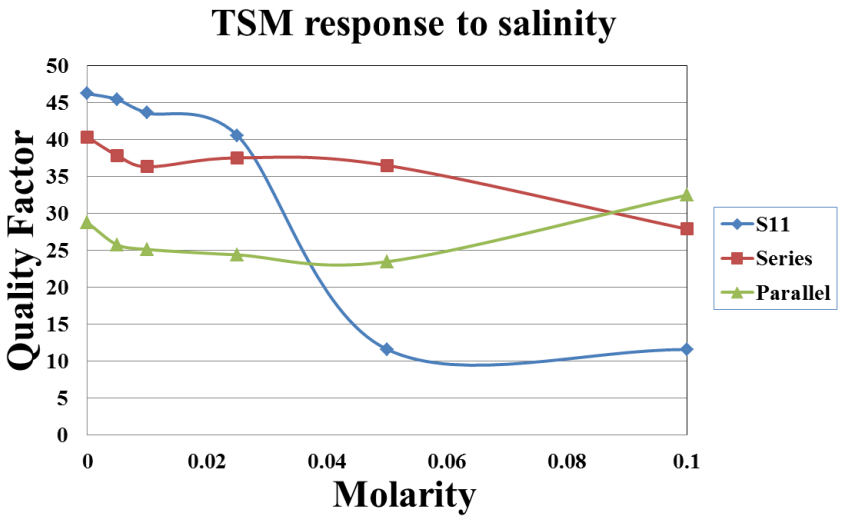

Figure 3.26: Quality factors of the TSM under solutions of varying conductivity

We have presented a preliminary characterization of our multi-media devices against viscous and conductive liquids. The measurements indicate the sensitivity of the device response to both viscosity and conductivity of liquid samples that points out the useability of the multi-mode device as liquid phase bio sensor. However, further experimental studies on a large number of devices for statistical significance is left for future studies. The conductive solution measurements need to be carried out in a way that avoids salt layer

formation either by operating at very low molar concentration or by introducing better methods of cleaning after each concentration measurement.

3.5 Conclusion

In this chapter we have tried to gain an understanding of the working of our multi-mode device. In the first section we used FEM simulation to look at the physical profile of the particle displacement of TSM in the multi-mode device structure. The results of FEM simulation suggest that laterally the energy of the TSM is trapped under the top electrode and vertically it extends into both the electrodes and the top layer of the reflector stack. Thus the material and the thickness of the electrodes as well as the top layer of reflector stack should be given importance in the design of TSM BAW SMR. From biosensing perspective, the area on the top electrode is more suitable for immobilization of chemi-sensitive layer as all the TSM energy is concentrated under the top electrode. In the second section we explored the nature of hybrid mode. We presented the hybrid mode is different from both the TEM and TSM and showed through theory, simulations and experiments that the hybrid mode is a coupled mode with both longitudinal and shear particle displacements. Lastly we presented the preliminary multi-mode device characterization with the viscosity and conductivity measurements. These measurements indicate the useability of the multi-mode device for liquid phase biosensing.

Equipped with the understanding of the multi-mode device developed in this chapter we can now move onto converting these devices into biosensors. The subsequent steps in this direction are the design of the microfluidics for liquid phase operation and the functionalization of these devices (with a chemically sensitive layer for target biomoelecule), which we discuss in the next chapter.

CHAPTER IV

MICROFLUIDICS DESIGN

4.1 Microfluidic integration for Liquid Phase Measurement

Microfluidics deals with the behavior, precise control and manipulation of fluids at microscale. Microfluidics integrated with biosensors enables the lab-on-a-chip type systems [39], and the point of care presence of biosensors [40]. The principal advantages of microfluidics is the capability of analyzing small sample volume, minimizing costly reagent consumption, multiple sample detection in parallel, high throughput analysis, portability and disposability [41]. To employ the BAW resonators described earlier as liquid phase biosensors, the use of integrated microfluidics is an essential step. For liquid-phase sensing application it is very important that only the active resonant area of the device is exposed to the liquid sample. Isolation of the liquid sample from the measurement probes is essential to avoid measurement errors and this isolation is the focus of the microfluidics design for our BAW resonators. Here, we present the investigation of a very simple design of microfluidics with our BAW resonator based biosensor. For this purpose we investigated the use of SU-8 polymer barriers for liquid containment.

SU-8 has been used to form microchannels in microfluidic systems [42], SU-8 is an epoxy-based negative photoresist and is commonly used for the fabrication of high aspect ratio for micro-electro-mechanical systems (MEMS) devices. Biocompatibility, mechanical reliability [43, 44], and chemical resistance to electrolytes are some of the desirable features of SU-8 [44]. The use of SU-8 allows for fabrication of monolithic auto-assembled channels for microfluidic applications [45]. The fabrication process is simple and low cost and is compatible to conventional fabrication techniques [45, 46]. Pan et al. [47] investigated many photo-patternable material and found SU-8 to be the best material for microfabrication of 3D structures.

We investigated the fabrication of SU-8 for microfluidics structures integrated with our

multi-mode devices. We designed a photolithography mask to pattern the SU-8 wells on the surface of our devices. We carried out our experiments for SU-8 fabrication on two different types of wafers containing different device designs. Firs wafer housed the planar devices which were the result of our initial attempts at designing TSM resonators. The second wafer contains the arrays of multi-mode devices. The difference between the two types of devices is that the firs one are planar devices whereas the multi-mode devices have raised ZnO platforms. Figure 4.1 shows the SU-8 wells on the wafer with the planar devices and the Figure 4.2 shows that these wells are able to contain the water providing isolation between the probe active area of the device.

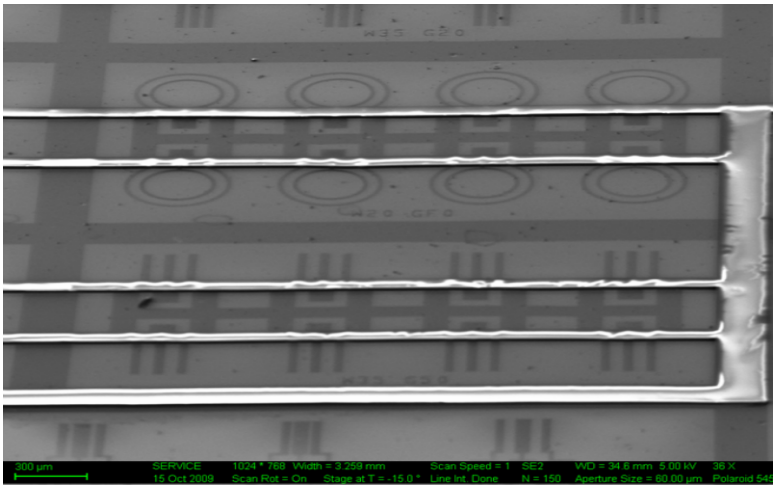

Figure 4.1: Fluid containment wells using SU-8 walls on the three finger device array.

Figure 4.1 shows SU-8 well on an array of our planar devices. For these wells to provide the necessary functionality of containing the liquids, the adhesion of SU-8 with the substrate needs to be very good. The SU-8 walls are passing over the aluminium electrodes and ZnO layer. Good adhesion to bothe of these materials is required to provide good containment of liquid. A zoomed in SEM of the SU-8 walls on the substrate (Figure 4.3) shows that the SU-8 walls show better adhesion to Aluminium as compared to ZnO. Figure 4.3 is an exaggerated case of poor adhesion to ZnO, where it seems to be completely disconnected from ZnO. In order to use SU-8 walls for microfluidic wells its adhesion to the surface of our devices needs to be improved.

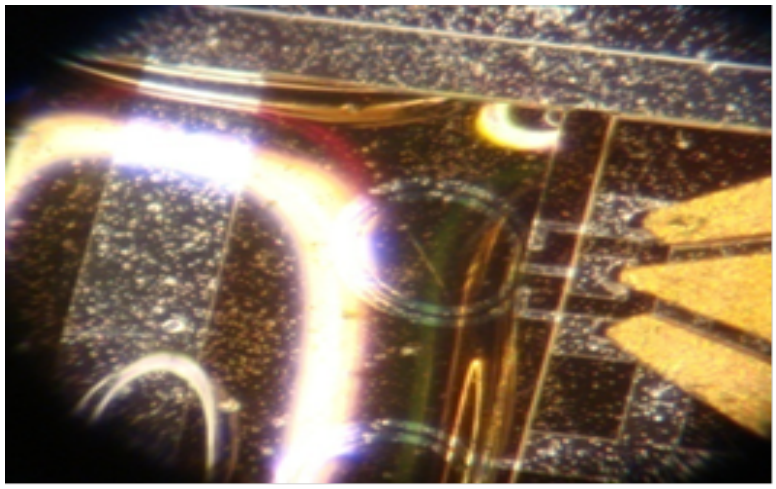

Figure 4.2: SU-8 walls isolating probe area and active area.

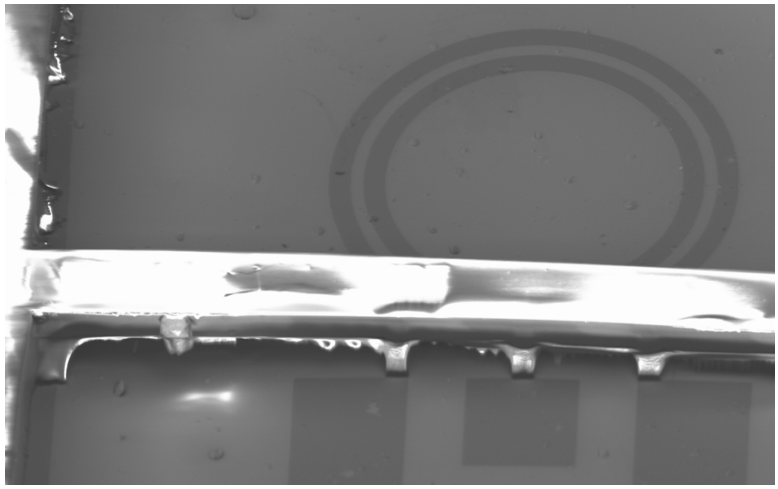

Figure 4.3: Su8 adhesion to ZnO and Aluminium.

We now take a look at the SU-8 walls fabricated on top of the wafer containing arrays of our multi-mode devices. Figure 4.4 shows the mask layout of the multi-mode device array with the SU-8 well shown with the yellow line. The sensor array in this figure consists of six dual mode resonators. The fluid well around the devices (green box) is about 2mm by 3mm. which ensures that each device is exposed to sufficient amount of liquid while isolating the probing pads. These wells will allow for the characterization of the devices when exposed to liquids of differing permittivities, viscosities, densities, conductivities, etc. The multi-mode devices are not planar devices as compared to the three finger devices shown above. The

central electrode along with the connecting probe pad are on top of a ZnO platform which is about $1\mu m$ thick while the other electrode is at the bottom of the ZnO. Thus the SU-8 have to ride up on the ZnO platform and to go across the top electrode i.e now the SU-8 has to conform to 1 μm of change in surface profile.

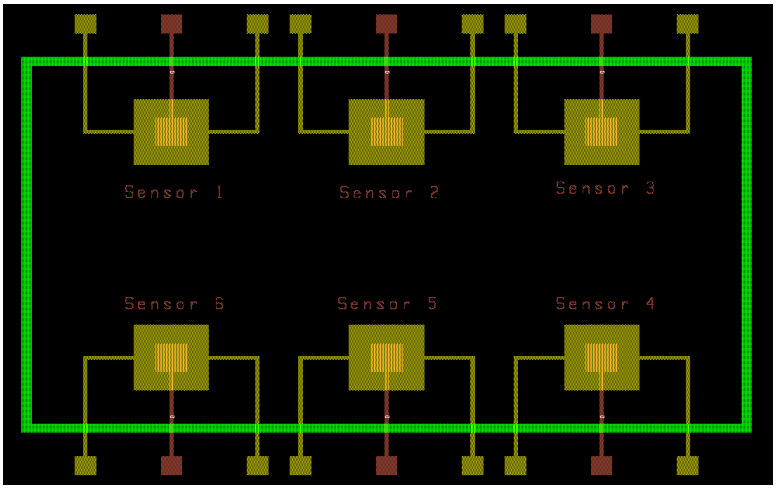

Figure 4.4: Su8 mask layout for the multi-mode device array.

Device failure due to SU-8 When we fabricated the SU-8 wells on the wafer containing multi-mode device arrays, we observed that most of the devices stopped working after SU-8 deposition. The S11 response of the device was a flat line without any characteristic resonance peaks implying a reflection coefficient of one. This suggested that the device has become open circuited. The SU-8 wall is passing over three conductors that connect the probe pads to the active area of the device. One of the possible causes of open circuit is that the SU-8 pulled on these three conductors and created an open circuit. To investigate this we looked at these conductors using SEM. Figure 4.5 shows a high resolution SEM image of the SU-8 passing over the central electrode. We see that the SU-8 film is pulling up the Aluminium electrode and may have broken it resulting in an open circuit condition. As we saw in Figure 4.3 that the SU-8 forms a bridge like structure where it is completely lifted off of ZnO. Such bridge structure would further be stressed because of 1um of raised ZnO platform. We believe that both the ZnO raised structure and poor adhesion of SU-8 to ZnO contribute towards stresses in SU-8 wall that result in the pulling of ZnO. A

possible solution to this problem would be to get rid of the raised ZnO platform, but that is an essential part of device design and can not be touched. Another solution would be to increase the adhesion of SU-8 walls to the substrate at all places including metal electrodes and ZnO. In [48] T. M. Verhaar conducted SU-8 adhesion tests on Silicon, Silicon Oxide and Alumniumn and concluded that SU-8 adhesion to Silicon Oxide is better than both Aluminium and Silicon. Hence, we proposed that a very thin layer of Silicon Oxide on the surface of multi-mode devices can be used in order to achieve uniform adhesion across the device structure. In addition the Silicon Oxide would also serve as a good passivation layer for ZnO. ZnO film is susceptible to easy dissolution on exposure to liquids that have even slightly acidic or basic pH level. Silicon Oxide passivation will increase the robustness of the devices and make it more accessible for different kind of surface chemistry options.

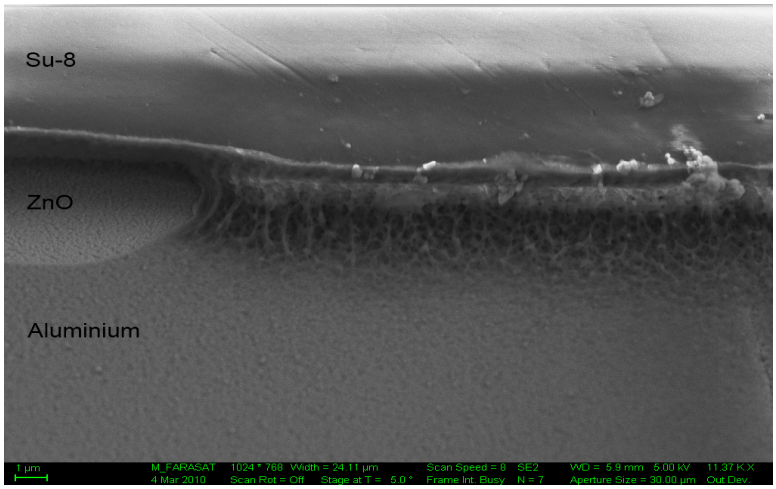

Figure 4.5: Su8 adhesion to substrate-Stress pattern in adhesion to Aluminium.

Figure 4.6 shows the SEM of a multi-mode device which has been passivated with 30nm layer of SiO. We see that SU-8 walls now conforms to the surface profile very well. The SU-8 walls sits evenly on both ZnO and the Aluminium electrodes and there is no sign of stress that is pulling at the Aluminium layer. Then we measured the device response after deposition of the SU-8 and it showed that the devices were still functional.

Slight degradation of the device response due to the SiO layer is expected as it will load the device mechanically. However there is some margin available to play with here. Firstly,

we tried 30nm thickness which is reasonably thick, however 20 nm or even 15 nm may be tried to minimize the loading effect. Secondly, taking into consideration that the energy of the acoustic modes generated in the multi-mode device is contained under the top electrode, a patterned Silicon Oxide layer that does not cover the top electrode may provide the same effect as a uniform SiO layer covering the whole multi-mode device.

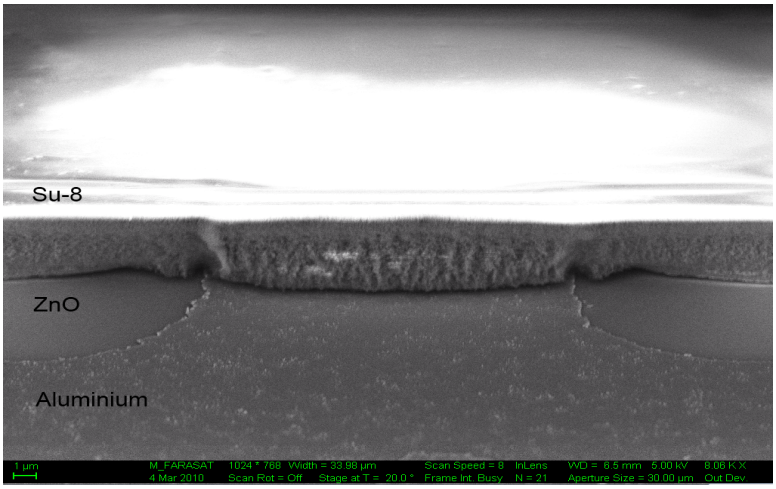

Figure 4.6: Su8 adhesion to substrate coated with 20nm Of SiO-Stress pattern in adhesion to Aluminium.

This concludes our discussion of development of a suitable microfluidic design that is compatible with our multi-mode devices. We have shown that the SU-8 microfluidic structures can be designed and integrated with ZnO based BAW resonators. In order to improve the adhesion of the SU-8 structures to the sensor surface a very thin layer of SiO can be used. Future research efforts can build upon the results presented in this section for design of advanced microfluidic structures such as channels, inlet and outlet reservoirs,and mixers using SU-8.

CHAPTER V

FROM TRANSDUCER TO BIOSENSOR

In this chapter, we look at the biosensor application of the transducers designed in early chapters. The first step in this regard is the functionalization of the transducer with a chemically sensitive layer. This layer imparts the sensing functionality to the transducer. We investigate various methods and propose a suitable method that is compatible with our ZnO BAW resonator devices. This is then followed by a preliminary investigation of our devices as biosensors for detection of Head and Neck Cancer biomarkers.

5.1 Sensor Functionalization

The purpose of the biosensor system is to determine the presence, absence or concentration of specific target molecules (biomarkers) in an environment. The biosensor system relies on the detection of a molecular recognition event e.g. an antigen binding to an antibody. A chemically sensitive layer (from here on referred to as bio-recognition layer) performs the molecular recognition. The layer itself is functionalized onto a transducer. Therefore a bio-recognition layer and the transducer are the two main components of a biosensor. A good functionalization layer design is a fundamental requirements for a working biosensor. In this section we will explore different types of surface chemistry options for immobilization that are compatible with our acoustic resonator devices.

5.1.1 Reversible and Oriented Immobilization

Antibodies or more generally proteins are one of the most commonly employed capture agents for biosensor applications. In the design of functionalization layer, proteins are immobilized onto the device and have been widely studied [49]. Immobilization can be defined as the attachment of target molecules to a support resulting in reduced or complete loss of mobility.

In principle, proteins can be fixed non covalently onto an inert metal surface by simple

adsorption. However, antibodies immobilized by physical adsorption are not stable during the biosensing process, especially if buffer rinses are carried out, because the physical adsorption is based on attraction forces, such as electrostatic force, rather than chemical bonds. Therefore, a covalent immobilization is desired to achieve better biomolecule activity, reduced nonspecific adsorption, and greater stability.

Another major issue regarding the protein immobilization is the orientation, which is considered to be a determinant of their effectiveness. Immobilized antibodies must be in an oriented and homogeneous manner, rather than randomly distributed on the surface. Proteins are inclined to lose their activity if their native structure is disrupted. Changes in temperature, pH, and ionic strength are such denaturing agents. It was suggested that random immobilization of proteins may cause changes in their native state, consequently reducing their activity to different degrees up to total loss [50, 51].

Exposed lysine residues present on the surface of proteins provide the possible attachment points. Since these residues are abundant on the proteins, they lead to random orientation and possibly multiple bonds between the proteins and the immobilization support. This lead to an overall reduced antigen binding capacity [52]. When the density of antibodies attached on the support is high, steric hindrance problems may arise.

Specifically for ZnO, Corso et al [53]has described in detail antibody immobilization on planar ZnO using amine and thiol terminated organosilanes based surface chemistry. But this method of antibody immobilization on ZnO results in random immobilization. Here we present our investigation of antibody immobilization using Histidine-Nickel interaction on our ZnO based BAW resonators. Histidine-Nickel interaction based immobilization method fall under the broad category of affinity-tag based immobilization methods. The tags allow a specific immobilization of the protein, confer orientation and reduce the probability of protein denaturation upon immobilization [54]. In addition the affinity tag based immobilization schemes offer reversibility of the immobilized molecule. Reversible immobilization can be beneficial as it can allow for regeneration of the device and can permit calibration of device before actual use [54].

A sequence of histidines at either the N- or C-terminus of a protein, introduced by gene

fusion method can form strong, stable and reversible complexes with metal ions such as Ni 2+. Usually the tag consists of 2 to 6 histidine residues attached to the protein. Most commonly a tag of 6 histidine residues is used, and is often labeled as 6xHis-tag. The interaction between the His-tagged protein and Nickle (Ni2+), shown in Figure 5.1, is also commonly used for protein purification [55]. The Ni(2+) ion is anchored to a surface through a chelator such as nitrilotriacetic acid (NTA). The protein thus bound can be removed by either introducing imidazole which competes with His-metal ion(Histag-Ni) interaction or by introducing ethylenediaminetetraacetic acid (EDTA) which competes with the metal-ion-chelator (Ni-NTA) interaction. These two methods has been used for regenerating the immobilized surfaces in various studies [54]

Our goal here is to functionalize resonator surface with Ni-NTA complex to allow for histidine tag (6xHis-tag) binding to surface.

The functionalization of gold substrates with Ni-NTA has been thoroughly investigated, and numerous successful studies employing this chemistry have been reported [56]. The functionalization of glass substrates with Ni-NTA is considerably less prominent, though still well-documented [54]. There has been no success (to our knowledge) with regards to the functionalization of ZnO substrates with Ni-NTA.

5.1.2 Ni-NTA based immobilization on gold electrodes

As a preliminary investigation we conducted experiments to establish the protocol for a functionalization layer that employs histidine-Ni(2+) interactions. We evaporated gold electrodes onto quartz wafer and followed the protocol in [57]to immobilize proteins onto the gold surface. The protocol consists of three steps. a) Formation of a self assembled monolayer(SAM)on gold surface using carboxylic acid terminated alkane thiols (C15-C00H Figure 5.2).

The sulfur in thiol (S-H) group has high affinity to gold surface.b) The other end of the alkane-thiol molecule contains carboxylic groups which has affinity for the amine group on the NTA-NH2. Thus in the second step this affinity is exploited for grafting NTA-NH2 molecule (Figure 5.3)onto the alkane thiol molecule resulting in a NTA-terminated SAM on

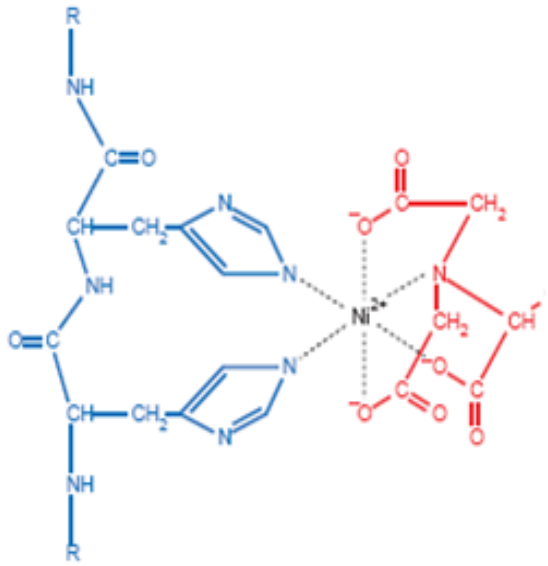

Figure 5.1: Histidine and Ni-NTA binding: part of 6xHis-tags is shown(blue) on the left of Ni(2+) and on the right of Ni(2+) NTA molecule is shown(red)
.

gold electrodes. c) In the third step the complexation of Ni(2+) ion onto NTA is carried out. Thus we have immobilized Ni(2+) ions onto gold surfaces. When a His-tagged protein is introduced to this surface containing Ni-NTA terminated SAM, the proteins will bind to the Ni(2+) due to the strong affinity between the Ni(2+) and His tags.

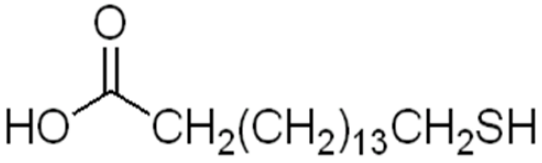

Figure 5.2: C15-COOH (16-mercaptohexadecanoic acid) with thiol(SH) group.

We used Enhanced Green Fluorescent protein (EGFP) tagged with 6 Histidine molecules to test our surface chemistry protocol using confocal microscope. EGFP exhibits bright green fluorescence when exposed to light in the blue to ultraviolet range. The results are shown in Figure 5.4. For reference purpose we took fluorescence image after SAM formation steps, and after formation of Ni-NTA on top of SAM. The final picture shows confocal images taken after exposure to EGFP. Each image was taken after making the

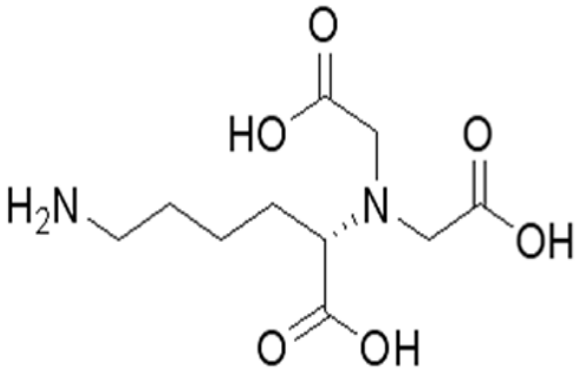

Figure 5.3: NTA-NH2 [(1S)-N-(5-amino-1carboxypentyl)iminodiacetic acid)].

reflectance off the metal electrodes to near zero, and using fluorescein filters that only allow imaging of the light with wavelengths in the vicinity of green light. These step helps to differentiate between reflectance off the surface of the substrate and the green fluorescence emitted by EGFP. It is evident from these pictures that there was no fluorescence visible after formation of Thiol-SAM and after immobilizing the Ni-NTA on top of SAM. However after exposure to EGFP we see green fluorescence only in the region of electrodes and not on the substrate.

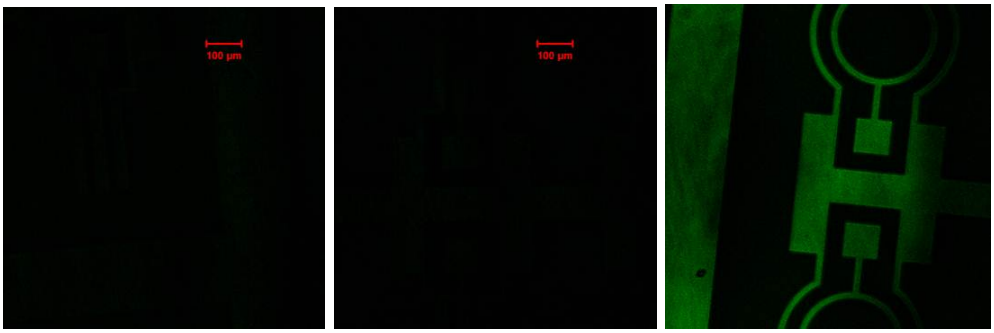

(a) Carboxylic Terminated Thiol only

(b) After immobilization of NTA and Ni(2+) complexation

(c) After exposure to EGFP

Figure 5.4: Confocal microscope images of NiNTA immobilization steps on Quartz wafer

These results show that the EGFP is bound to the electrode surfaces only with high degree of specificity indicating the success of the immobilization procedure. Taking this as a green signal we move onto towards our goal of using Histidine-Ni(2+) interaction for

immobilizing antibodies on ZnO devices.

ZnO Vulnerability: To carry out the above mentioned protocol on our ZnO based BAW resonator devices we deposited gold electrodes on ZnO and followed the protocol steps mentioned above. We found out that electrodes of our devices peeled off and closed examination revealed that the ZnO layer was being etched away. ZnO is known to be easily dissolvable material in acidic pH solutions. We measured and adjusted the pH of every solution towards basic end of pH scale and exposed ZnO surface to individual solution in protocol separately. We found out that all the solution were not reactive to ZnO except NTA-NH2 solution. NTA-NH2 solution always etched away ZnO even at basic pH of 8.3 which is very close to the pH of water. Thorough investigation of this behavior needs to be carried out by researchers skilled in the subject of Chemistry and is therefore beyond our expertise. However we can circumvent this problem by using a very thin layer of amorphous SiO_2 as a protective layer on top of ZnO. Thus we used 30nm of sputter deposited amorphous SiO_2 on top of ZnO. Etching tests, on this SiO_2 protected ZnO surface, with NTA-NH2 solutions revealed that the ZnO layer stays protected. Thus we can now use the above mentioned protocol on ZnO devices passivated by a thin layer of Silicon Oxide.

In some ZnO based devices it may be desirable to deposit on ZnO surface itself rather than on the electrodes. In those cases the thiol based SAM layer can not be used and a different foundation layer is required. Since we are using a SiO coating layer we now investigate the functionalization of Ni-NTA on Silicon Oxide.

5.1.3 Ni-NTA immobilization on Silicon Oxide surface

There are several chemistries and methods of application available to accomplish the goal of Ni-NTA immobilization on Silicon Oxide surface. One of the more common methods for functionalizing SiO2 surfaces involves the use of organosilanes. Organosilanes react at room temperature with surface hydroxides to link the silane molecules to the oxide

surface and thus laying a silane foundation layer. Most of the demonstrated methodologies employ organosilane molecules such as Mercaptopropyltrimethoxysilane (MTS), (3-glycidoxypropyl)trimethoxysilane (GPS) but the chemical principal is the same for all. Literature protocols also differ in the method of application of the surface chemistry. In some instances, the entire molecule (including Ni-NTA) was prepared in solution and then applied to the substrate in one step [58]. This approach is the most likely candidate for enhancing manufacturability of biosensors as it allows for the preparation of one large solution for an entire batch of devices and minimizes the necessary handling of the devices (substantially decreasing the potential for damage or contamination). Nevertheless, the chemical processes necessary for synthesis of large molecules in solution are fairly complex as is evident in the paper by Kim et al. [58].

We focus on the alternative application method that is, the largest purchasable molecules are applied serially so as to assemble the surface chemistry on the substrate. These processes tend to involve fewer chemicals and very simple techniques. First step is to lay the silane foundation. One end of the organosilane molecule binds with the hydroxyl groups on the Silicon Oxide surface and the other end has affinity for the lysine group(specifically for the amine(NH2) on the lysine) which is the attachment point of the antibody to the organosilane molecule. Thus NTA-NH2 which is also a lysine derivative binds to the immobilized silane exploiting this affinity. Therefore the second and third step are similar to the second step of immobilization on gold electrodes i.e to bind NTA-NH2 followed by Ni(2+) complexation with NTA-NH2. Previously in our group silane SAM formation has been thoroughly investigated by Corso et al. [53]. They immobilized MTS on ZnO followed by N-γ-maleimidobutyryloxy succinimide ester (GMBS) as Hetrobifunctional crosslinker. Heterobifunctional crosslinkers serve the purpose of transforming the end group of the silane into a group that will bind covalently with functional groups on an antibody. However this chemistry requires two step immobilization procedure first MTS is immobilized and then GMBS immobilization follows. This silane foundation has not been reported in literature for Ni-NTA immobilization. In literature, [58–60] have demonstrated the formation of NTA

terminated SAMS on glass surface(Silicon Oxide) using 3-glycidyloxypropyl) trimethoxysilane(GPS), a one step immobilization of silane foundation. Since prior literature evidence for formation of NTA-terminated Silane based SAM exists for GPS and not for MTS-GMBS we propose to use the former for our devices as well. Thus we devise a detailed protocol which is similar to the protocol described above for thiol surfaces. We propose the use of (3-glycidyloxypropyl) trimethoxysilane as the silane foundation layer. The detailed procedure of this proposed protocol for immobilization is given below and is graphically shown in Figure 5.5.

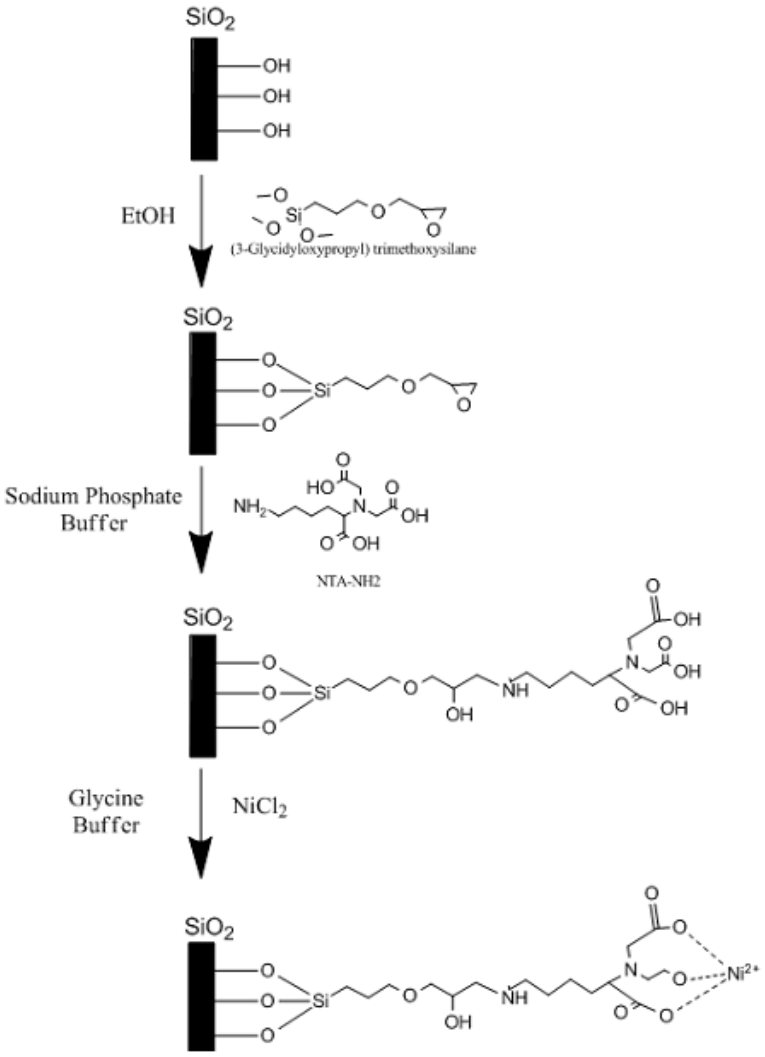

Figure 5.5: Procedure for immobilization of Ni-NTA on Silicon Oxide using Silane based surface chemistry.

Procedure

1. Wash die with the following: TCE, Acetone, Methanol, IPA, and HPLC-grade DI H2O.

2. Ion Mill substrate by manually moving the platform back and forth through the beams path for a total of 2 minutes.

3. Incubate the die in a 95% ethanol solution containing 2trimethoxysilane for 3 hrs at 60 C and rinse with HPLC-grade DI H2O.

4. Incubate the die in a 0.1 M sodium phosphate buffer (pH 8.0) containing 10 mM N, N-Bis(carboxymethyl)-L-lysine hydrate (AB-NTA) for 4 hrs at 60 C and rinse with HPLC-grade DI H2O.

5. Incubate the die in 5 mM glycine buffer (pH 8.0) containing 10 mM NiCl2 for 2 hrs at room temperature to charge the NTA groups with Ni ions and rinse with HPLC-grade DI H2O.

6. Store die in HPLC-grade water until use.

Protein immobilization

1. Incubate in 25 mM Tris-HCL buffer (pH 7.5) containing 100 nM His-EGRP or His-DsRed for 30 minutes.

2. Rinse with 10 mM Tris-HCl buffer (pH 8.0) and HPLC-grade DI H2O.

3. Dry under a nitrogen stream.

5.1.4 Conclusion of immobilization efforts

We have presented here our efforts to functionalize our ZnO BAW resonators with a reversible and oriented immobilization method. For this purpose we have demonstrated that successful immobilization of His-tagged proteins on gold electrodes based on Histidine-Ni(2+) interaction which used NTA as the chelator for anchoring on the Thiol based SAM layer. We then discovered that NTA-NH2 based protocols etch away the ZnO layer and

hence can not be used with ZnO based devices. Our experiments further showed that a thin layer of Silicon Oxide (30nm) prevent the etching of Zno and allows for the use of same immobilization protocol on quartz wafers and the Silicon Oxide coated ZnO devices. In some ZnO based device it will be desirable to functionaire on the area other than the electrodes, therefore, we have also suggested a protocol for immobilizing the His-tagged proteins on the Silicon Oxide planar surface using silane foundation.

5.2 Sensor Experiments for Head and Neck Cancer Biomarkers

We have now covered all parts of a complete biosensor . We described the design of the transducer and then the design of micro fluidics and finally looked into the methods of functionalizing the transducer for biosensing purposes. Equipped with all the knowledge gathered in this process we are now ready to test our biosensor to establish its sensing properties.

In this section, we engage in a preliminary investigation of the potential of these devices as biosensors for detection of Head and Neck cancer. We conducted experiments in collaboration with Dr. Dong Shin and Dr. Georgia Chen at the Winship Cancer Institutes at Emory University. They identified the phospho-Akt (pAkt) and the transforming growth factor alpha (TGF-α) as potential biomarkers for Head and Neck cancers. In this section we outline the protocols used and results obtained during the experiments.

5.2.1 Device Preparation

ZnO hybrid mode devices on 1cm x 1cm dies were used for the sensor experiments described here. Device operation and subsequent sensor testing was accomplished using a HP 8753 C Network Analyzer, equipped with a S-parameter test set and a Cascade Microtech 9000 Probe Station with a temperature control chuck. Devices were probed using Cascade Microtech ACP40 GSG-150 probes.

The devices were functionalized with three IgG Antibodies i.e Anti-FITC, anti-Phospho-Akt(pAkt) and anti-hTGF-α. Anti-FITC is used as a control experiment and is used as reference sensor. Anti-pAkt and anti-hTGF-α are known cancer Biomarkers. AnitFitc was obtained from Santa Cruz Biotechnology Inc. [anti-FITC (sc-69871)]. The anti-pAkt was

obtained from Cell signaling Technologies [#7143] and anti hTGF-α was obtained from R&D systems Minneapolis [anti-hTGF-α (AF-239-NA)].

These antibodies were covalently attached to the surface of the ZnO piezoelectric film using the functionalization protocol developed previously in our group [53] and is summarized as follows. The protocol employs mercaptopropyl-trimethoxy silane (MTS) as a primary crosslinker to the ZnO surface, followed by N-γ-maleimido butyryloxy-succinimide ester (GMBS) as a secondary crosslinker to covalently bind IgG molecules. T

Target Proteins The test medium consists of 686LN cell line lysate samples containing the target proteins pAkt and TGF-α proteins.The 686LN cell line lysate samples were provided by the labs of Dr. Shin and Dr. Chen. The stability of the acquired samples was time-sensitive and required immediate use within a time frame on the order of a couple of hours after preparation. The standard samples, along with the lysate samples, were prepared at Emory and transported by car to Georgia Tech for experimentation.

Four serial dilutions of the 686LN cell line cell lysate in a 1% ELISA blocking buffer (10ml PBS + 0.05% Tween 20 + 1% BSA) were used as the test medium. The lysate dilutions are as follows:

o Undiluted (100% lysate)

o 1:10 (10% lysate in buffer)

o 1:30 (3.33% lysate)

o 1:60 (1.66% lysate)

o 1:90 (1.11% lysate)

5.2.2 Measurement protocol

The following step-by-step protocol (after sample acquisition and device preparation, including surface chemistry) was used for the measurement of the acoustic sensors.

(1) 1cm x 1cm dies were split into three groups of 6-10 dies - control, TGF-α, and pAkt.

(2) A 30uL drop of the appropriate antibody was deposited onto the respective die and allowed to incubate for 4 hours in a petri dish under a parafilm cover to prevent evaporation.

(3) After antibody immobilization, the devices were rinsed with sterile PBS and individually placed into test tubes to await measurement.

(4) The die was rinsed with sterile PBS once more and dried under a stream of N2.

(5) Die was then measured using a coarse frequency resolution to gain insight on the approximate resonant frequency across the die.

(6) Once the approximate frequency was found, the probe station was calibrated over a 40MHz frequency span centered at the approximate frequency.

(7) "Before" measurements were taken of the devices with the antibody coating.

(8) A 20uL drop of the target (purified protein or lysate) was then deposited onto the die and allowed to incubate for 15 minutes.

(9) While this die was incubating, steps 1-7 were applied to the next die to reduce the risk associated with the time-critical nature of the samples.

(10) While second die is incubating, the first die was then rinsed under sterile PBS then dried under N2.

(11) "After" measurements were taken of the devices to monitor the frequency shift after target exposure.

(12) Repeat steps 1-11 with second die and subsequent dies.

5.2.3 Measured Dose Response curves

The change in resonance frequency measured by comparing the "Before" and "After" measurements is plotted against the 4 serial dilutions of the test medium to generate the dose response curves shown In Figures 5.7,5.8 and 5.9. Figure 5.6 shows an example device response "Before" and "After" exposure to target proteins.

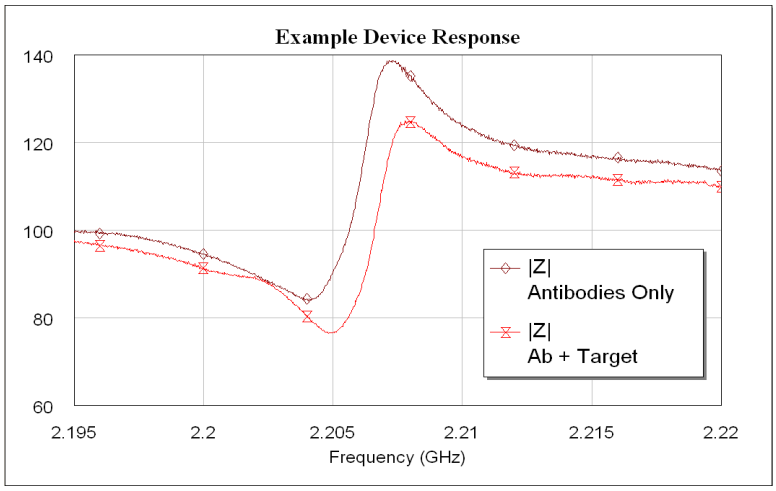

Figure 5.6: Example device response with Antibody and Antibody + Target

The dose response curve for pAkt shows a detection threshold at or below a lysate dilution of 1:40. There is a maximum difference of 1.2 MHz in frequency change between undiluted and 1:40, which is very easily detectable.

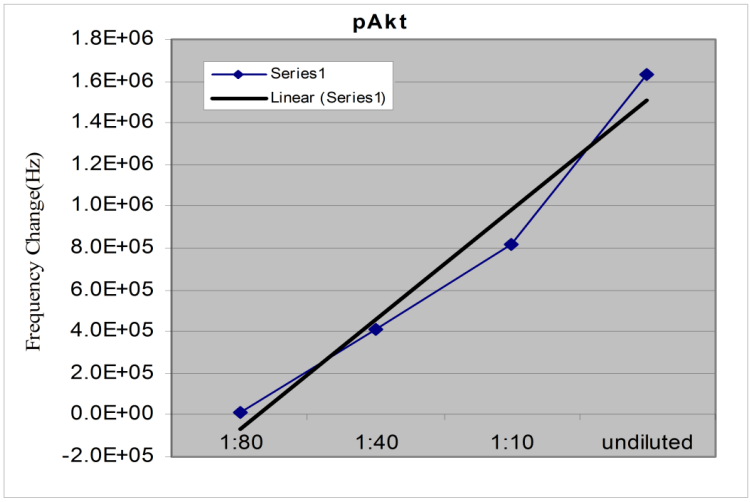

Figure 5.7: Dose response curves due to varying concentration of cell Lysate in buffer solution for a sensor surface immobilized to target pAkt in the cell Lysate.

The dose response curve for TGF-α shows a detection threshold at or below a lysate dilution of 1:80. There is a maximum difference of 800 kHz in overall frequency shift between undiluted and 1:80, which is also easily detectable.

The dose response curve for anti-FITC labeled device shows no real predictable pattern,

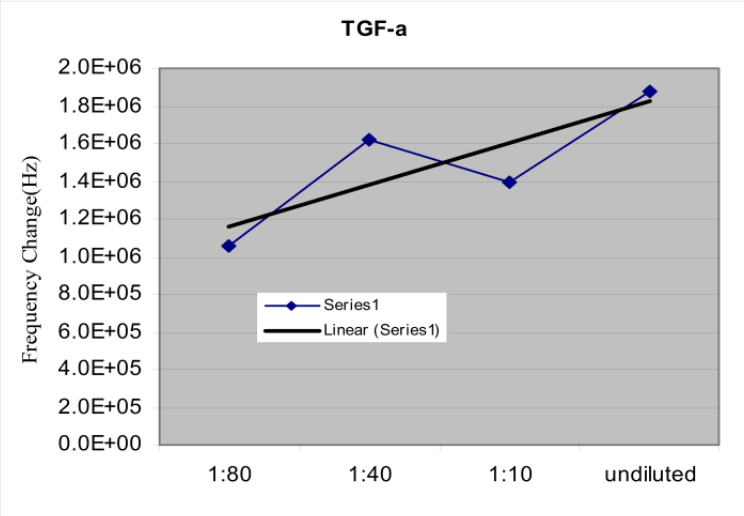

Figure 5.8: : Dose response curves due to varying concentration of cell Lysate in buffer solution for a sensor surface immobilized to target TGF- α in the cell Lysate.

i.e. it represents a kind of noise level. Only a 50 kHz difference in frequency shift between the undiluted and 1:80 lysate samples.

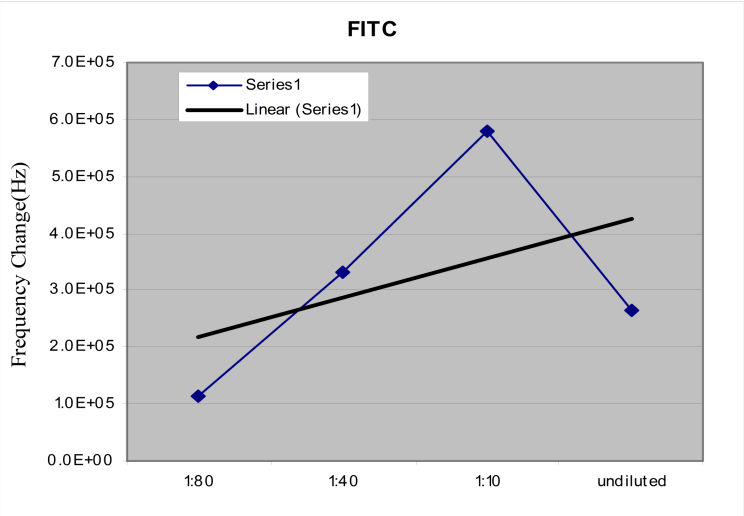

Figure 5.9: Dose response curves due to varying concentration of cell Lysate in buffer solution for a sensor surface immobilized to target FITC in the cell Lysate.

Discussion of the Dose Response curves The FITC dose response curve shows a relatively very small change as compared to the pAkt and TGF-alpha dose response curves.

Given that there are no target FITC molecules in the test medium, the sensor noise and possible non specific absorption may be the cause of these relatively small responses. The dose response curves for the pAkt and TGF-alpha show a linear increase in the change in the resonant frequency with increasing concentration of Cell lysate. The deviation from the linear fit in the TGF-alpha dose response curve can be possibly be explained by an inconsistency in the surface chemistry and Ab immobilization protocols on a particular die or insufficient rinsing of the die after Ab or target conjugation.

These sensor tests demonstrated the ability of the designed acoustic sensors to detect pAkt and TGF-α in extremely low concentrations . The pAkt detection threshold was at or below a 1:40 (lysate: buffer dilution). The TGF-α detection threshold was at or below a 1:80 dilution. Both of these threshold limits are much better than ELISA detection threshold. The ELISA experiments on pAkt and TGF-α were done in Dr. Georgia Chen's lab. They reported the detection threshold wer not quite 1:10 for TGF-α and approximately 1:10 for pAkt.

5.3 Conclusion

In this chapter we have covered the aspects of biosensor design which impart the sensing functionality to our acoustic transducer and then we present a preliminary effort at detection of cancer biomarkers using our biosensors. In the first section we explored various ways of immobilizing a chemically sensitive layer. We highlighted the importance of oriented immobilization and reversible scheme for preserving the activity of immobilized proteins and to allow for regeneration of the device surface. We presented Histidine-Ni interaction based surface chemistry as a suitable technique for oriented and reversible immobilization. We showed our efforts at using this functionalization approach on our ZnO based devices with Ni-NTA terminated alkane-thiol SAM and Ni-NTA terminated organosilane SAM. We also suggested the use of a thin layer of Silicon Oxide on top of ZnO as a protective layer to prevent the etching of ZnO during the immobilization procedure.

In the next section we presented a preliminary investigation of using our ZnO based BAW resonator devices as a biosensor for detection of Head and Neck Cancer biomarkers.

The results of these experiments demonstrated that our device are capable of detection of biomarkers in complex medium such as cell lysate and that they exhibit very high sensitivity and selectivity compared to ELISA based detection of the same biomarkers. However there is a need to test the suitability of these device for biosensor purposes in a much improved setup that involves a proper flow cell to allow for pressure and volume control, a method of probing these devices within a circuit that avoids the stresses induced by the RF probes. Future research efforts should focus on these steps as the feasibility of these devices, at a very high degree, as biosensor has been established in the research efforts presented in this dissertation.

CHAPTER VI

ELECTRICAL INTERFACE FOR WIDEBAND CHARACTERIZATION OF THE RESONATOR

6.1 Introduction

The electrical interface to the transducer/resonator plays a very important role in achieving the goals underlined for our Biosensor system in section (1.1.1). This interface allows for accessibility of the transducer response, determines its usability, manufacturability (to some extent), and its cost. Thus, a low cost, easy to use interface to the transducer can enable the ubiquitous presence of the biosensor. This chapter focuses on describing a new method for extracting data from resonator based sensing devices, which leads towards a low-cost, simple setup and compact electronic interface for sensor systems.

6.2 Motivation and Background

Many sensing platforms widely studied for use in chemical and biological applications are resonator-based. QCM is the most widely used resonator, however, there are other examples of resonators (used for sensing purposes) such as membrane resonators2, cantilever resonators,3-5 and high frequency surface and bulk acoustic wave (SAW and BAW) devices.6-8 The sensing functionality is imparted to the resonator by coating its surface with a chemically sensitive or selective layer (bio recognition layer). A change in the physico-chemical properties of this layer due to the sensing event affects the electrical response of the resonator. This permits the use of the resonator as a sensor device to detect changes in the physical properties of the contacting layer.

In general, a sensor system has to provide four principal functionalities: a) an effective electrical interface circuit to excite and read out the sensor response, b) the capability to analyze the sensor response in equivalent parameters of an electrical model of sensor, c) translation of the sensor data from electrical parameters to physical properties of the surface perturbation layer, and d) relationship of the physical terms to a chemical, biological, or

physical phenomenon. The interface circuit is the most important, since, any errors in measuring the sensor response will reflect adversely on subsequent modeling, translation, and physical phenomenon interpretation.

For designing the electrical interface circuit design, the resonator must be treated as a component included in the electrical circuit. This allows to analyze the resonator performance in relation to the external circuitry. Thus a proper electrical model of the resonator is required which represents it behavior electrically. Various electrical equivalent circuit models of the BAW resonators have been developed. The Butterworth-Van-Dyke (BVD) equivalent circuit, shown in Figure 6.1 adapted from [14], is a standard model used in the literature for bulk acoustic resonators.

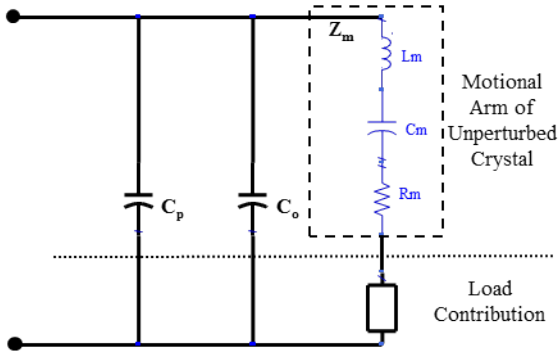

Figure 6.1: BVD model (adapted from 14).

The RLC "motional arm" of the network represents the acoustic motion of the resonator with the parallel capacitor representing the static capacitance of the device itself.

The lumped parameters in the BVD model can be determined by measuring the electrical response of the resonator using network analysis and then fitting the equivalent circuit model to this data. From this analysis further characterization parameters can be extracted such as f_s, the motional series resonant frequency (MSRF) of the unperturbed resonator given by (6.1), motional resistance R_s, the static capacitance Co, and parasitic parallel capacitance C_p.

$$f_s = \frac{1}{2\pi\sqrt{L_m C_m}} \tag{6.1}$$

where L_m represents the motional inductance and C_m represents the motional capacitance of the resonator. MSRF and R_s are generally used to extract physical parameters of the surface load.

Traditionally, oscillator circuits are used for monitoring the shift of the resonance frequency, fo, of the resonator. The resonator is employed in the feedback loop of the oscillator as a frequency determining element. These circuits provide only a single point measurement at the frequency where the oscillation criterion is met. However, the resonator response itself is broadband and contains much more information than a single point measurement. As an example, resonators operating in liquid phase experience a strongly damped Q as compared to gaseous phase. Extreme phase and circuit stability are required to obtain stable single frequency oscillation [37]. Hence, various modifications to simple oscillator circuits are reported which use automatic gain control [61, 62], or parallel capacitance compensation techniques [63]. It is very difficult to maintain the accuracy of the measurements under reduced Q conditions and, therefore, careful calibration of the oscillator circuit is required. This calibration in oscillator based circuits may require expensive instruments such as network analyzers [61]. Phase-Locked Loop (PLL) based techniques have been proposed [64–66] to overcome these issues but are relatively more complex and also require calibration. This calibration in PLL based circuits is achieved by employing additional reference phase-locked loops, thus resulting in manifold increase in circuit complexity. Another type of interface circuit relies on impulse excitation of the resonator. A popular example is the ring-down technique [67]. In addition to the resonance frequency, this method does provide an additional measurement point (energy dissipation, D, or quality factor, Q=1/D), but still relies on oscillator circuitry and suffers from the same problems previously mentioned.

Measurement of the shift in the resonance frequency and quality factor is not always enough for complete determination of the physical parameters of the tested sample. In particular, for biosensors operating in liquid loading conditions, there are more than two unknown physical parameters (such as mass density, shear modulus, film thickness) of the sample [68]. Therefore, a complete characterization of the impedance spectrum is useful, which can be only performed using network analyzers that are sophisticated, bulky and

expensive. Hence, they are not suitable for in situ techniques. Systems operating on the principle of network analysis, but with smaller and less expensive electronics, have been developed for quartz crystal resonators [69, 70]. Unlike network analyzers, they operate in a narrow range around the resonance frequency. As an alternative to impedance spectra, systems measuring a 'voltage transfer function', dependent on sensor-impedance, have been reported; however, the transfer function method requires further fitting to application-specific models to extract load data [71].

Simultaneous detection of multiple biomarkers requires multi-element sensor array systems. Such a system is very useful for screening of diseases like cancer or sepsis where single biomarker detection is not conclusive [1, 72]. Arrays of resonators have some unique electrical interface circuit requirements. In particular, for oscillator-based circuit designs, each amplifier-resonator pair must be designed separately to measure the shift in resonance frequency. However each individual oscillator loop in the array is prone to interference and frequency pulling effects from neighboring resonators in the array. Therefore it is difficult to extract and compare the orthogonal responses of individual resonators.

Excitation of a resonator with a sufficiently wideband signal gives an output that will contain only the filtered frequencies representative of the transfer function of the resonator. Previously, different types of wideband excitation signals have been used with resonators (i.e. multi-frequency chirp and narrow time domain impulse) [73, 74]. Each of these signals requires careful design of the signal itself as well as the circuit layout for the specific type, resonance frequency, and bandwidth of the resonator. These signals have their individual limitations for use with resonators: the chirped signal requires larger measurement time and the time domain pulse excitation signal is not well suited to very high Q resonators [74] such as a QCM (Q 30000). Moreover, the response of reduced Q resonators (as experienced under liquid loading conditions) spans a larger bandwidth. The time domain input pulse, then, must be very narrow in time and, correspondingly, its power is dispersed over a larger bandwidth. This will reduce the power at the resonance frequency down to a level which may fail to excite the resonance [74].

Another wideband signal is a multi-sine signal which is commonly used for frequency

domain system identification and characterization. Its application to resonant systems has not been reported. However the circuit design for multi-sine generation is very complicated, especially at high frequencies [75]. A multi-sine signal provides wideband excitation but its spectrum is discrete and will therefore be resolution limited and ill-suited for high Q resonators.

6.3 Spectral Analysis of Noise Excited Resonator (SANER)

Here we present a new method for extracting data from resonator-based sensing devices, which tries to circumvent the issues discussed above. The method is based on white noise excitation of the resonator. The resonator is used in a 2-port filter configuration and its output is then subjected to frequency domain spectral analysis. This proposed method is shown schematically in Figure 6.2. We further show that it offers a very simplistic interface design with several advantages over conventional methods of parameter extraction and tracking. The white noise source requires no design of the input signal and is readily available commercially for very wide bandwidths (1 MHz to 3 GHz). Moreover, it offers simplicity in circuit design as it does not require precise impedance matching; whereas such requirements are very strict for oscillator circuit systems, and are hard to fulfill. This results in a measurement system that does not require calibration, which is a significant advantage over oscillator circuits. The measurement output of this method is experimentally compared to that of a bench-top network analyzer and is shown to agree within 0.002%. Given the simplicity in the signal and circuit design, and its immunity to other common interface concerns (injection locking, oscillator interference and drift, etc.), this method is better suited to accommodating array-based systems.

Figure 6.2: Spectral Analysis of Noise Excited Resonator

6.4 Theoretical Underpinnings and Simulation Results

In deterministic signal scenarios, the input and output of a linear system are directly related through the transfer function. In the case of the excitation of linear systems with stochastic inputs, such direct characterization does not exist. The white noise input signal proposed here can be assumed wide-sense stationary. The second-order moments of such a signal (such as autocorrelation) can be used to characterize the system transfer function. The Fourier transform of the autocorrelation gives the Power Spectral Density (PSD), which is used for frequency domain characterization. For a random input signal, the input and output power density spectrums of the resonator are related as

$$\Gamma_{yy} = \Gamma_{xx}|H(F)|^2, \tag{6.2}$$

where, Γ_{yy} is the Output PSD, Γ_{xx} is the Input PSD, H(F) is the resonator transfer function in the frequency domain, $|H(F)|^2$ is thus the energy density spectrum of the resonator response. If the input is a white noise signal with power , then we have

$$\Gamma_{yy} = \sigma_x^2|H(F)|^2, \tag{6.3}$$

Thus, for white noise, the output PSD is proportional to the energy density spectrum of the resonator frequency response scaled by the power of input noise. The output, then, gives us a measure of the magnitude of the frequency response of the resonator. We cannot measure the phase of the resonator response with this method, which is very essential for oscillator based interface methods, The phase measurement, though, holds a much lesser significance here, because the frequency response measured by this method can give a direct measure of the resonance frequency, f_r, and the bandwidth of the resonator. The more technically precise term for bandwidth is half-band-half-width(HBHW) which refers to half the bandwidth at half maximum of the resonance. Conventionally these two parameters are used for characterizing the resonator, and are measured using network analyzers. It has been shown by various groups for acoustic as well as MEMS resonators that the viscoelastic properties of the surface perturbation sample can be deduced by analyzing the resonance

frequency and bandwidth [71, 76–80]. Resonance frequency and dissipation, (measured by oscillator based interface circuits coupled with impulse excitation), have also been extensively used to interpret the viscoelastic properties of the surface coating layer and the tested sample [81,82]. Both of these methods are equivalent as Johannssmann has given a relation that describes dissipation, D, in terms of the HBHW bandwidth [83]. Furthermore, convergence relationships of dissipation analysis and the analysis based on Δf and ΔHBHW, have also been reported [84]. The proposed method described here gives not only information about f_r and Γ, but also the wide-bandwidth transfer function of the resonator (with a much simpler setup than a network analyzer). Potentially, this could offer more useful information than just relying on the f_r and Γ. The setup of Figure 6.2 was simulated using Simulink software by MathWorks. The simulation setup is shown in Figure 6.3.

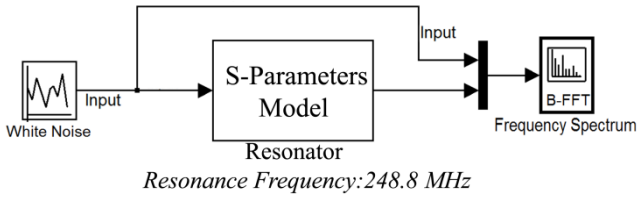

Figure 6.3: Setup for simulating noise excited response of a resonator.

The "White Noise" block generates a signal with uniform frequency distribution as an input to the resonator. To model the resonator response accurately in the simulation, a measured S-parameters file of an actual SAW resonator is used. The FFT scope is used for power spectrum density analysis. The results are shown in Figure 6.4. Notice that in this simulation setup, we used a 2-port resonator and the output frequency response is similar to the S21 response. However, one-port devices can also be used in this technique by employing them as a through element in a 2-port measurement system. The results in Figure 6.4 are for an FFT of 1024 points. We did the simulation for an FFT size of 256, 512, 1024 and 2048. The relative error between the S21 and FFT output decreased with increasing FFT size. However there was minimal improvement between 1024 and 2048 point FFT. We expect that the FFT size required for a minimal relative error is dependent on the resonator quality factor and the particular sensing application. The purpose of presenting this simulation is

to give a proof-of-concept for the proposed method, which is clearly demonstrated by the results shown in Figure 6.4. Next, we demonstrate the scalability of the proposed method to resonator arrays.

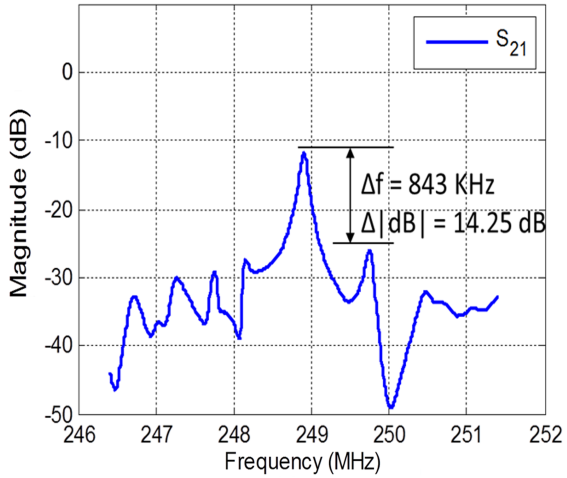

(a) Measured S-parameters of a SAW resonator.

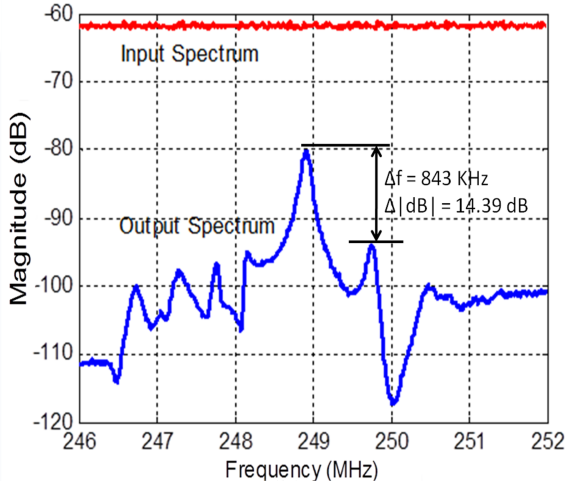

(b) Simulated FFT scope output showing both the input noise spectrum and the output of the resonator.

Figure 6.4: Saw resonator Simulation.

Figure 6.5 shows the setup for exciting a 2-element resonator array simultaneously with a single noise source. The resonators are again modeled using their S-parameters files with their individual resonance peaks (in the S21 response) at 248.8 MHz and 252 MHz. The simulated FFT of the combined output shows that the individual responses of each resonator element are reproduced fairly accurately in the spectral output. Based on these simulation

results, we suggest that the proposed method can be easily extended to resonator arrays. This method provides a significant advantage over all other methods for array systems by eliminating the need for multiple input sources or a switching method between array elements. However, it requires that the resonance frequency of each element in the resonator array is offset from the other elements in the array. Implementing such an array system has been reported by Yang, et al [73].

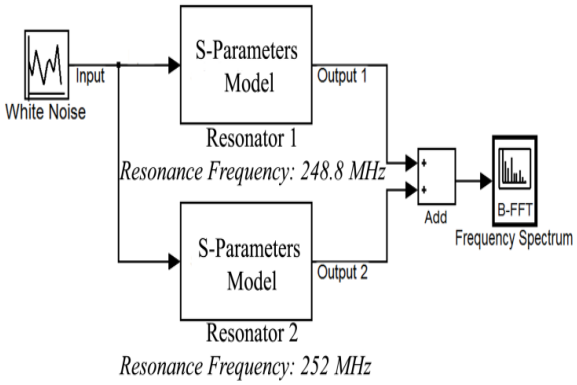

(a) Simulation setup for 2 element resonator array.

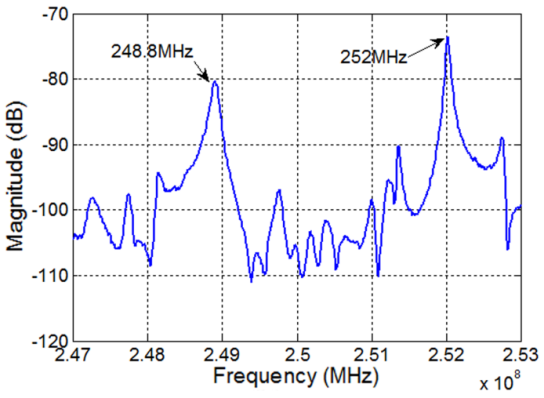

(b) The noise excited spectral output of a 2-element resonator array.

Figure 6.5: Array system simulation.

6.5 Measurement Results

To further investigate the proposed system, we built a prototype using a surface mount noise source, SMN-7114-C2A by Micronetics Inc. This noise source excites a resonator and the output spectrum is measured using a E4404B Agilent Spectrum Analyzer (SPA). The noise source and its frequency spectrum are shown in Figure 6.6. The prototype setup is

shown in Figure 6(b). Using this setup, we measured two different types of resonators-a 434 MHz SAW resonator and a 5 MHz QCM.

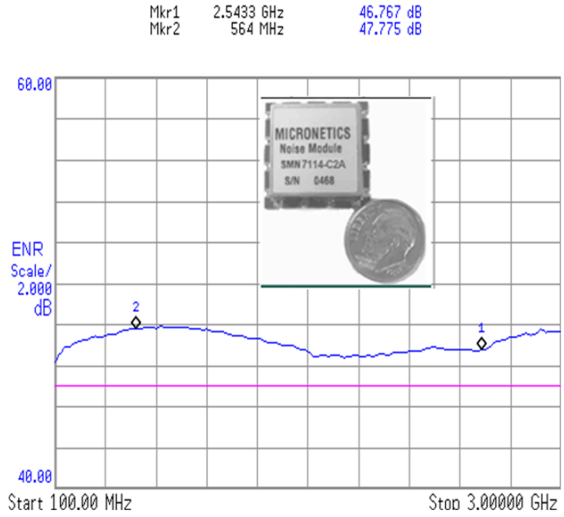

(a) SMN-7114-C2A noise source and its spectrum.

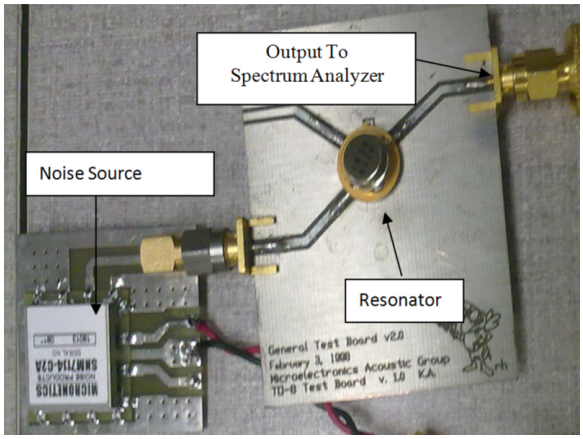

(b) Prototype setup snapshot.

Figure 6.6: Prototype System

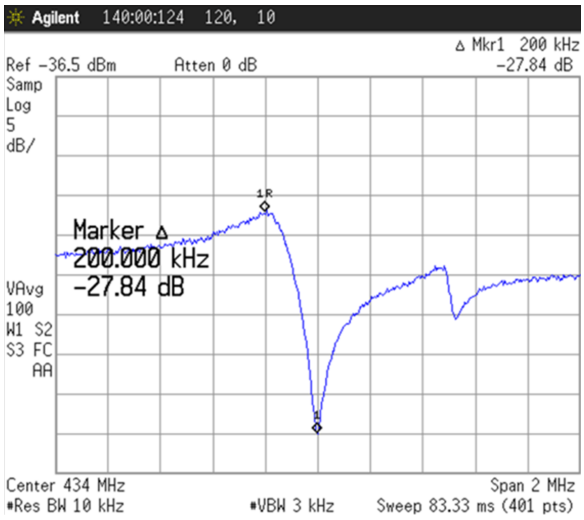

(a)) Measured by a spectrum analyzer.

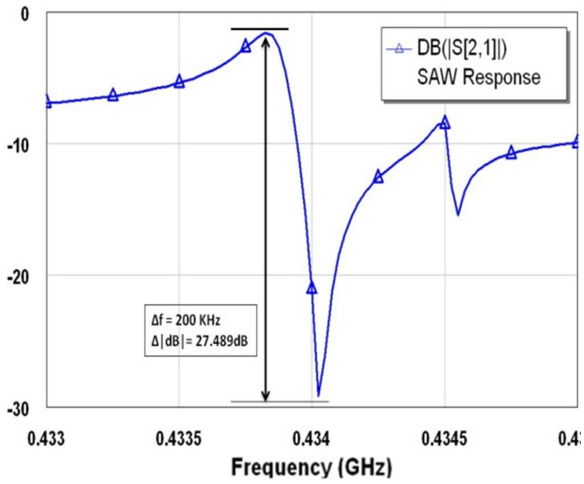

(b) Measured by a vector network analyzer.

Figure 6.7: Measured spectral output of noise excited SAW resonator.

6.5.1 SAW Resonator

We measured a 434 MHz SAW resonator with the prototype setup shown in Figure 6(b). A comparison of the SAW resonator output as measured by the SPA and as measured by the Vector Network Analyzer (VNA) is shown in Figure 6.7. It is evident that both responses are comparable in frequency content. The characteristic resonance peaks are replicated at the same frequencies, and the relative strengths of frequency content are preserved and have been explicitly marked. It should be noted that the measurements with the proposed method are done without any calibration. The remarkable accuracy of the proposed system is further highlighted in Figure 6.8, where both responses are plotted in the same graph. There is no scaling employed on frequency or magnitude axis, but both responses are plotted after subtracting the respective mean power levels. The frequency resolution for VNA measurements and for SPA measurements is 3 KHz and 10 KHz respectively. The resonance frequencies (taken as the frequency at the minimum point in the S21 amplitude) measured by VNA and SPA are 433.996875 MHz and 434.000000 MHz, respectively. This gives a relative difference of about 0.0004%. The mean amplitude difference over the entire bandwidth of measurement, between the two methods is 0.3 dB with a variance of 0.09 dB. Further accuracy can also be obtained by improving the frequency resolution of the SPA, but at the cost of increased measurement time.

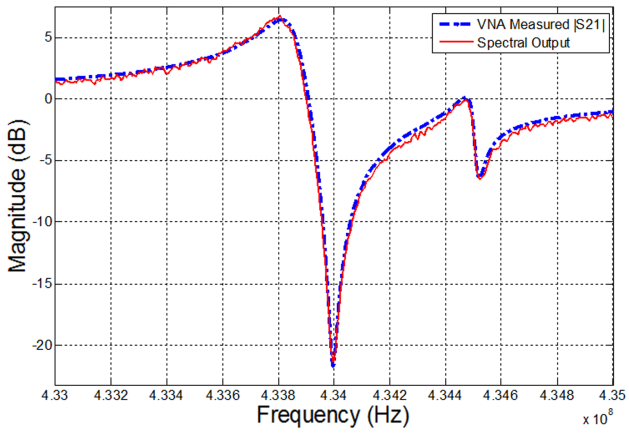

Figure 6.8: Measured responses of SAW resonator by VNA and the proposed method after mean level subtraction.

6.5.2 Quartz Crystal Microbalance

The same circuit setup shown in Figure 6(b) without any modification can be used for measuring low frequency or high frequency resonators, as well as one-port resonators. However, one port resonators will be needed to plug into the two port circuit setup as through elements. To demonstrate these properties of the proposed system, we measured a 5 MHz QCM (a very low frequency, one-port resonator) with the same circuit that was used for the SAW resonator mentioned above. We measured the 2-port S-parameters of the QCM with the VNA as well as with our proposed method. Figure 6.9 shows the two responses in a single plot with the mean power level for each response subtracted from its respective response.

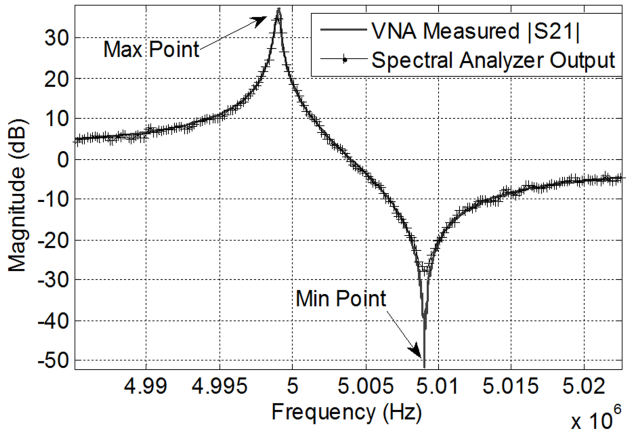

Figure 6.9: Measured Responses of QCM by the VNA and the proposed method after mean level subtraction.

Here, we present a comparison of QCM measurement with the two methods. There are two distinct points in the QCM response which corresponds to the maximum amplitude point (Max Point) and minimum amplitude point (Min Point. Each of these could be considered a measure of resonance frequency. At the maximum, the resonance frequencies measured by the VNA and SPA are 4.9991 MHz and 4.9990 MHz, respectively. This gives a relative difference in resonance frequencies of about 0.002%. The mean amplitude difference between the two methods (over the entire bandwidth of measurement) is 0.58 dB with a variance of 1.4 dB. However, these numbers are misleading because the SPA response is not

following the VNA-measured results in the negative dip at minimum. This error is due to the fact that the QCM response has a very large dynamic range (80-90 dB), which takes the negative dip well below the noise floor of the SPA. Therefore, the QCM response is truncated at the negative dip as it has approached the noise floor of the SPA (-124 dBm). This problem can be taken care of by properly amplifying the input noise signal level to raise the output of the resonator well above the SPA noise floor.

6.5.3 Frequency Tracking Ability

We measured the temperature curve of the SAW device with both a VNA and the proposed method. The temperature was varied from 0 C to 100 C and at each temperature point the devices were allowed to settle for 2 minutes. The changes in device response with changing temperature were tracked by measuring the maximum amplitude point in the frequency response obtained by the spectral analyzer and in the —S21— response measured by the VNA. An important detail to note here is that VNA measurements were taken after a tedious 2-port calibration of the VNA, whereas the measurements with our proposed method were taken without any calibration. Results are shown in Figure 6.10. The temperature curves measured by both techniques are in agreement with a maximum difference of 5.53 ppm. This experiment demonstrates the ability of the proposed method to accurately track changes in the frequency response of the resonator.

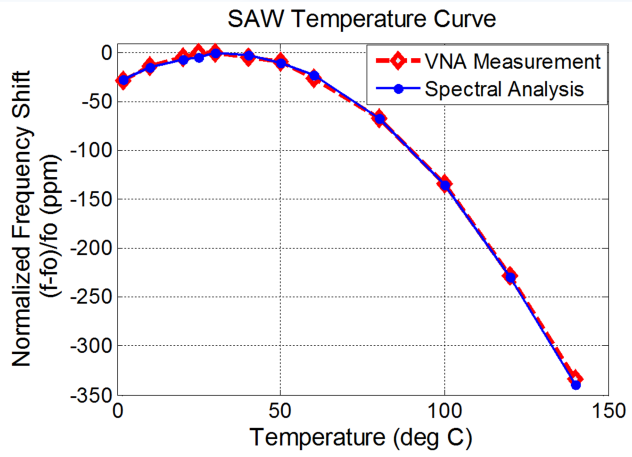

Figure 6.10: Temperature curve measurement of SAW device with VNA and with noise-excited spectral measurement.

6.6 Discussion

The SANER system proposed above gives a wideband response of the resonator with a very simple setup. The wideband frequency response has more information than just the measurement of resonance frequency and bandwidths. This extra information could be potentially useful for extraction of the physical parameters of the surface load. It is extremely difficult to find and track the resonance frequency shifts of the resonator when heavily loaded by liquid. The oscillations may even fail to occur due to high damping. Therefore under heavy liquid loading conditions the proposed method has an advantage over other methods as it is not just a single point measurement. Moreover, because of noise being used as the input signal, significant advantages are obtained over conventional single frequency excitation systems such as oscillators. Circuit design for the proposed method is relatively independent of resonance frequency variations. Hence, the same circuit designed for a particular center frequency may be used for a very large bandwidth around the center frequency. We demonstrated the use of same circuit for 5 MHz and 434 MHz device without using any calibration for either device. The proposed method is relatively immune to parasitic effects compared to oscillator-based systems. It is also immune to background noise fluctuations which appear as a jitter in the oscillator-based systems and result in limited frequency resolution. Wideband white noise has a continuous frequency spectrum and hence, the resolution is, theoretically, not limited. In practice, though, the resolution will be limited by the ADC sampling rate and FFT resolution. There are some additional benefits for noise excitation of resonator arrays. It does not require individual circuits tuned for individual sensors. A single input source drives all the sensors simultaneously with no switches required (switching circuits introduce an additional complexity at high frequencies). In our proposed method, each resonator outputs its own frequency response and is not in an oscillator configuration where loop dynamics can lock onto external signal (from a neighboring resonator) injected into the loop [85]. Therefore, it will be immune to interference from neighboring resonators.

Table 6.1: Summarized comparison of Oscillator-based systems and the proposed method

	Oscillator-based Interface Circuitry for Resonators	**Spectral Analysis of Noise Excited Resonators**
Measured Information Content	Gives a single point measurement of the resonance frequency only.	Gives a wideband frequency response, holding much more information than just the resonance frequency.
Circuit Design	• Strict requirements of phase stability. • Requires precise impedance matching. • Circuit design requires modification with the change in resonance frequency. • Phase noise appears as jitter and limits the frequency resolution.	• No phase compensation requirements. • Tolerant to mismatch over a broadband. • Same circuit can operate over a wide range of resonance frequencies. • Immune to phase noise and limited in frequency resolution only by FFT size.
Reduced Q Conditions	• Difficult to excite oscillations. • Requires complex circuit modifications for accurate measurements.	• No Oscillatory behavior needed. • Same setup can be used for both reduced Q and high Q conditions.
Array Systems	• Requires individual circuit tuned for individual elements of the array. • Each element is prone to interference (due to injection locking) from neighboring resonators in the array.	• Array is excited as a whole and hence does not require individual circuit for each element. • No oscillator loops are involved and hence interference from neighboring elements is not a concern.

6.7 Conclusion

In this chapter, we have presented a novel method (SANER) to measure and track a resonator's response and extract its characterization parameters. This method measures the wideband frequency response of the resonator with a much simpler setup compared to conventional methods. We have suggested and demonstrated the use of a white noise signal as a viable signal for broadband excitation of resonator-based sensing platforms. We have also established, through simulation and prototype measurements, the feasibility of the proposed method. The accuracy and speed of the system can be further improved by FFT-based digital implementation of the spectral analysis system. This will allow for a low-cost and compact solution in the form of a system on a chip. In the subsequent chapters, we will expand further on the digital implementation techniques and the design of a standalone system based on the proposed method.

CHAPTER VII

STAND ALONE SYSTEM DESIGN AND IMPLEMENTATION

7.1 Introduction

The SANER interface system proposed and demonstrated in the prototype form in the previous chapter have to be implemented in a stand-alone way in order to deliver its promised benefits of portability and low cost. In this chapter we will discuss the system architecture and implementation details for stand-alone implementation of system described in chapter 6. The perspective here is to enable the reader to be able to understand the theoretical basis and construct and demonstrate the performance of a system for acoustic biosensing application.

7.2 System Architecture

7.2.1 Background

The principal component of design for standalone SANER implementation is the spectrum analyzer. Modern spectral analyzers come in a variety of forms with different characteristics. Broadly they can be classified as swept frequency analyzers and FFT analyzers. Swept frequency analyzers are primarily aimed at measurement of RF and microwave systems using analog techniques.

7.2.1.1 Swept Frequency Spectrum Analyzer

A typical architecture of a swept frequency analyzer is shown in Figure 7.1. The swept spectrum analyzer uses a super-heterodyne configuration. A swept local oscillator (LO) sweeps through a range of frequencies that are mixed with the incoming signal. The output of the mixer has sum or differences of the original signals. This output passes through an intermediate frequency (IF) filter. The IF filter selects the desired component to be processed further. The IF filter output drives the detector which produces a voltage level relative to the amount of power received from the incoming signal. As the LO sweeps different

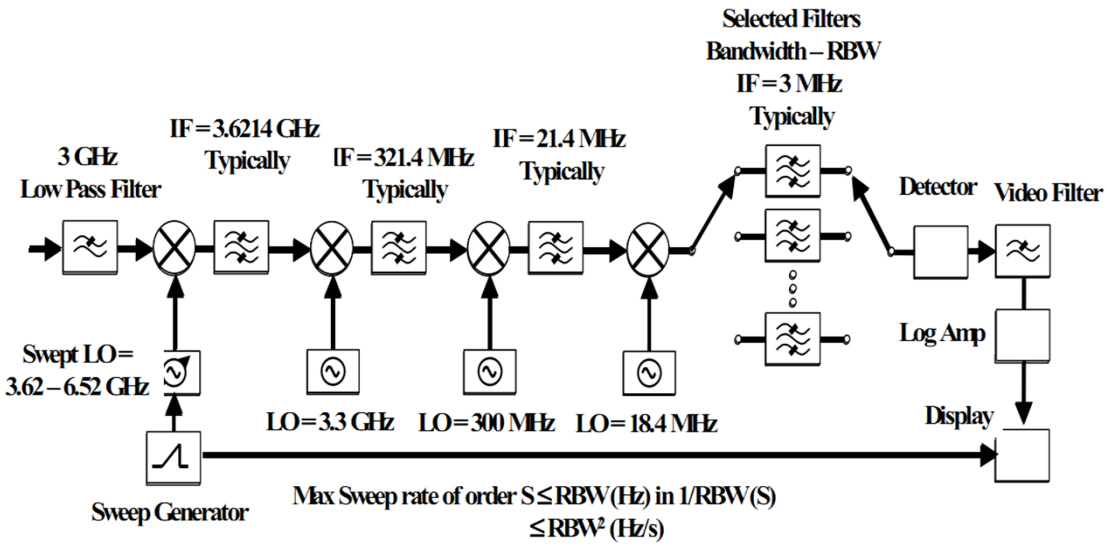

Figure 7.1: Conventional Swept Frequency Analyzer [2]

frequencies, the detector produces a corresponding voltage level, or power measurement. Thus we get a power level vs frequency plot i.e the frequency spectrum.

An important parameter of the swept analyzer is Resolution bandwidth (RBW). It is determined by the bandpass IF filter. Adjusting the bandwidth of this filter allows for the discrimination of signals with closely spaced frequency components, while also changing the measured noise floor. Decreasing the bandwidth of RBW filter decreases the measured noise floor and vice-versa. Often the IF filter section is composed of a number of filters, which together determine the resolution bandwidth. Resolution bandwidth is affected by the speed at which the instrument sweeps the frequency range. The IF filter requires a certain time to respond to signals placed at the input, so the analyzer cannot sweep through the frequency range too fast.

Thus the two important components of conventional swept spectrum analyzers are the swept local oscillator and the filter bank. For narrower RBW the filter design becomes very difficult in the analog domain. Therefore, for very low RBW (less than 300 Hz) digital filters are used. The swept LO design also becomes very challenging for very low RBW. The narrower the RBW, the more accurate the frequency sweep and the lower the oscillator phase noise is required. Here again digitally synthesized source is used for LO. Thus for

narrow RBW, the use of digital filters and digitally synthesized source results in a very expensive analyzer. Both the cost and the analog components are not compatible with a system on a chip type implementation. Thus the the swept spectrum analyzer is not ideal for our stand alone system design. Therefore, we will be focussing on the other type of analyzer, the FFT analyzer.

7.2.1.2 FFT Spectrum Analyzer

FFT analyzers acquire a digital time domain waveform using ADC, and the down conversion and filtering is done in the digital domain. The transformation from time to frequency is done using FFT algorithm. The speed and dynamic range of FFT analyzers is mainly limited by the availability of appropriate ADC. Conventional swept spectrum analyzers easily give a dynamic range of 100 dB. Recent advances have produced ADC of 16 bits at 100 MHz sampling rate, thus giving more than 100 dB of dynamic range. A simplified block diagram of FFT based analyzers is shown below. Prior to analog conversion the

Figure 7.2: Simplified block diagram of FFT Analyzer

signal must pass through attenuators or gain stages to adjust the amplitude of the signal to match the input range of the ADC. After the ADC, there is a digital IF and filtering block that enables high resolution spectrum for smaller bandwidths. Modern FFT analyzer has dedicated DSP circuitry available to perform the FFT and there is a multitude of DSP algorithms for implementation of FFT based spectrum analysis. Thus there are many different configurations of an FFT analyzer depending on the particular algorithm and application. Moreover, the DSP circuitry is programmable, allowing for a change in the algorithm according to desired specifications of spectrum. A detailed description of all the available configurations and algorithms is beyond the scope of this dissertation. In the

following lines we will describe the design of FFT analyzer for our particular application and will explain the algorithms and techniques pertinent to the requirements of our design.

7.2.2 Goals of Digital System Design

Our intention here is to design a spectrum analyzer that takes the method proposed in the previous chapter and move it towards a standalone type implementation. The overarching goal is to design FFT analyzer to measure spectral output of a noise excited resonator or resonator array. To achieve this the system must provide the following features.

- Provides enough dynamic range to cover the amplitude variations in the resonator response.
- The system should be very sensitive to allow for measurement of damped frequency response of the resonator under heavy liquid loading conditions.
- The system should be able to measure resonator with very high resolution thus enabling measurement and tracking of all features in the resonator response.
- The bandwidth of the system should be able to encompass the complete frequency spanned by the resonator (or the array of resonators) response.
- The system should be able to accommodate an array of resonators and still maintain the high resolution for individual resonator response.
- Ideally the system should be scalable to accommodate different types of resonators operating at different resonance frequencies.

Though we suggest implementing the spectral analysis of resonator output in the digital domain, the resonator itself would still operate in the analog domain (it is excited with an analog input noise signal and generates an analog output signal). The output signal of the resonator has to be converted into the digital domain by an appropriate Analog to Digital Converter (ADC) for further signal processing. The input signal (Wideband white noise) can be generated by an analog noise source or it can also be generated in the digital domain. The digitally generated noise signal however needs to be converted to analog domain by

using Digital to Analog Converter (DAC). The noise signal thus obtained may also require some signal conditioning such as adjustment of its gain and center frequency before being fed into the resonator. The digital generation reduces the external components required for the stand-alone design and gives more control on the properties of the generated noise, which can be exploited in the analysis of resonator output.

We will slightly modify the block diagram of FFT analyzer shown in Figure 7.2 to suit our system and arrive at the system architecture shown below.The detailed requirements and design of these components is discussed in the following lines.

The complete system is a mixed signal system where part of the system is in the analog domain.

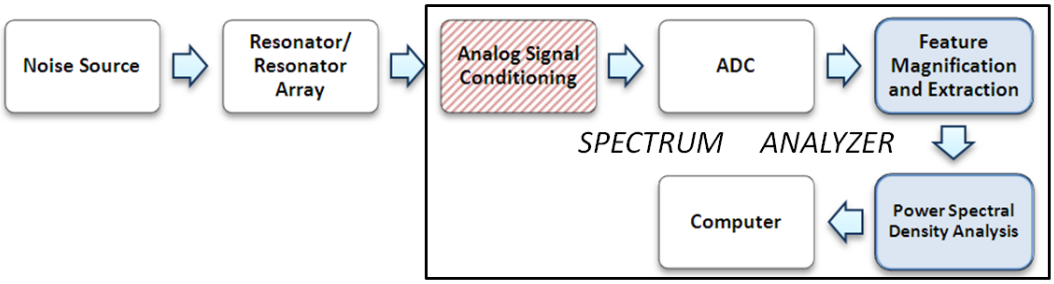

Figure 7.3: System Architecture for Stand Alone System Design

We will briefly explain the Analog Signal Conditioning and the Feature Magnification and Extraction blocks now. The subcomponents of analog signal conditioning chain are shown below.

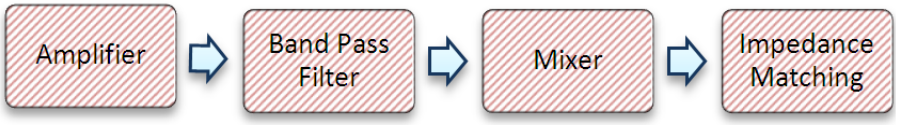

Figure 7.4: Subcomponents of the analog signal conditioning chain

The purpose of analog signal conditioning chain is to make the resonator output appropriate for the ADC output.The Amplifier ensures that the signal covers the full input signal dynamic range of ADC. The bandpass filter attenuates all the frequencies except those that lies within a narrow range containing the resonator/resonator array response.

For appropriate sampling, the signal should be within the sampling bandwidth of the ADC this is ensured by using the mixer. The impedance matching block minimizes the signal level attenuation due to the impedance mismatching between the analog signal conditioning chain components and the input impedance of the ADC.

Since we are designing a wideband digital spectrum analysis system, the bandwidth captured by ADC is large. The resonator within this bandwidth is high Q and thus occupies a narrow bandwidth. Thus a very high resolution spectrum analysis of the acquired ADC bandwidth is required.

The feature magnification and extraction block enables us to take enhanced frequency resolution measurement at subset of frequencies within the available bandwidth of the ADC. Particular features of interest in the resonator output can then be measured more accurately.

Narrow band features require higher resolution in the frequency domain. Frequency resolution is a function of total length of time spanned by sampled data. Therefore, for narrow band features at high data rates, high resolution comes at the cost of a large number of data samples, large FFT size and increased computational complexity. To avoid this the desired feature or resonator response is down converted by digital mixing to a lower frequency and then the data rate is reduced by decimation and filtering. The spectral analysis of this reduced data rate and low frequency signal gives a high frequency resolution without the requirement of very large FFT size. Thus the feature magnification and extraction block can be described in block form as follows.

Figure 7.5: Subcomponents of the Feature Extraction

7.3 Design and Implementation of System Architecture

In the following lines we explain the detailed design and implementation using the above mentioned system architecture.

7.3.1 Hardware Platform

The digital part of the system can be implemented using either a digital signal processor or an FPGA. For our example implementation we chose the XILINX XtremeDSP digital board which houses Virtex 2 FPGA along with 105 MSPS ADC and DAC. This board is installed in the PCI slot of the computer. XILINX provides a tool called System Generator for simulating and generating the FPGA logic blocks in the Simulink® . System Generator also provides a mechanism for Hardware/Software co-simulation whereby the designed FPGA logic runs in the actual FPGA on the XtremeDSP board and has real time interface with the software running in Simulink® . Given all the above mentioned components and features, we can implement a real time data acquisition and analysis system using this board. The board is shown in figure below.

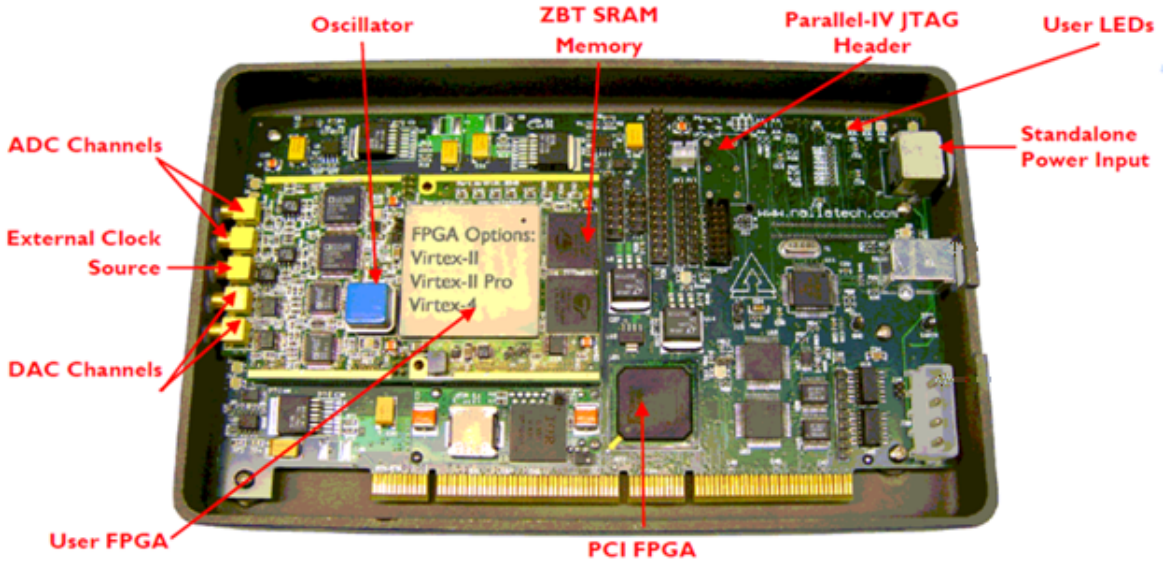

Figure 7.6: XILINX XtremeDSP Board

This board and its specifications are sufficient enough for an example implementation of the proposed architecture and can provide us insights into system design specifications and requirements for an ASIC based stand-alone implementation. These requirements can then be interpolated for estimating resource requirements for more advanced spectrum analyzer implementations. As a test case we design our system for a 10 MHZ QCM resonator; its

VNA measured spectrum is shown below.

The complete system implementation for this board was developed in Simulink® software using the System Generator for DSP^{TM} provided by XILINX . System Generator for DSP^{TM} is a rapid prototyping tool which helps in system modeling and automatic code generation (of programable logic for the FPGA on the XtremeDSP board) from the Simulink® and MATLAB® Environments. Figure 1 below shows the complete system implementation in the Simulink® and is then followed by description of detailed design of each block in the implementation.

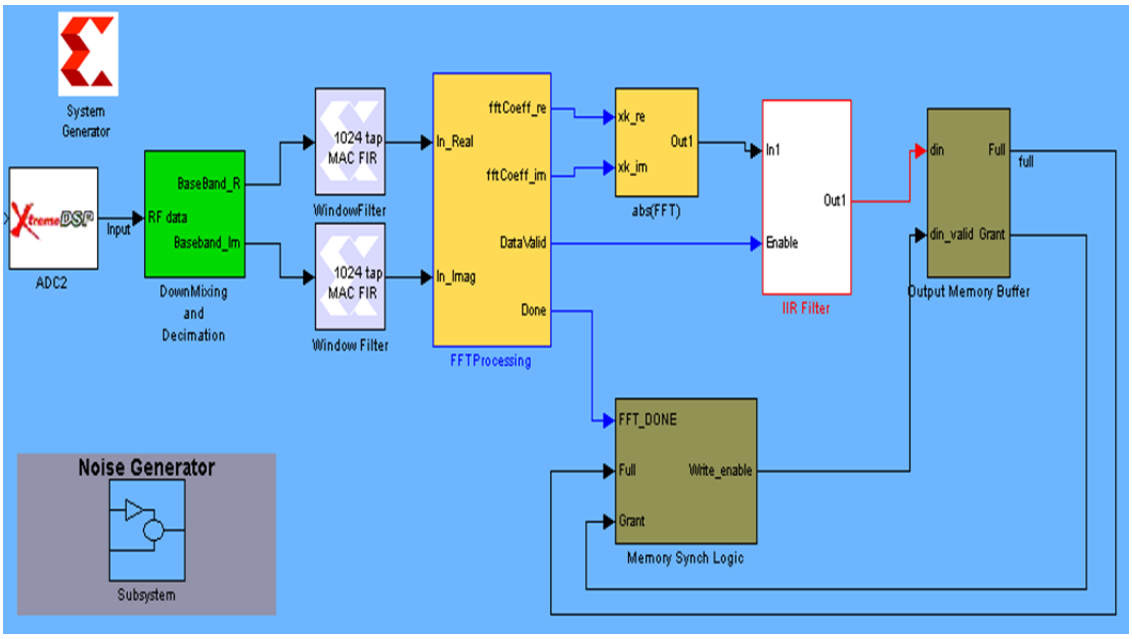

Figure 7.7: System Generator Implementation of the system Spectrum Analyzer

7.3.2 Noise Generator

Figure 7.8: Subcomponents of the noise generator

The noise source FPGA implementation block diagram is shown above. Since our resonator has fundamental resonance at 10 MHz and the complete response spans about 50 kHz, so we designed the noise source to have flat response past 10 MHz. To sample a signal of 10MHz we need to sample it at least twice this frequency, and so we use 30 MHz sampling clock, which requires that the noise signal be band limited to Nyquist frequency of 15 MHz. To achieve such a signal we run the LFSR on 60 MHz clock which gives out a flat white noise spectrum up to 30 MHz This spectrum is further passed through a half band FIR filter to give a low pass band limited white noise spectrum flat up-to 15 MHz. The output of the noise source is shown below

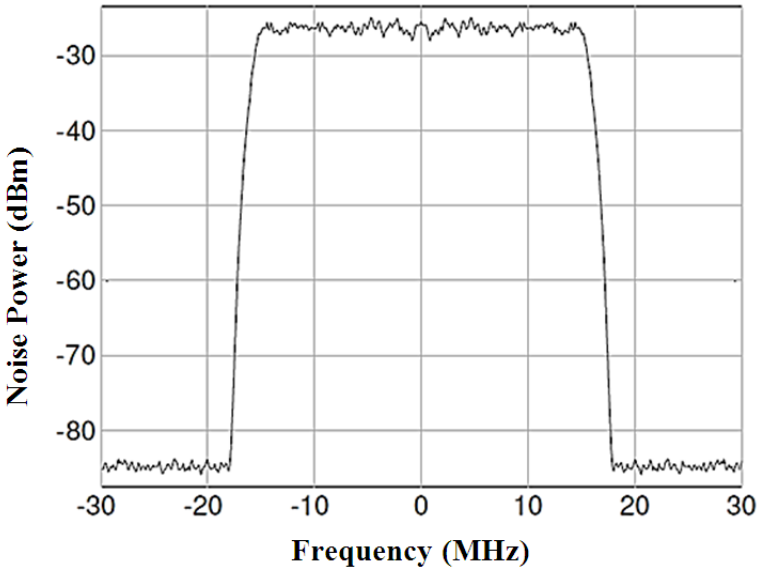

Figure 7.9: Noise Source Output

7.3.3 Analog to Digital Conversion

Analog to digital conversion is the most important part in the digital spectrum analyzer. Many of the attributes of the spectrum analyzer are determined by ADC. ADC has two important parameters (besides the sampling frequency) which ultimately determine its effectiveness at measuring the resonator response. One is the absolute quantization noise floor, which determines the minimum amount of signal power level which must be available at the ADC input to excite a meaningful reading. The other figure of merit is the dynamic

range, which specifies the maximum amount of signal energy above the quantization noise floor, that the ADC can successfully convert to its full scale output without exciting any non linearities in its analog subsystem. This is governed by the signal to quantization noise ratio.

$$\left(\frac{S}{N}\right)_{dB} = 1.76 + 6.02n = DR_{ADC} \tag{7.1}$$

The input signal excitation level, the resonator insertion loss, and ADC dynamic range must all be considered together carefully to make a selection of the appropriate device. The maximum insertion loss of the resonator must not exceed the difference of input excitation level and quantization noise floor. Similarly the minimum insertion loss of the resonator must not exceed the difference of input excitation level and the dynamic range. The ADC in the Xilinx Xtreme DSP board accepts signals in the range of +1 volts to -1 volts. The input port impedance is 50 Ohms and the maximum bandwidth of ADC is 58 MHz. The signal conditioning chain we described earlier must be designed to meet these requirements and the dynamic range considerations. Though for 10 MHz resonator output, we do not need a mixer since our signal is already within the ADC bandwidth. We do however need an amplifier with a variable gain, which can convert the output of the resonator or adjust the input to the resonator so that the output of the resonator spans the full dynamic range of the ADC. The output dynamic range that the FFT analyzer can provide can never exceed the dynamic range performance of the ADC. For very high frequency resonator, such as a 434 MHz SAW resonator, a mixer will be required to up convert the generated noise signal and an another mixer for down converting the resonator output within the ADC bandwidth. The Impedance matching can be obtained by using transformer type circuit. Once the signal is sampled appropriately, we can move on to the analysis and feature extraction blocks.

7.3.4 Feature Magnification and Extraction Block

The QCM resonator used in general for bio sensing applications is very high Q. The resonance frequency is at 10 MHz; however the complete fundamental resonance mode spans only 50 kHz. We need to do spectral analysis with high resolution on this 50 KHz bandwidth. However, if we acquire a signal of 10 MHz by sampling at 30 MHz and take N-Point

FFT. This maps Nyquist frequency Fs/2 (15 MHz) to N/2 points. So each frequency bin in the FFT output spans Δf = Fs/N (30 MHz/1024 = 29 KHz). This implies that the whole QCM response (50 kHz) is concentrate in only two frequency bins, which will give us very poor resolution and the detailed features of the spectral response will be lost. One way to increase the resolution is to increase the size (N) of FFT. However this increases the computation cost and thus consumes higher resources of FPGA fabric resulting in bigger chip area and greater power consumption.

Here we take an alternate approach i.e. to down convert the QCM response from 10MHz to baseband (very close to DC) and then we reduce the bandwidth of the input signal to the FFT by the decimation ratio. FFT of this reduced bandwidth gives high resolution result because each Δf reduces by decimation ratio. As an example, if we decimate the 30 MHz signal by 96 we get Δf = (30 MHz/96 /1024) = 300 Hz. Each frequency bin of the FFT output now spans 300Hz. The QCM response (50KHz) now spans 166 bins, providing a high resolution spectrum of QCM response. Keeping the above mentioned advantages of digital down sampling and decimation in mind we design the feature magnification and extraction block. A block diagram of the feature magnification and extraction has been shown in Figure 7.5. We now look at the details of the sub components and highlight the theoretical basis of the design.

7.3.4.1 DDC (digital down conversion)

We now look at the underlying theory for digital down conversion. First step in digital down conversion is the multiplication of ADC sampled data with a sinusoidal source. This is done by digital mixer. Digital down conversion requires a digital data synthesis source for generating sine wave of known frequency. This sine wave acts as an oscillator input to a mixer and the output of the ADC acts as RF input. Lets look at the change in spectrum due to the multiplication with a sinusoidal signal mathematically. Consider the multiplication of an input time domain function f(t) by a $\cos(\omega t)$. Since by euler identities we can write $\cos(\omega t) = (e^{j\omega t} + e^{-j\omega t})/2$. So we first look at the multiplication of f(t) by e^{jwt} and its

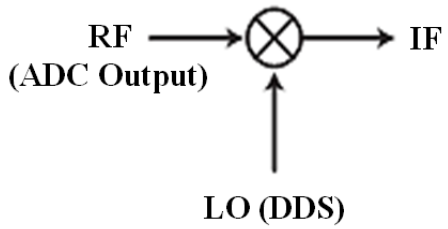

Figure 7.10: Digital Down Conversion

corresponding fourier spectrum.

$$\begin{aligned}\mathcal{F}\{e^{(j\omega_0 t)}f(t)\} &= \int_{\infty}^{\infty} f(t)e^{j\omega_0 t}e^{-j\omega t}\,\mathrm{d}t \\ &= \int_{\infty}^{\infty} f(t)e^{-j(\omega-\omega_0)t}\,\mathrm{d}t \\ &= F(\omega-\omega_0)\end{aligned} \tag{7.2}$$

Thus we see that multiplication by complex exponential results in the shift in the frequency spectrum. Consequently multiplication by $\cos(\omega t) = (e^{j\omega t} + e^{-j\omega t})/2$ will result in

$$\mathcal{F}\{\cos(\omega_0 t)f(t)\} = \frac{1}{2}F(\omega-\omega_0) + \frac{1}{2}F(\omega-\omega_0) \tag{7.3}$$

i.e we get sum and difference components. In comparison, duue to multiplication with a single sinusoidal we incur the image problem. Consider as an example that we have our ADC/RF signal at 1GHz = 1000 MHz. Let's choose LO= 900 MHz This gives an IF of 100 Hz. But this also means that any signals or noise at 800 MHz will also be down converted to the same IF in addition to the RF signal at 1000 MHz. This unwanted signal is called image signal and 800 MHz is called as image frequency. In more generic terms the image frequency is the second frequency that also down-converts to the same IF. This is undesirable because the noise and interference at the image frequency can potentially overwhelm the desired down converted RF signal.

Now let's look at the down conversion process graphically for both cases of single sinusoid down conversion or complex down conversion.

This spectrum is modified by modulation with complex exponential or real sinusoidal signal. The difference between the two modulations is shown in the figure below. Here we

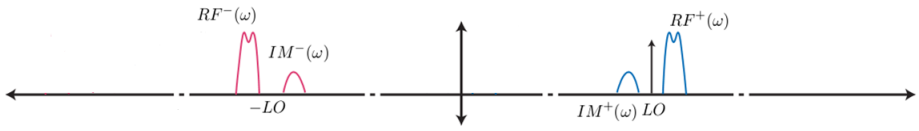

Figure 7.11: Complex Spectrum at the output of ADC;Showing image and RF components

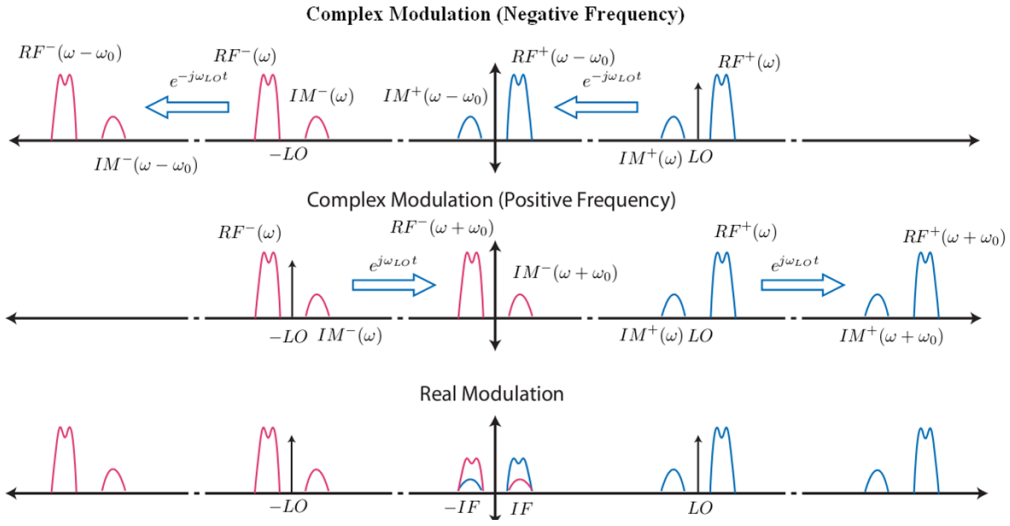

Figure 7.12: Complex Modulation vs Real Modulation [3]

can see that in the case of multiplication by a real sinusoidal signal the image spectrum overlaps the RF down converted spectrum and thus causes problems. Whereas, there is no image problem in the case of modulation by complex exponential. To achieve the complex modulation with real signals we use sine and cosine modulation as shown below

Thus we see that in the case of delayed sine we have a very desirable situation where the image is inverted with respect to the cos modulation and can be canceled. We have given such a detailed discussion of the digital down conversion and image cancelation, because image rejection is very important for wideband noise excited resonator response. In the case of of noise excited resonator response, the signal at the output of the ADC is not bandlimited to just the resonator bandwidth, it always contains the noise signal at the image frequencies and at the same or higher power level as the resonator response. Therefore, it was essential to understand the image frequency problem and its cancelation.

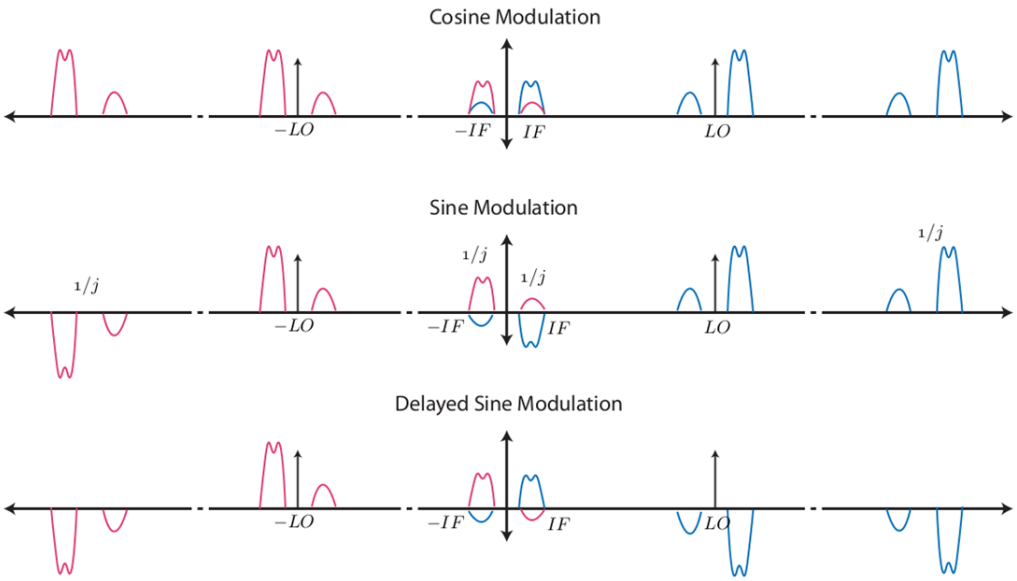

Figure 7.13: Sine Cosine modulation to eliminate image problem [3]

7.3.4.2 Digital Down Sampling

By using the digital down conversion we have converted the resonator response in the spectrum of the ADC sampled data to baseband (very close to DC). Thus only a small part of the bandwidth sampled by ADC contains our desired spectrum. We use digital down sampling and filtering at this stage to get rid of the excess bandwidth. Therefor, our FFT block will be able to compute high resolution spectrum of a much reduced bandwidth. The decimating filter structure could take several forms. It can be a combination of different types of filters including CIC, decimating FIR and polyphase structures. The CIC filter is a highly efficient multiplier-less structure capable of very high integer decimation. Different combinations of these filters were simulated to find the optimal bandwidth and side lobe attenuation level.

7.3.4.3 Windowing and FFT

In the previous section we discussed the use of digital down conversion and down sampling to improve the spectrum resolution. For FFT analyzers the second factor that affects the resolution is windowing. FFT analyzers use the Fast Fourier Transform (FFT) algorithm to compute the Discrete Fourier Transform (DFT). In the mathematic of DFT ,there is

an inherent assumption that the data being processed is a single period of periodically repeating signal. FFT takes in N-point frames of data and computes N-point FFT output. The discontinuities between successive frames introduces artificial artifacts not present in the original signal. This effect produces new frequency components that is called as spectral leakage. To avoid sudden discontinuities each data frame is multiplied with a smoothing window function. The window functions usually have a bell shape that reduces or eliminates the discontinuities at the end of the FFT frame. There are several different types of window functions that are discussed in detail in [86]. Following the window block the FFT block computes the N-point FFT frame. The block can be configured for N = 32 to 2^14 Points FFT. We are showing here an implementation of 1024 point FFT.

7.3.5 Spectrum Smoothing through IIR filtering

The FFT power spectrum output needs to be averaged to reduce the variance in the spectrum measurement. Thus we average multiple N-point FFT frames to increase the FFT sensitivity or reduce the noise variance. This is called as integration gain. When multiple FFT outputs are averaged, the random noise fluctuations in an FFT's output bins will decrease, while the magnitude of the FFT signal bin output remains constant. The multiple FFT averaging can be done in two ways, coherent and incoherent. In coherent averaging we average the real and imaginary part of multiple FFT frame before taking the magnitude.In incoherent averaging we average the magnitudes of multiple FFTs. In real world signals the incoherent averaging provides better gain compared to coherent averaging as discussed in [86]. In detail each averaged FFT bin is the average of the corresponding bin magnitudes of multiple FFTS i.e the zeroth bin of incoherently averaged k FFTs, Fincoh(0) is given by

$$F_{incoh}(0) = \frac{|F_1(0)| + |F_2(0) + |F_3(0)| + ... + |F_k(0)|}{k} \tag{7.4}$$

And the last bin of the FFT average, $F_{incoh}(N-1)$ is given as

$$F_{incoh}(N-1) = \frac{|F_1(N-1)| + |F_2(N-1) + |F_3(N-1)| + ... + |F_k(N-1)|}{k} \tag{7.5}$$

To obtain the averaging we employ the exponential moving average filter. The following

equation defines the exponential moving average filter.

$$y(n) = \alpha x(n) + (1 - \alpha)y(n - 1) \tag{7.6}$$

Where $y(n)$ is the current average output sample, $y(n-1)$ is the previous average output sample, and α is the weighting factor constant. The output $y(n)$ is the weighted average of the current input sample and previous average output sample. This scheme can be implemented by the diagram shown below. The advantage of the of exponential averaging is that only one storage register is needed to hold the value $y(n-1)$ while waiting for the next input data sample $x(n)$.

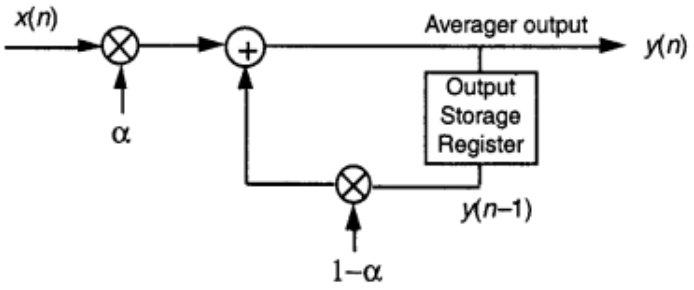

Figure 7.14: Exponential Averaging Filter for spectrum smoothing

This implementation is the same configuration as a single tap IIR filter. The average is output response or impulse response is shown in the figure below with alpha = 0.4. The noise reduction capability of exponential moving average filter is given by

$$SNR_{exp_{dB}} = 10.log_{10}\left(\frac{\alpha}{2-\alpha}\right) \tag{7.7}$$

By decreasing alpha increased noise reduction is achieved but that also results in slower response to input changes. When the moving average filter is applied to average multiple N-point FFTs then we have to store the last N-point output of the FFT averager. The single tap IIR architecture is executed for each of the N points of the FFT . This is accomplished by using an addressable shift register which evokes the kth point previous averager output for the k_{th} bin of the FFT to execute the IIR exponential averaging on the kth bin of the input data sample. The resulting IIR configuration is shown in figure below. This IIR configuration outputs a complete averaged FFT frame after every N clock cycles.

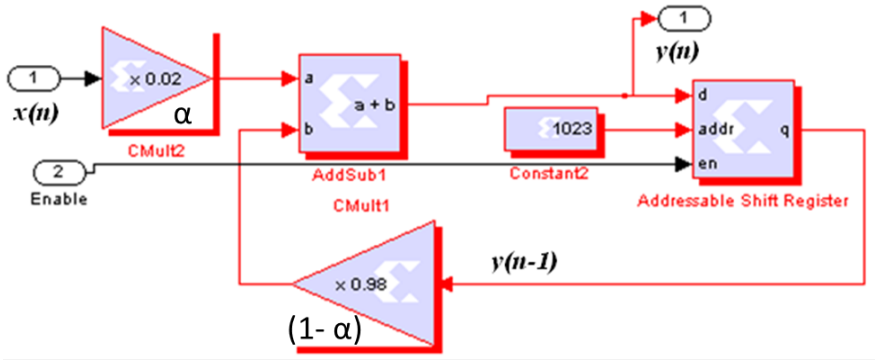

Figure 7.15: FPGA implementation of Exponential Averaging of multiple FFT frames

7.3.6 Interface with Host Computer

The complete digital system for spectrum analysis shown earlier in Figure 7.2 is compiled as hardware logic and runs in the FPGA of XtremeDSP board. The data acquired and processed by this board needs to be transferred to the Host Pc for further analysis and display purposes. The data transfer between hardware and software is achieved through memory blocks that are shared between the simulation software on the host PC and hardware in the FPGA. The memory block stores the output of the power spectrum analysis that is in the form of N-point FFT frames.

The memory block thus holds multiple FFT frames and is read by the host PC when it is full. The particular form of memory share implemented here is called lockable shared memory block in the System Generator terminology.

When the 'Hardware' is accessing the shared memory block it has to acquire a lock of the memory. During this while the software can't access the memory block and vice versa. Two images of the shared memory data are used when a lockable shared memory is co-simulated. One memory image is stored using dual port memory in the FPGA. This image is accessed by the System Generator hardware co-simulation design and co-simulation interfacing logic. The other image is implemented as a shared memory object on the host PC. This software shared memory image is accessed by any software shared memory objects used in a design.

Having two shared memory images requires synchronization between software and hardware to ensure the images are coherent. This synchronization is accomplished by transferring the memory image between software and hardware upon lock transfer.

Every time there is a transfer between the hardware in FPGA and the host PC software, there is some overhead associated with it. To reduce this overhead costs it is desirable to reduce the number of transfers between host and PC. This is achieved by bundling together as many data point in one transfer. In our case instead of dong the transfer as every frame of N-point FFT is completed we use a memory buffer large enough to hold multiple FFT frames at one time.

At this point it is important to remember that the Host PC simulation software is running at a different clock rate and the FPGA hardware compilation is running at a different clock rate. In sysgen terminology this is termed as FPGA free running mode. This allows the FPGA acquire the input data through the ADC in a continuous stream fashion independent of the timing constraints of the host pc simulation software. Thus the FFT block outputs data byte by byte in a continuous stream. To signal the complete frame it makes the 'Done' output high for one clock cycle. The blocks following the FFT such as abs (FFT) and IIR also operate on the continuously streamed data. Thus we use the done signal to determine the beginning and the end of an FFT frame. This FFT frame boundary should always be preserved. We may lose some data to processing delay, but then we have to lose the whole frame to preserve the frame boundary and thus ensuring that data stored in the memory buffer is always a full frame. This is the purpose of the memory buffer synching logic.

The memory buffer synch logic generates a write enable signal for the memory buffer. This write enable signal is dependent on the FFT blocks "DONE" signal the "Grant" and "Full" signal of the Memory block. Since the memory is configured to work in the lockable state, the request has to be made before getting access to the memory. When Grant signal of the memory block becomes one then the request has been granted to access the memory for read or write purposes. So we start with the Grant signal being one. Now we have access to the memory. We want to write the data to the memory buffer. First condition on

this data is that the first byte to be written has to be the first byte of a new FFT frame. When the "Done" signal of the FFT becomes high then we know that the next byte is the first byte. So we use the Complement of the Grant signal as the reset of the SR and "Done" as the reset of an "SR flip flop_1". The output Q of this SR flip flop becomes high when the "Done" (set) is high and 'Grant' signal (reset) is low. This high output Q will enable the Write enable to the memory block. When the memory becomes full the "Full" signal of memory block becomes high this resets the other flip flop the "SR flip flop", the logic following this flip flop will then make the write enable to the memory low thus stopping the write process. Thus the memory is written only when it has space (Full signal low), and if the access to the memory is available (Grant signal high) and guarantees that every time a Full Frame of N-point FFT data is written into the memory.

7.3.7 Hardware Synthesis and CoSimulation

Now we have discussed the complete system shown in Figure 7.7. The complete system is compiled for hardware logic implementation. This hardware compilation is available then as a library block for co-simulation in the host pc software i.e. Simulink. The simulation setup in the host PC is shown in Figure 7.16.

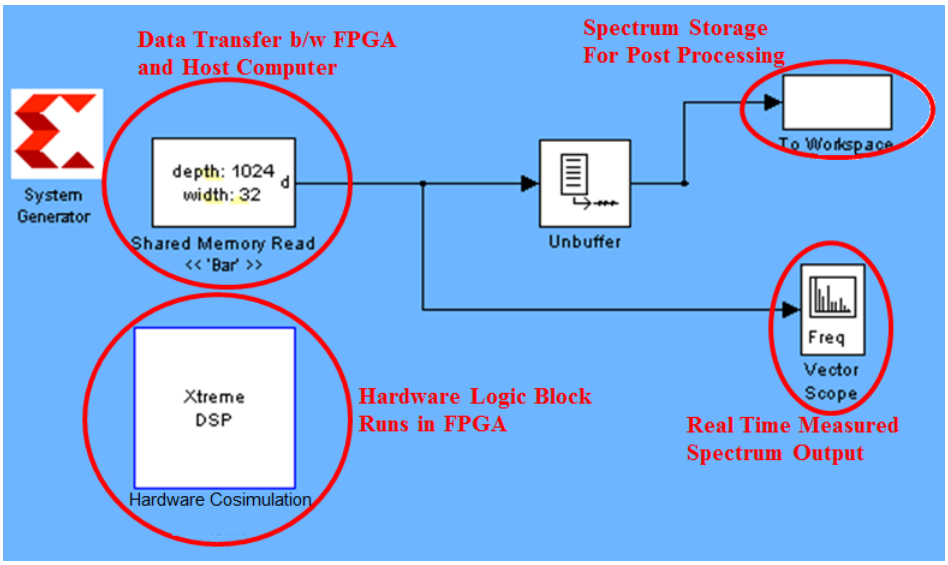

Figure 7.16: Host PC setup for real time spectral analysis

This figure holds the hardware co-simulation block "Xtreme DSP". This block is the interface to the XtremeDSP development board and the hardware compiled logic on the FPGA of the board. During the simulation this block behaves exactly as a subsystem of the Simulink® simulation except that the simulation data is processed in hardware in real time instead of software.

This block can have input and output data ports to exchange data with other Simulink® blocks in the simulation. In our case we only do the exchange through the lockable shared memory interface. The Shared Memory Read block in this simulation is invoked at particular intervals of time to interact with the shared memory object in the hardware. When it is invoked it tries to acquire the lock of the shared memory. Once the lock is acquired it reads the data from the shared memory object and then releases the lock. The read data is written to block's output data in the Simulink® vector or matrix form. This data can then be displayed on a graphical scope in real time or saved for post processing purposes.

7.4 Measurements and Post Processing

In this section we will present the measurements of spectrum of a 10 MHz QCM resonator using the system developed above. This is followed by a discussion on post processing this measured data to obtain the information relevant for sensing purposes. The following figure shows the measured output of a QCM resonant at the fundamental resonance frequency of 10 MHz. This is a real time output of a bare QCM which is excited with the digital noise source generated by our digital system. The same QCM was then loaded on one side with a water droplet to obtain the response of QCM (Figure 7.18) under water loading. As expected the response of the QCM is significantly dampened.

In the previous chapter in section 6.4 we discussed that the measurement of resonance frequency f_r and the half-band-half-width (HBHW), Γ, of the resonator are generally used to extract the information about a sensing event from the resonator response. These two parameters are obtained by fitting a theoretical resonance curve, the Lorentz curve , to the measured resonator response. The Lorentz curve is given by the following equation

$$I = \frac{\frac{BW}{(2*pi)}}{(f - f_r)^2 + \frac{BW^2}{4}} \tag{7.8}$$

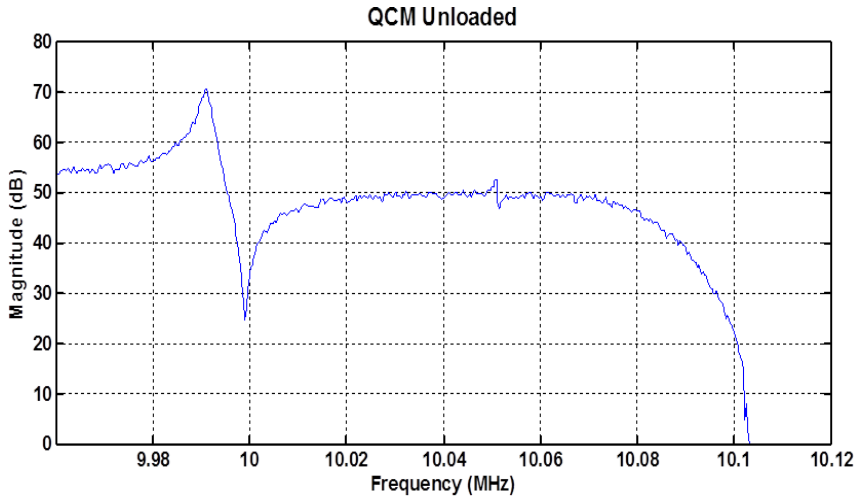

Figure 7.17: Measured Spectral Output of noise excited QCM (10 MHz)

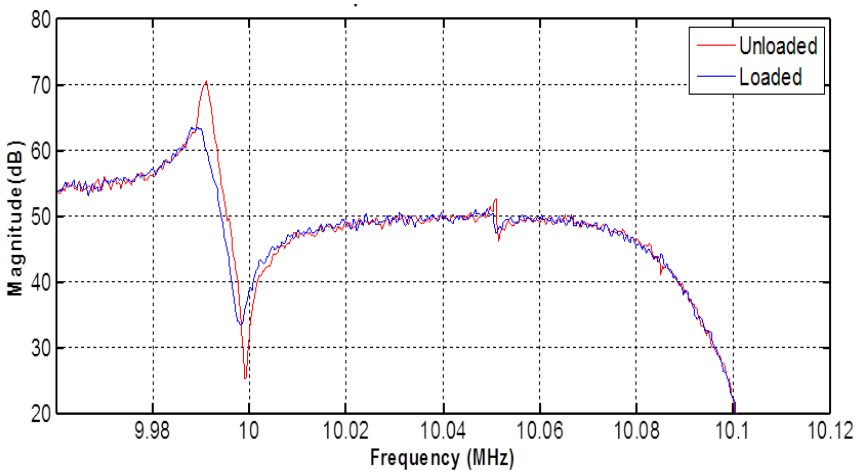

Figure 7.18: Water loaded response of QCM measured by the digital system compared to unloaded response

where BW is full bandwidth at half the maximum amplitude of the resonator response. Γ is half of BW. The resonance frequency and the bandwidth are extracted from the fit. The lorentz curve is a linear intensity function so we do the curve fitting to linear magnitude QCM response (Figure 7.19) rather than on dB scale. The fitted curve will give us the resonance frequency and the bandwidth of the resonance.

Figure 7.17 was a snapshot of real time output of the digital system presented above. As shown in Figure 7.16 the developed system is capable of simultaneously storing the

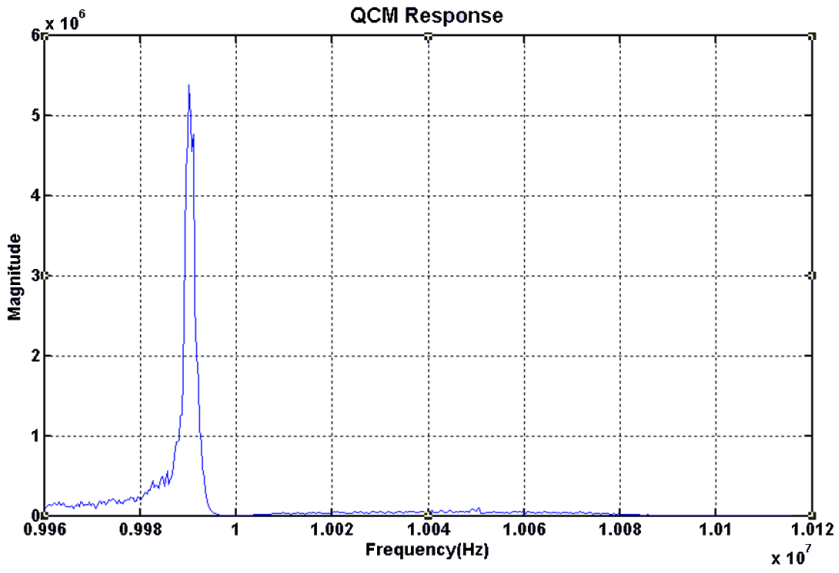

Figure 7.19: Linear magnitude plot of QCM

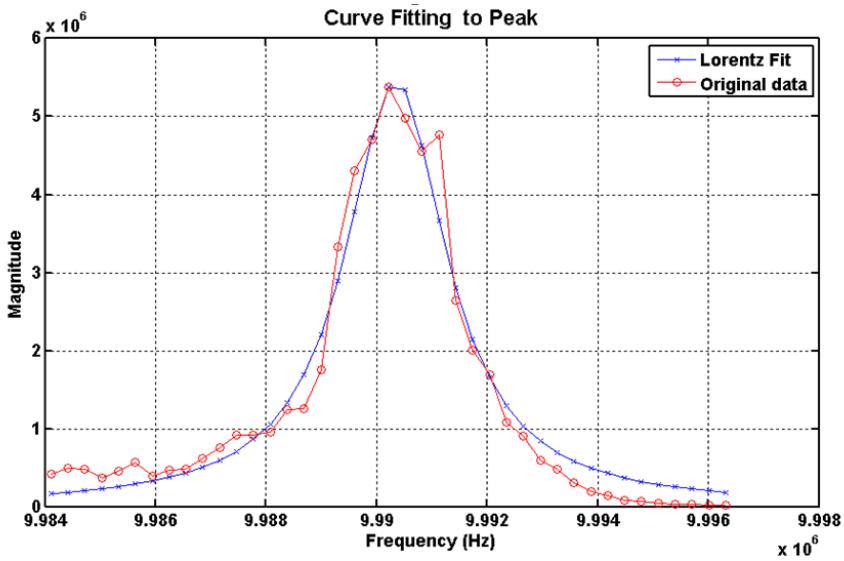

Figure 7.20: Lorentz curve fitted to the linear QCM response

measured spectrum. This stored spectrum can be used to extract the characteristic features of the resonator (i.e resonance frequency and bandwidth obtained by lorentz curve fitting) as a function of time. To record the time changing response of QCM, a drop of water was deposited on the QCM surface and was allowed to evaporate under room temperature and pressure conditions. Change in resonance frequency and bandwidth with respect to

unloaded case is then plotted verses time. Resulting graphs are shown in Figure 7.21 and Figure 7.22.

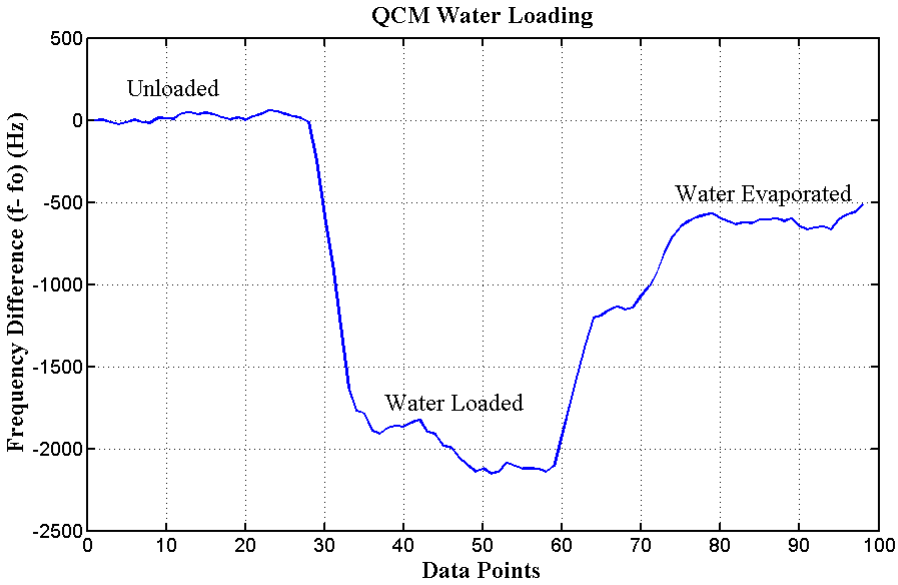

Figure 7.21: Change in Resonance frequency of QCM under water loading and evaporating conditions

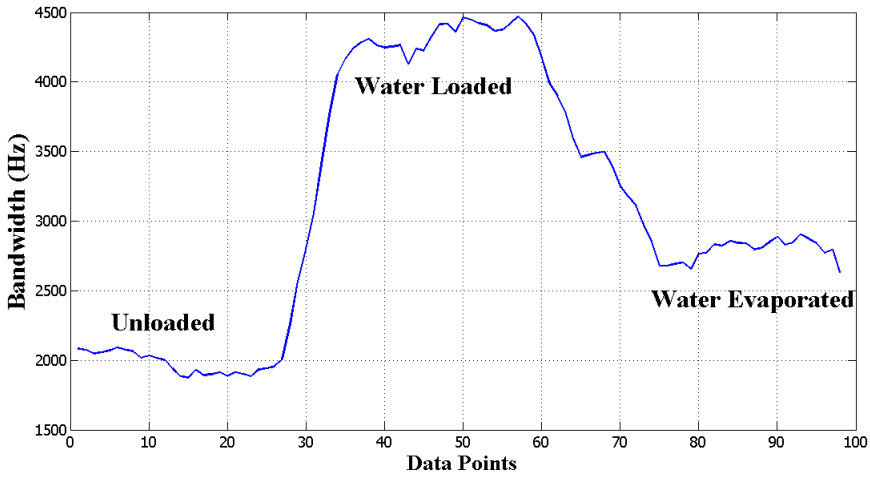

Figure 7.22: Time plot of QCM bandwidth change due to water loading

7.4.1 Sensing Information in Γ and $\tilde{f}$

In Chapter 1 we discussed that the acoustic transducers are converted to sensor by functionalizing the surface of the acoustic resonator with a chemically sensitive layer. The functionalized resonator is then exposed to a medium containing the target molecule. Now we look at how the surface changes affect the resonator response. In particular, we look at the two resonator parameters discussed in the previous section i.e the resonance frequency and Γ and their information content with regards to sensing. We define complex frequency ($\tilde{f}$) using these two components with f_r as real part and Γ as the imaginary part. Complex frequency can be used to characterize the changes at the surface of the resonator. A useful concept in this regard is the acoustic load impedance which is defined as the ratio of stress to speed at the surface of the resonator(where speed is the velocity of the propagation of acoustic waves that setup the resonance). The load impedance sums up the effect on acoustic resonance due to the changes at the surface of the resonator. The relationship between the complex frequency and the acoustic load impedance is given as follows [83].

$$\frac{\Delta\tilde{f}}{f_f} = \frac{\Delta f + i\Delta\Gamma}{f_f} \approx \frac{i}{\pi Z_q} Z_L = \frac{i}{\pi Z_q}\frac{\sigma}{\dot{u}} \tag{7.9}$$

Where f_f is the frequency of fundamental resonance, Z_q is the acoustic impedance of the resonator, σ is the average stress at the surface of the resonator, u_o is the particle displacement at the surface and $\dot{u} = i\omega u_o$ is the speed. This equation is the most important equation of the physics of the BAW resonator. As long as the frequency shift is small compared to the frequency , the complex frequency shift is proportional to the load impedance a the resonator surface. This equation at the moment is independent of the nature of surface load or sample present at the resonator surface. The surface impedance could be used to model many different kinds of surface loads but in practice, for acoustic biosensors the surface load consists of a surface coating layer in contact with the a liquid medium containing the target analyte. Therefore our interest lies in the effects of a viscoelastic medium (liquid samples i.e blood, cell lysate, saliva, urine etc) on the resonator response and the effect of a thin film in the presence of a viscoelastic medium(surface functionalization layer in the presence of liquid bio samples) to the resonator response. First, we look at the effect of just a thin film

deposited on the resonator surface in air. A very thin film will have only the inertial effects and the stress produced is given by $\sigma = -\omega^2 u_o m_f$ where u_o is the amplitude of oscillation and m_f is the average mass per unit area. Inserting this into the equation 7.9 gives us the following relation:

$$\frac{\Delta\tilde{f}}{f_f} \approx \frac{i}{\pi Z_q} = \frac{-\omega^2 u_o m_f}{i\omega u_o} - \frac{2f}{Z_q} m_f \tag{7.10}$$

which is the Sauerbrey equation. This equation holds for very thin films such that their viscoelastic properties can be ignored. With the increase in the thickness of the film its viscoelastic properties may influence to be considered. More complex modeling of the viscoelastic effects is needed. The complex frequency shift and load impedance relation for viscoelastic medium has been derived and dicussed by D.Johanssman in [83].We will summarize some of the key relations in the following lines. The change in complex frequency due to a viscoelastic medium present on the resonator surface is given as:

$$\frac{\Delta\tilde{f}}{f_f} = \frac{i}{\pi Z_q}\frac{\sigma}{\dot{u}} = \frac{i}{\pi Z_q} Z_{liq} == \frac{i}{\pi Z_q}\sqrt{\rho_{liq} i\omega\eta} \tag{7.11}$$

$$= \frac{1}{\pi Z_q}\frac{-1+i}{\sqrt{2}}\sqrt{2\pi n f_f \rho_{liq}(\eta' - \eta'')} \tag{7.12}$$

where $\eta = \eta' + i\eta''$ is the complex viscosity and p_{liq} is the density of the liquid.

The combined effect of a coating layer and a liquid sample can be characterized by the following equation.

$$\frac{\Delta\tilde{f}}{f_f} = \frac{i}{\pi Z_q}(Z_{tot} - Z_{liq}) \tag{7.13}$$

$$= \frac{-\omega m_f}{\pi Z_q}\left(\frac{Z_f^2 - Z_{liq}^2}{Z_f^2}\right) \tag{7.14}$$

Where Z_f is the acoustic load impedance of the film coating. This equation without the terms in the bracket on right side is equivalent to Sauerbrey relation. The terms in the bracket are the viscoelastic correction to the sauerbrey frequency shift.

7.4.1.1 The information content of the $\Delta\Gamma$ to Δf ratio

The complex frequency shift is dependent on the mass of the film m_f which is not known independently. This mass can be eliminated by taking the ratio of shift in half-band-half-width, $\Delta\Gamma$, and the negative shift in frequency, Δf

$$\frac{\Delta\Gamma}{-\Delta f} = \frac{-Im(1 - i\omega\rho_{liq}\eta J_f/\rho_f)}{Re(1 - i\omega\rho_{liq}\eta J_f/\rho_f)} = \frac{\omega\rho_{liq}\eta J_f/\rho_f}{\rho_f - \omega\rho_{liq}\eta J'_f/\rho_f}. \tag{7.15}$$

where $\rho_f$is the density of the film,$J_f = J'_f + iJ''_f$ is the complex elastic compliance of the film. For practical cases the film is more rigid compared to the ambient film and we can arrive at a simpler relation.

$$\frac{\Delta\Gamma}{-\Delta f} \approx \frac{\rho_{liq}}{\rho_f} 2\pi n f_f \eta J'_f \tag{7.16}$$

The equations described in this section give us a better understanding of the acoustic interaction between the resonator and surface load. These equations establish the usefulness of using the resonator parameters i.e Δf and $\Delta\Gamma$ and have highlighted their information content with regards to bio sensing. We have shown that by using both of these parameters, a lot more information about the surface load can be obtained, rather than just using the change in frequency. There has been a lot of research in exploiting these two parameters for different kinds of sensing application and a very detailed and comprehensive account of this research is provided in [83]

7.4.2 Conclusion

In this chapter, we have presented the design of a stand alone system for SANER. We have also given theoretical basis of the design. We have given an example implementation for 10 MHz QCM resonator and demonstrated the use of stand alone system for characterization and tracking of resonator response. The purpose of example implementation given here is to show the design approach towards digital implementation of the saner system idea 6. The design presented here establishes the feasibility of a a stand alone implementation as wells as it provides a footprint towards more advanced and generalized implementation.

The current system implementation is scalable. The extents of scalability are determined by hardware mostly. The maximum output bandwidth of DAC is 80 MHz. The maximum

input bandwidth of the ADC on the XILINX XtremeDSP is 57.9 MHz. Thus the current system is capable of measuring any resonator or resonator array whose spectral response is less than 57.9 MHz without changing the hardware. This is significant compared to the oscillator circuits, in which case the whole circuit usually needs to be redesigned for different resonators. The architecture of the digital spectral analyzer will stay the same but it may need some customization according to the resonator frequency such as the frequency of the sinusoidal input for complex down conversion needs to be changed according to where the resonator response lies in the captured ADC bandwidth. For resonators at much higher frequency i.e in GHz range we will need to use external hardware to mix down the resonator output down to the input bandwidth of the ADC. In addition the noise generator also needs to be modified to be able to excite the resonator response at GHZ range. However, the digital system that has been presented here will still be valid. There is room for improvement in the digital system to provide more accurate spectrum estimation. Advanced methods of digital spectral estimation have been discussed in [2,87]. For implementation of these methods one has to keep in mind that the computational load remains such that the real time nature of stand alone system is not effected.

CHAPTER VIII

CONCLUSIONS

8.1 Summary

The work presented in this thesis is directed towards a holistic effort aimed at the design of an acoustic biosensor system to aid in the diagnosis and prognosis of cancer diseases. The individual components of a biosensor system are usually spread over several non overlapping research areas and therefore it was necessary to study different facets of the problem in order to aid in the efforts towards providing an optimal biosensor design. Chapter 1 described the individual components of research in detail and subsequent chapters build upon this introduction to delve deeply into various technical challenges of the biosensor design.

Transducer being the principal component of any biosensor, attracted a large portion of the research efforts. Chapter 2 described in detail the design of the transducer, covering the theoretical aspects, the practical fabrication challenges, and some measured results. We described a novel design of a single structure device that is simultaneously resonant in multiple modes. Such a device can have potentially useful applications for sensing purposes. For multi-mode device design, we described a new method for characterizing a multi-mode reflection coefficient of an acoustic reflector. We showed that multiplying the individual reflection coefficients of the TSM and longitudinal modes of an acoustic reflector allows for a simple determination of the appropriate piezoelectric layer thickness for the excitation and support of both modes. The measured resonant frequencies show the existence of the TSM and TE mode frequencies within the respective reflection bands of the reflector. In addition, the existence of a hybrid mode was observed in all devices, with resonant frequencies in between, and non-harmonically-related to, the TSM and TE modes.

The existence of this mode opens doors to the possibility of extracting more information about a sample under test than just the TSM or longitudinal modes. The observation of this mode was first published in Applied Physics Letters as well as an invention disclosure

[31,36]. The physical description of the mode was later published in the Journal of Applied Physics [28].

The focus of Chapter 3 is to achieve a better understanding of the multi-mode device designed in the previous chapter. We presented a very thorough characterization of the multi-mode devices using simulation, theory and experiment to gain an insight into the device behavior and characterize its response. This characterization and understanding is essential for making use of the device as a bio sensor.

We first showed using FEM simulations that several factors affect the TSM, which result in changing the resonance frequency from the theoretically predicted value. We showed that the energy profile of TSM is contained under the top electrode and extends beyond the piezoelectric layer into the electrodes and the top layer of the reflector stack. Thus TSM resonance deviates from theoretical values as it will depend on the material properties of the top layer of reflector stack and the electrode's material. Moreover, the fact that the energy of the TSM mode is concentrated under the top electrode is important from the sensing point of view as the sensitivity of TSM could only be in the areas where its energy is present.

We then explored the physics of the Hybrid mode. We presented the hybrid mode as a mode that is different from both the TEM and TSM and showed through theory, simulations and experiments that the hybrid mode is a coupled mode with both longitudinal and shear particle displacements. Lastly we presented the preliminary multi-mode device characterization with the viscosity and conductivity measurements. These measurements indicate the useability of the multi-mode device for liquid phase biosensing.

In Chapter 4, we discussed the microfluidics required for liquid phase operation of the biosensor. Carefully attention liquid phase operation is necessitated by the fact that most of the biosensor usage scenarios will happen in liquid mediums. After the device functionalization using chemically sensitive layers, the amount and location of the liquid sample over the devices must be controlled for successful liquid phase measurement. In addition the probing pads of the device must be isolated from the active area of the device exposed to the sample to ensure an accurate measurement. For this purpose we investigated the use of

SU-8 polymer barriers for liquid containment. The design of microfluidics mask, the recipe of SU-8 fabrication process, and the challenge of making it compatible with ZnO-based devices are discussed in this chapter.

In Chapter 5, we focussed on the aspects of biosensor design which impart the sensing functionality to our acoustic transducer i.e the functionalization of the transducer by immobilizing a chemically sensitive layer on top of our acoustic transducer. We highlighted the importance of oriented immobilization and reversible scheme for preserving the activity of immobilized proteins and to allow for regeneration of the device surface. We presented Histidine-Ni interaction based surface chemistry as a suitable technique for oriented and reversible immobilization. In this chapter, we showed our efforts at using this functionalization approach on our ZnO based devices with Ni-NTA terminated alkane-thiol SAM and Ni-NTA terminated organosilane SAM. We also suggested the use of a thin layer of Silicon Oxide on top of ZnO as a protective layer to prevent the etching of ZnO during the immobilization procedure. We also presented a preliminary investigation of using our ZnO based BAW resonator devices as a biosensor for detection of Head and Neck Cancer biomarkers. The results of these experiments demonstrated that our device are capable of detection of biomarkers in complex medium such as cell lysate and that they exhibit very high sensitivity and selectivity compared to ELISA based detection of the same biomarkers.

Chapter 6 focuses on describing a new method for extracting data from resonator based sensing devices, which leads toward an easy electronic interface for sensor systems. The electrical interface to the transducer/resonator plays a very important role in achieving the goals underlined for our biosensor system in Section 1.1.1. This interface allows for accessibility of the transducer response, determines its usability, manufacturability (to some extent), and its cost. Thus a low cost, easy to use interface to the transducer can enable the ubiquitous presence of the biosensor. In this chapter, simulation results are first presented for verification of the proposed system, followed by measurement results with a prototype implementation. The accuracy and speed of the system can be further improved by FFT-based digital implementation of the spectral analysis system. This will allow for a low-cost

and compact stand-alone implementation. We discuss the system architecture for this stand-alone implementation in Chapter 7. The system architecture consist of two major parts i.e. the analog signal conditioning chain and the FFT based digital spectrum analyzer. The design of this system is presented according to the specifications followed by measurements and a discussion on results.

8.2 Author Contributions

The work presented in this these has been published in a wide variety of journals and several invention disclosures. This section contains a list of the author's contributions.

8.2.1 Peer-reviewed journal publications

1: **F. Munir**, A. Wathen, and W. D. Hunt, "A novel parameter extraction method for acoustic wave resonators based on wideband noise excitation," *Review of Scientific Instruments*, vol. 82, pp. 035119-7, 2011.

2: A. Wathen, **F. Munir**, and W. D. Hunt, "Trapped Hybrid Modes in Solidly-Mounted Resonators Based on c-axis Oriented Hexagonal Crystals," *Journal of Applied Physics*, vol. 108, pp. 114503-8, 2010

3: A. Wathen, **F. Munir**, and W. D. Hunt, "A high-Q hybrid acoustic mode in thin film ZnO solidly mounted resonators," *Applied Physics Letters*, vol. 95, pp. 123509-2, 2009.

8.2.2 Conference Publications/Presentations

1: **F. Munir**, A. Wathen, and W. Hunt, "A GHz-range, Single-Structure, Multi-Mode ZnO Solidly-Mounted Bulk Acoustic Resonator", 2010 Ultrasonics Symposium, San Diego, CA, October, 2010

8.2.3 Non-peer-reviewed presentations

1: **F. Munir**, A. Wathen, G. Cooley, R. Tarleton, and W. Hunt - "Acoustic Microarrays (AC$\boldsymbol{\mu}$Ray$^{\mathrm{TM}}$) for Testing the Efficacy of Treatments and Vaccines for Trypanosoma

cruzi Infection", Poster presented at the Georgia Research Alliance Roundtable, Centers for Disease Control, April 2008

2: A. Wathen, **F. Munir**, and W. D. Hunt, "The Use of a High-Q Hybrid Acoustic Mode ZnO Solidly-Mounted Resonator for the Detection of Head-and-Neck Cancer Biomarkers", Poster for the Georgia Tech Research and Innovation Conference, February 2010

8.2.4 Provisional Patent Applications

1: **F. Munir**, A. Wathen, C. Corso, A. Dickerber, W. D. Hunt, "A Solidly-Mounted, Multi-Mode ZnO Bulk Acoustic Wave Resonator," U.S. PTO, 61/382,680, September 2010

2: **F. Munir**, A. Wathen, W. D. Hunt, "A High-Q Hybrid Acoustic Mode in Thin Film ZnO Solidly Mounted Resonators," U.S. PTO, 61/381,233, September 2010

3: **F. Munir**, A. Wathen, W. D. Hunt, "A Novel Parameter Extraction Method for Multi-Frequency Sensor System," U.S. PTO, 61/348,478, May 2010

4: A. Wathen, **F. Munir**, W. D. Hunt, "True-time Bulk Acoustic Stacked Delay Line," U.S. PTO, 61/499,289, June 2011

8.3 Thoughts on Future Work

As mentioned in the beginning of the thesis, the need for a low cost, portable biosensor, is a fundamental need for such a system, in order to enable point of care usage, fast diagnosis and immediate, effective treatment. We have strived to move in the direction to achieve this holy grail of biosensor design by giving a holistic treatment to this optimization problem. There are several extensions possible on this work, which can lead to substantial steps forward in this area of research.

The resonator design, is the most fundamental to entire biosensor system. Chapter 3 opens the way for several directions of future research to improve the resonator design. The effect of electrode and reflector stack needs to be explored analytically and experimentally for resonator with better Q and better sensing properties. Since significant portion of the

mode energy extends into both the electrode and reflector there is room for optimization of resonator response by looking into the design of electrode and reflector stack. Different types of electrode materials and geometries should be explored and different types of materials and thicknesses of the top layer of stack can be tried to optimize the resonator response.

Hybrid mode itself is an excellent starting point for future research. This mode can be potentially useful for sensing purpose as well as other resonator application such as filters and oscillators. Further theoretical and experimental exploration of this mode is required to develop a better understanding of this mode to take it close to field application.

The multi-mode nature of the resonator is also an inviting point for future research. There is a need to explore the use of multiple modes to enhance the sensing information available from a multi-mode device compared to a single mode device. Such a research will involve developing mathematical models, further characterization of each mode for different types of sample loads as well as for environmental factors such as temperature.

The microfluidics design presented in this thesis should be extended in future research to reach at an integrated design that can incorporate microfluidic channels for sample flow control, routing, or mixing etc. The surface chemistry protocols also need to be researched further to allow for precise immobilization of molecules on specific regions of sensor surface to utilize the maximum sensitivity areas of the sensor as well as on specific sensors (in the case of sensor arrays).

For a research effort focusing on the electronics and systems aspect of biosensor design, this thesis offers a good starting point for a lot of interesting ideas and investigations. The thesis has theoretically proposed and experimentally demonstrated a new method of data extraction from biosensors, based on wideband excitation and measurement of spectral signatures. This paradigm of departing from analog oscillator based systems, for sensor response measurement, is a big shift on the previous methods of acoustic biosensor measurement. It offers a range of interesting possibilities. One of them is to adopt a system identification based approach to biosensor measurement. This will start by physical modeling of the transducer and developing a parametric model of the sensor. The parametric model can be linked to physical characteristics directly and to the sensing characteristics

indirectly. This parametric physical model can then be populated using system identification approach, where excitation is tailored in accordance with the response to get the fastest and the most accurate representation of the physical system being identified. This generalized approach of system identification is based on all the components introduced in the new methods presented in this thesis. Wideband excitation noise, the resonator based transducer, and spectral measurements are all a specific manifestation of a general system identification scheme.

The digital system used for processing and learning about the sensor response, offers another possibility of extensive investigation and optimization. Today, many different signal processing techniques exist, which can be applied towards precision measurements from a biosensor system. There are many multi-rate signal processing methods, which offer the possibility of detecting very faint spectral signatures from the data. The chief amongst these family of methods is the multi-resolution analysis, or popularly called wavelet analysis which uses time-frequency methods to provide greater information on physical structures. Already, time domain analysis of biosensors has yielded significant performance enhancements and measurement methodologies for sensor systems [67]. With the combination of multi-resolution analysis and time frequency techniques, these methods can be tied with general system identification approach for faster, more accurate, and more information rich usage of biosensors.

This thesis has also demonstrated the use of a standalone analysis system to be used for response characterization and measurement. As alluded to in the earlier paragraphs, if modern tools of signal analysis and system identification are to be used for biosensor characterization, it is imperative that low power standalone hardware systems be built to interface with physical sensing devices. We have used a prototyping methodology that can be used and extended for such systems. Rapid prototyping methodologies as offered by different electronic system vendors, offer the possibility of trying different hardware architecture to come up with cost, size and power consumption estimates immediately. These methodologies facilitate the researcher the exploration of design space to come up with optimal design solutions. The power profiling of such hardware architectures will

become increasingly important, as we move towards biosensors which are either embedded and/or in perpetual measurement mode. We have identified and implemented one such digital prototyping effort that offers fast estimates of power consumption and area estimates of digital hardware. With more complex algorithms, and more mature system identification approaches, these tools can be used to achieve the goals of portable, or even embedded bio-sensors.

REFERENCES

[1] K. R. Kozak, F. Su, J. P. Whitelegge, K. Faull, S. Reddy, and R. Farias-Eisner, "Characterization of serum biomarkers for detection of early stage ovarian cancer," *Proteomics*, vol. 5, no. 17, pp. 4589–4596, 2005.

[2] J. Lillington, "wideband spectrum analysis using advanced DSP techniques." [Online]. Available: http://www.rfel.com/download/W04009-WidebandSpectrumAnalysisusingAdvancedDSPTechniques.pdf

[3] A. M. NikNejad, "I/q mixers; bjt mixers," *Univeristy of California at Berkley, Course EECS 142: Integrated Circuits for Communications*, 2005. [Online]. Available: http://rfic.eecs.berkeley.edu/~niknejad/ee142_fa05lects/pdf/lect15.pdf

[4] American-Cancer-Society, "Cancer facts and figures 2012," 2011. [Online]. Available: http://www.cancer.org/acs/groups/content/@epidemiologysurveilance/documents/document/acspc-031941.pdf

[5] T. Ibtisam E., "Biosensors for cancer markers diagnosis," *Seminars in Cell & Developmental Biology*, vol. 20, no. 1, pp. 55–62, Feb. 2009. [Online]. Available: http://www.sciencedirect.com/science/article/pii/S1084952109000196

[6] S. Mousa, "Biosensors: the new wave in cancer diagnosis," *Nanotechnology, Science and Applications*, p. 1, Dec. 2010. [Online]. Available: http://www.dovepress.com/biosensors-the-new-wave-in-cancer-diagnosis-peer-reviewed-article-NSA

[7] H. B. Carter, L. Ferrucci, A. Kettermann, P. Landis, E. J. Wright, J. I. Epstein, B. J. Trock, and E. J. Metter, "Detection of Life-Threatening prostate cancer with Prostate-Specific antigen velocity during a window of curability," *Journal of the National Cancer Institute*, vol. 98, no. 21, pp. 1521 –1527, Nov. 2006. [Online]. Available: http://jnci.oxfordjournals.org/content/98/21/1521.abstract

[8] B. Martin, J. Finlay, K. Sterling, M. Ward, D. Lifsey, D. Mercante, J. Jainto, L. Martin, and W. Rayford, "Early detection of prostate cancer in african-american men through use of multiple biomarkers: human kallikrein 2 (hk2), prostate-specific antigen (psa), and free psa (fpsa)," *Prostate Cancer and Prostatic Diseases*, vol. 7, no. 2, pp. 132–137, 2004.

[9] A. J. Vickers, A. M. Cronin, M. J. Roobol, C. J. Savage, M. Peltola, K. Pettersson, P. T. Scardino, F. H. Schrder, and H. Lilja, "A four-kallikrein panel predicts prostate cancer in men with recent screening: Data from the european randomized study of screening for prostate cancer, rotterdam," *Clinical Cancer Research*, vol. 16, no. 12, pp. 3232–3239, Jun. 2010. [Online]. Available: http://clincancerres.aacrjournals.org/content/16/12/3232.abstract

[10] J. R. Grandis, M. F. Melhem, W. E. Gooding, R. Day, V. A. Holst, M. M. Wagener, S. D. Drenning, and D. J. Tweardy, "Levels of tgf- and egfr protein

in head and neck squamous cell carcinoma and patient survival," *Journal of the National Cancer Institute*, vol. 90, no. 11, pp. 824–832, Jun. 1998. [Online]. Available: http://jnci.oxfordjournals.org/content/90/11/824.short

[11] G. Sauerbrey, "Use of quartz vibrator for weighing thin films on a microbalance," *Z. Phys.*, vol. 155, pp. 206–210, 1959.

[12] C. J. Robinson and M. A. Baker, "A simple and inexpensive method of measuring thin film thicknesses," *Journal of Physics E: Scientific Instruments*, vol. 11, no. 7, pp. 625–627, Jul. 1978. [Online]. Available: http://iopscience.iop.org/0022-3735/11/7/008

[13] J. Hlavay and G. G. Guilbault, "Applications of the piezoelectric crystal detector in analytical chemistry," *Anal. Chem.*, vol. 49, no. 13, pp. 1890–1898, 1977. [Online]. Available: http://dx.doi.org/10.1021/ac50021a007

[14] Thompson, C. L. Arthur, and G. K. Dhaliwal, "Liquid-phase piezoelectric and acoustic transmission studies of interfacial immunochemistry." *Analytical Chemistry*, vol. 58, no. 6, pp. 1206–1209, 1986.

[15] S. H. Lee, "Theoretical and experiment characterization of time-dependent signatures of wave based biosensors," Ph.D. dissertation, Georgia Institute of Technology, 2006.

[16] T. W. Grudkowski, J. F. Black, T. M. Reeder, D. E. Cullen, and R. A. Wagner, "Fundamental-mode VHF/UHF minature acoustic resonators and filters on silicon," *Applied Physics Letters*, vol. 37, pp. 993–995, 1980, 11.

[17] K. Nakamura, H. Sasaki, and H. Shimizu, "ZnO/SiO2-diaphragm composite resonator on a silicon wafer," *Electronics Letters*, vol. 17, p. 507, 1981.

[18] R. Gabl, H. Feucht, H. Zeininger, G. Eckstein, M. Schreiter, R. Primig, D. Pitzer, and W. Wersing, "First results on label-free detection of DNA and protein molecules using a novel integrated sensor technology based on gravimetric detection principles," *Biosensors and Bioelectronics*, vol. 19, no. 6, pp. 615–620, Jan. 2004. [Online]. Available: http://www.sciencedirect.com/science/article/pii/S0956566303002598

[19] J. Weber, W. M. Albers, J. Tuppurainen, M. Link, R. Gabl, W. Wersing, and M. Schreiter, "Shear mode FBARs as highly sensitive liquid biosensors," *Sensors and Actuators A: Physical*, vol. 128, no. 1, pp. 84–88, Mar. 2006. [Online]. Available: http://www.sciencedirect.com/science/article/pii/S0924424706000264

[20] S. Pinkett, "Techniques to facilitate the fabrication of zno-based thin film bulk acoustic wave devices," Ph.D. dissertation, Georgia Institute of Technology, 2003.

[21] C. Corso, "Theoretical and experimental development of a zno-based laterally excited thickness shear mode acoustic wave immunosensor for cancer biomarker detection." Ph.D. dissertation, Georgia Institute of Technology, 2008.

[22] J. Rosenbaum, *Bulk Acoustic Wave Theory and Devices*, first edition ed. Artech Print on Demand, Jun. 1988.

[23] W. Hunt, D. Stubbs, and S. Lee, "Time-dependent signatures of acoustic wave biosensors," *Proceeding of the IEEE*, vol. 91, no. 6, pp. 890–901, 2003.

[24] J. S. Wang and K. M. Lakin, "c-axis inclined ZnO piezoelectric shear wave films," *Applied Physics Letters*, vol. 42, no. 4, p. 352, 1983.

[25] Link, M. Schreiter, J. Weber, R. Gabl, D. Pitzer, R. Primig, W. Wersing, M. B. Assouar, and O. Elmazria, "c-axis inclined ZnO films for shear-wave transducers deposited by reactive sputtering using an additional blind," *Journal of Vacuum Science and Technology A Vacuum Surfaces and Films*, vol. 24, no. 2, p. 218, 2006.

[26] W. E. Newell, "Face-mounted piezoelectric resonators," *Proceedings of the IEEE*, vol. 53, no. 6, pp. 575– 581, Jun. 1965.

[27] C. D. Corso, A. Dickerber, and W. Hunt, "A thickness shear mode zinc oxide liquid sensor with off-axis excitation," *Proceedings of the IEEE Sensors 2007 Conference*, p. 218, 2007.

[28] A. D. Wathen, F. Munir, and W. D. Hunt, "Trapped hybrid modes in solidly-mounted resonators based on c-axis oriented hexagonal crystals," *Journal of Applied Physics*, vol. 108, pp. 114 503–1 – 114 503–8, 2010.

[29] F. Munir, A. D. Wathen, and W. D. Hunt, "A ghz range, single structure, multi-mode zno, solidly-mounted bulk acoustic resonator," *IEEE International Ultrasonics Symposium, 2010*, pp. 853–856, 2010.

[30] A. D. Wathen, F. Munir, and W. D. Hunt, "A solidly-mounted, multi-mode zno bulk acoustic wave resonator," Patent 61/382 680, 2010.

[31] ——, "A high-q hybrid acoustic mode in thin film zno solidly mounted resonators," *Applied Physics Letters*, vol. 95, no. 12, pp. 123 509–123 509–2, 2009.

[32] S. Wu, Z.-X. Lin, M.-S. Lee, and R. Ro, "Bulk acoustic wave analysis of crystalline plane oriented zno films," *Journal of Applied Physics*, vol. 102, pp. 084 908–1 – 084 908–7, 2007.

[33] C. D. Corso, A. Dickherber, and W. D. Hunt, "Lateral field excitation of thickness shear mode waves in a thin film zno solidly mounted resonator," *Journal of Applied Physics*, vol. 101, no. 5, pp. 054 514–054 511 – 054 514–054 517, 2007.

[34] L. Woo Wai, S. Yonghua, and K. Eun Sok, "Lateral-field-excitation acoustic resonators for monolithic oscillators and filters," *Frequency Control Symposium, 1996. 50th., Proceedings of the 1996 IEEE International.*, pp. 558–562, 1996.

[35] W. Pang, H. Yu, J. W. Kwon, H. Zhang, and E. S. Kim, "Self-aligned lateral field excitation film acoustic resonator with very large electromechanical coupling [fbar]," *Frequency Control Symposium and Exposition, 2004*, pp. 558–561, 2004.

[36] A. D. Wathen, F. Munir, and W. D. Hunt, "A high-q acoustic mode in thin film zno solidly-mounted resonators," Patent 61/381 233, 2010.

[37] R. Lucklum and F. Eichelbaum, "Interface circuits for QCM sensors," vol. 5, pp. 3–47, 2007.

[38] M. Yang and M. Thompson, "Multiple chemical information from the thickness shear mode acoustic wave sensor in the liquid phase," *Analytical Chemistry*, vol. 65, pp. 1158–1168, 1993.

[39] S. Haeberle and R. Zengerle, "Microfluidic platforms for lab-on-a-chip applications," *Lab on a Chip*, vol. 7, no. 9, p. 1094, 2007. [Online]. Available: http://pubs.rsc.org.www.library.gatech.edu:2048/en/Content/ArticleLanding/2007/LC/b706364b

[40] T. G. Henares, F. Mizutani, and H. Hisamoto, "Current development in microfluidic immunosensing chip," *Analytica Chimica Acta*, vol. 611, no. 1, pp. 17–30, Mar. 2008. [Online]. Available: http://www.sciencedirect.com/science/article/pii/S0003267008002420

[41] S. Choi, M. Goryll, L. Y. M. Sin, P. K. Wong, and J. Chae, "Microfluidic-based biosensors toward point-of-care detection of nucleic acids and proteins," *Microfluidics and Nanofluidics*, vol. 10, no. 2, pp. 231–247, 2010.

[42] S. Tuomikoski and S. Franssila, "Free-standing SU-8 microfluidic chips by adhesive bonding and release etching," *Sensors and Actuators A: Physical*, vol. 120, no. 2, pp. 408–415, May 2005. [Online]. Available: http://www.sciencedirect.com/science/article/pii/S0924424705000348

[43] G. Voskerician, M. S. Shive, R. S. Shawgo, H. Von Recum, J. M. Anderson, M. J. Cima, and R. Langer, "Biocompatibility and biofouling of MEMS drug delivery devices." *Biomaterials*, vol. 24, no. 11, pp. 1959–1967, 2003.

[44] Hong, A. S. Holmes, and M. E. Heaton, "SU8 resist plasma etching and its optimisation," *Microsystem Technologies*, vol. 10, no. 5, pp. 357–359, 2004.

[45] L. J. Guerin, M. Bossel, M. Demierre, S. Calmes, and P. Renaud, "Simple and low cost fabrication of embedded micro-channels by using a new thick-film photoplastic," *Proceedings of International Solid State Sensors and Actuators Conference Transducers 97*, vol. 2, pp. 1419–1422, 1997.

[46] R. J. Jackman, T. M. Floyd, R. Ghodssi, M. A. Schmidt, and K. F. Jensen, "Microfluidic systems with on-line UV detection fabricated in photodefinable epoxy," *Journal of Micromechanics and Microengineering*, vol. 11, no. 3, pp. 263–269, May 2001. [Online]. Available: http://iopscience.iop.org/0960-1317/11/3/316

[47] C. Pan, H. Yang, S. Shen, M. Chou, and H. Chou, "A low-temperature wafer bonding technique using patternable materials," *Journal of Micromechanics and Microengineering*, vol. 12, no. 5, pp. 611–615, Sep. 2002. [Online]. Available: http://iopscience.iop.org/0960-1317/12/5/315

[48] T. M. Verhaar, J. Wei, and P. M. Sarro, "Pattern transfer on a vertical cavity sidewall using SU8," *Journal of Micromechanics and Microengineering*, vol. 19, no. 7, p. 074018, Jul. 2009. [Online]. Available: http://iopscience.iop.org/0960-1317/19/7/074018

[49] F. Rusmini, Z. Zhong, and J. Feijen, "Protein immobilization strategies for protein biochips," *Biomacromolecules*, vol. 8, no. 6, pp. 1775–1789, 2007. [Online]. Available: http://dx.doi.org/10.1021/bm061197b

[50] M. Wilchek and T. Miron, "Oriented versus random protein immobilization," *Journal of Biochemical and Biophysical Methods*, vol. 55, no. 1, pp. 67–70, Jan. 2003. [Online]. Available: http://www.sciencedirect.com/science/article/pii/S0165022X02001781

[51] S. V. Rao, K. W. Anderson, and L. G. Bachas, "Oriented immobilization of proteins," *Microchimica Acta*, vol. 128, no. 3, pp. 127–143, 1998. [Online]. Available: http://www.springerlink.com.www.library.gatech.edu:2048/content/r74ll2337rmq2233/abstract/

[52] J. Turkov, "Oriented immobilization of biologically active proteins as a tool for revealing protein interactions and function," *Journal of Chromatography B: Biomedical Sciences and Applications*, vol. 722, no. 12, pp. 11–31, Feb. 1999. [Online]. Available: http://www.sciencedirect.com/science/article/pii/S0378434798004344

[53] C. D. Corso, A. Dickherber, and W. D. Hunt, "An investigation of antibody immobilization methods employing organosilanes on planar ZnO surfaces for biosensor applications," *Biosensors & Bioelectronics*, vol. 24, no. 4, pp. 811–817, Dec. 2008, PMID: 18755581. [Online]. Available: http://www.ncbi.nlm.nih.gov/pubmed/18755581

[54] Y. C. Liu, N. Rieben, L. Iversen, B. S. Srensen, J. Park, J. Nygrd, and K. L. Martinez, "Specific and reversible immobilization of histidine-tagged proteins on functionalized silicon nanowires," *Nanotechnology*, vol. 21, no. 24, p. 245105, Jun. 2010. [Online]. Available: http://iopscience.iop.org/0957-4484/21/24/245105

[55] J. Schmitt, H. Hess, and H. G. Stunnenberg, "Affinity purification of histidine-tagged proteins," *Molecular Biology Reports*, vol. 18, no. 3, pp. 223–230, Oct. 1993, PMID: 8114690. [Online]. Available: http://www.ncbi.nlm.nih.gov/pubmed/8114690

[56] A. Tinazli, J. Tang, R. Valiokas, S. Picuric, S. Lata, J. Piehler, B. Liedberg, and R. Tamp, "High-Affinity chelator thiols for switchable and oriented immobilization of Histidine-Tagged proteins: A generic platform for protein chip technologies," *Chemistry - A European Journal*, vol. 11, no. 18, pp. 5249–5259, Sep. 2005. [Online]. Available: http://onlinelibrary.wiley.com.prx.library.gatech.edu/doi/10.1002/chem.200500154/full

[57] J. K. Lee, Y. Kim, Y. S. Chi, W. S. Yun, and I. S. Choi, "Grafting nitrilotriacetic groups onto carboxylic Acid-Terminated Self-Assembled monolayers on gold surfaces for immobilization of Histidine-Tagged proteins," *The Journal of Physical Chemistry B*, vol. 108, no. 23, pp. 7665–7673, 2004.

[58] S. H. Kim, M. Jeyakumar, and J. A. Katzenellenbogen, "Dual-Mode Fluorophore-Doped nickel nitrilotriacetic Acid-Modified silica nanoparticles combine Histidine-Tagged protein purification with Site-Specific fluorophore labeling," *J. Am. Chem. Soc.*, vol. 129, no. 43, pp. 13 254–13 264, 2007. [Online]. Available: http://dx.doi.org/10.1021/ja074443f

[59] H.-j. PaikThese authors contributed equal, Y. KimPresent address: Department of M, R. N. Orth, C. K. Ober, G. W. Coates, and C. A. Batt, "End-functionalization of poly(3-hydroxybutyrate)via genetic engineering for solid surface modification," *Chemical Communications*, no. 15, p. 1956, 2005. [Online]. Available: http://pubs.rsc.org/en/Content/ArticleLanding/2005/CC/b415809a

[60] K. Adachi, R. Yasuda, H. Noji, H. Itoh, Y. Harada, M. Yoshida, and K. Kinosita, "Stepping rotation of F1-ATPase visualized through angle-resolved single-fluorophore imaging," *Proceedings of the National Academy of Sciences of the United States of America*, vol. 97, no. 13, pp. 7243–7247, Jun. 2000, PMID: 10840052 PMCID: PMC16530.

[61] R. Lucklum and P. Hauptmann, "The delta f-Delta r QCM technique: an approach to an advanced sensor signal interpretation," *Electrochimica Acta*, vol. 45, pp. 3907–3916, 2000, 22-23.

[62] C. Chagnard, P. Gilbert, A. N. Watkins, T. Beeler, and D. W. Paul, "An electronic oscillator with automatic gain control: EQCM applications," *Sensors and Actuators B-Chemical*, vol. 32, pp. 129–136, 1996, 2.

[63] R. Behrends and U. Kaatze, "A high frequency shear wave impedance spectrometer for low viscosity liquids," *Measurement Science & Technology*, vol. 12, pp. 519–524, 2001, 4.

[64] A. Arnau, T. Sogorb, and Y. Jimenez, "A continuous motional series resonant frequency monitoring circuit and a new method of determining Butterworth-Van dyke parameters of a quartz crystal microbalance in fluid media," *Review of Scientific Instruments*, vol. 71, pp. 2563–2571, 2000, 6.

[65] D. Rocha, V. Ferrari, and B. Jakoby, "Improved electronic readout circuit for resonant acoustic sensors," in *Sensors, 2004. Proceedings of IEEE*, 2004, pp. 32–35 vol.1.

[66] T. Nakamoto and T. Kobayashi, "Development of circuit for measuring both q variation and resonant frequency shift of quartz crystal microbalance," *Ultrasonics, Ferroelectrics and Frequency Control, IEEE Transactions on*, vol. 41, pp. 806–811, 1994, 6.

[67] M. Rodahl and B. Kasemo, "A simple setup to simultaneously measure the resonant frequency and the absolute dissipation factor of a quartz crystal microbalance," *Review of Scientific Instruments*, vol. 67, pp. 3238–3241, 1996, 9.

[68] A. R. Hillman, A. Jackson, and S. J. Martin, "The problem of uniqueness of fit for viscoelastic films on thickness-shear mode resonator surfaces," *Analytical Chemistry*, vol. 73, pp. 540–549, 2001, 3.

[69] J. Schroder, R. Borngraber, R. Lucklum, and P. Hauptmann, "Network analysis based interface electronics for quartz crystal microbalance," *Review of Scientific Instruments*, vol. 72, pp. 2750–2755, 2001, 6.

[70] R. Schnitzer, C. Reiter, K. C. Harms, E. Benes, and M. Groschl, "A General-Purpose online measurement system for resonant BAW sensors," *Sensors Journal, IEEE*, vol. 6, pp. 1314–1322, 2006, 5. [Online]. Available: 10.1109/JSEN.2006.877977

[71] F. Eggers and T. Funck, "Method for measurement of shear-wave impedance in the mhz region for liquid samples of approximately 1 ml," *Journal of Physics E-Scientific Instruments*, vol. 20, pp. 523–530, 1987, 5.

[72] D. D. Taylor, S. Atay, D. S. Metzinger, and C. Gercel-Taylor, "Characterization of humoral responses of ovarian cancer patients: Antibody subclasses and antigenic components," *Gynecologic Oncology*, vol. 116, pp. 213–221, 2010, 2.

[73] Y. T. Yang, C. Callegari, X. L. Feng, K. L. Ekinci, and M. L. Roukes, "Zeptogram-scale nanomechanical mass sensing," *Nano Letters*, vol. 6, pp. 583–586, 2006, 4.

[74] R. P. Wali, P. R. Wilkinson, S. P. Eaimkhong, J. Hernando-Garcia, J. L. Sanchez-Rojas, A. Ababneh, and J. K. Gimzewski, "Fourier transform mechanical spectroscopy of micro-fabricated electromechanical resonators: A novel, information-rich pulse method for sensor applications," *Sensors and Actuators B-Chemical*, vol. 147, pp. 508–516, 2010, 2.

[75] N. B. Carvalho, J. C. Pedro, and J. P. Martins, "A corrected microwave multisine waveform generator," *Microwave Theory and Techniques, IEEE Transactions on*, vol. 54, pp. 2659–2664, 2006, 6.

[76] B. Du and D. Johannsmann, "Operation of the quartz crystal microbalance in liquids: derivation of the elastic compliance of a film from the ratio of bandwidth shift and frequency shift," *Langmuir*, vol. 20, pp. 2809–12, 2004, 7.

[77] H. L. Bandey, S. J. Martin, R. W. Cernosek, and A. R. Hillman, "Modeling the responses of thickness-shear mode resonators under various loading conditions," *Analytical Chemistry*, vol. 71, pp. 2205–2214, 1999, 11.

[78] R. Lucklum, C. Behling, R. W. Cernosek, and S. J. Martin, "Determination of complex shear modulus with thickness shear mode resonators," *Journal of Physics D-Applied Physics*, vol. 30, pp. 346–356, 1997, 3.

[79] R. Etchenique and A. D. Weisz, "Simultaneous determination of the mechanical moduli and mass of thin layers using nonadditive quartz crystal acoustic impedance analysis," *Journal of Applied Physics*, vol. 86, pp. 1994–2000, 1999, 4.

[80] D. Johannsmann, "Derivation of the shear compliance of thin films on quartz resonators from comparison of the frequency shifts on different harmonics: A perturbation analysis," *Journal of Applied Physics*, vol. 89, pp. 6356–6364, 2001, 11.

[81] M. Rodahl, F. Hook, A. Krozer, P. Brzezinski, and B. Kasemo, "Quartz-crystal microbalance setup for frequency and q-factor measurement in gaseous and liquid environments," *Review of Scientific Instruments*, vol. 66, pp. 3924–3930, 1995, 7.

[82] M. V. Voinova, M. Rodahl, M. Jonson, and B. Kasemo, "Viscoelastic acoustic response of layered polymer films at fluid-solid interfaces: Continuum mechanics approach," *Physica Scripta*, vol. 59, pp. 391–396, 1999, 5.

[83] A. Janshoff, C. Steinem, and D. Johannsmann, "Studies of viscoelasticity with the QCM," in *Piezoelectric Sensors*, ser. Springer Series on Chemical Sensors and Biosensors. Springer Berlin Heidelberg, 2007, vol. 5, pp. 49–109. [Online]. Available: http://dx.doi.org/10.1007/978-3-540-36568-6_2

[84] Y. Zhang, B. Du, X. Chen, and H. Ma, "Convergence of dissipation and impedance analysis of quartz crystal microbalance studies," *Anal Chem*, vol. 81, pp. 642–8, 2009, 2.

[85] P. J. Edmonson, P. M. Smith, and C. K. Campbell, "Injection locking techniques for a 1-GHz digital receiver using acoustic-wave devices," *Ultrasonics, Ferroelectrics and Frequency Control, IEEE Transactions on*, vol. 39, pp. 631–637, 1992, 5.

[86] R. G. Lyons, *Understanding Digital Signal Processing*, 1st ed. Pearson Education, Nov. 1996.

[87] M. H. Hayes, *Statistical Digital Signal Processing and Modeling*, 1st ed. Wiley, Apr. 1996.

VITA

Farasat Munir was born on June 29, 1979 and grew up in the Lahore Pakistan. He received a B.S. in electrical engineering from University of Engineering and Technology in 2001 and a M.S. in electrical engineering from Georgia Tech in 2007. After working in the industry in the field of Image processing , Machine vision, Communication system design for 4 years, Farasat came to Georgia Tech and did his Masters in electrical engineering in 2007. Under the advisement of Dr. William D. Hunt he completed his Ph.D in electrical engineering in 2012 with focus on biosensor design for cancer diagnosis and prognosis. Following his graduation he plans to continue research in the disciplines of electrical engineering and biomedical engineering.